Kazimierz Peszyński
Editor

Developments in machinery design and control

Vol. 3

University Press
University of Technology
and Agriculture in Bydgoszcz

Kazimierz Peszyński
Editor

Developments in machinery design and control

Vol. 3

University Press
University of Technology and Agriculture in Bydgoszcz

ASSOCIATE REVIEWERS
Jerzy Iwaszko, Assoc. Prof.; Prof. Józef Kubik;
Tadeusz Niezgoda, Assoc. Prof.; Franciszek Siemieniako, Assoc. Prof.

Proof-reading: Bernadeta Gierszewska, MA
Typeset by: Dorota Ślachciak, MA
Cover design: Daniel Morzyński, MSc

ISBN 83-89334-85-2

University Press of University of Technology and Agriculture
Editor-in-chief
Lucyna Drozdowska, Assoc. Prof.
Ks. A. Kordeckiego 20, 85-225 Bydgoszcz, phone +48(52) 3749482, 3749426
e-mail: wydawucz@atr.bydgoszcz.pl http://www.atr.bydgoszcz.pl/ wyd

---

1st edition. 100 copies. Author's sheets 5.4. Printed sheets 6.5. 3rd class printing paper.
Submitted and printing completed in February 2004. Order No 2/2004
Printed in: Small Typography of University of Technology and Agriculture
in Bydgoszcz, Ks. A. Kordeckiego 20

On behalf of all the Authors, I hereby proudly introduce volume 3 of 'Developments in Machinery Design and Control'. The aforementioned research presents selected issues discussed at the annual scientific conference under the same name, arranged and prepared by the Department of Control and Machinery Design, University of Technology and Agriculture, Bydgoszcz, Poland. A constantly growing applications of digital tools is the unique feature of our seminars – it easily enables the direct associative link between the intelligence of a human scholar and the impressive speed of a digital machine, or quite similar cooperation of the designer and the computer. My general conclusions, as a participant and observer of our seminars, are included in the initial paper 'Instead of Preface Some Words on Modeling and Numerical Computations'.

At the same time I would like to thank cordially all my colleagues and fellow scientists I have had a privilege to work with at the University of Technology and Agriculture for the last 30 years.

Kazimierz Peszyński

CONTENTS

Kazimierz Peszyński

University of Technology and Agriculture
Department of Control and Machinery Design
Prof. S. Kaliskiego 7, 85-796 Bydgoszcz

INSTEAD OF PREFACE SOME WORDS ON MODELING AND NUMERICAL COMPUTATIONS

1. INTRODUCTION

The presented further set of monographs submitted by the authors participating in the successive seminars 'Developments in Machinery Design and Control' exemplifies the effect of contemporary computational technology on current scientific research. A conclusion is suggested that without the computer the monographs could not exist or, in same cases, they would be difficult to generate.

The computer as a device serves as:

- terminal unit in the network, both local and worldwide. Here it can play an essential role as a tool on dispersed research or designs stand [7], or as an auxiliary tool facilitating contacts between researchers. In the latter case it is the best-known telecommunications tool, used almost exclusively when editing this publication. One could also risk a statement that it must have served the authors for contacts when preparing individual papers as a tool for:
- complex calculations. In this case it is a very fast calculator for numerical solution of differential equations (Tesař, Tippets, Allen)[1], (Hošek, Peszyński, Trávníček) or tasks based on logical decisions [1, 3];
- experimental results data acquisition and processing (Peszyński, Trávníček)], [1, 9, 10];
- typesetting; here it has been used as a word processor, graphical processor etc. by all the authors.

This brief list is already a sufficient illustration of how precious the tool is. However one should ask about the limits of its application. A perfect answer to this question is offered by a paper (Tesař, Tippets, Allen), which stresses that the man plays the key role in the research process, which should be expressed in experimental research verifying the numerical calculated results. Unfortunately, frequently, there is observed no such limited confidence. The author himself has noted a case in which a bridge calculated with genetic algorithms with the use of computer – was short off a bridge span. Another example is an uncritical use of computer as a text translator, e.g. from Polish to English. In this field we are likely to wait donkey's years for an accurate computer-generated translation. There is still more to it in everyday life. The computer, just like the car, makes you lazy. Frequently the spell check makes us unaware of the

[1] In the analysis presented further in this introduction, papers marked with surnames in parenthesis are included in this volume. The analysis is also based on conference papers presented in the cycle of seminars 'Developments in Machinery Design and Control' as well as on the first and second volumes of the series edited by Janusz Sempruch and Janusz Sempruch, Kazimierz Peszynski respectively, marked as references with digits in square brackets.

mistakes we have just made. When there is no red underline (MS Word), we do not assume that a word has been misspelled, e.g. in Polish between words 'miedzy" and 'między' or in English 'heat' and 'head' there is an obvious semantic difference, however the spell check does not recognize it. Another example can be a wrong word choice by the computer; the word 'promień' in Polish has two meanings: 'ray' or 'radius'. However the computer does not always differentiate between the contexts and so selects the wrong one. It is totally unacceptable to blame the computer for mistakes; it is only a tool which follows the software developed by man.

2. NUMERICAL SOLUTION OF RESEARCH PROBLEMS

Let us, however, relate back to scientific research. The most interesting papers include those which cover numerical calculations. Numerical methods were developed many years ago, however their wide application has been possible only since the computer appeared. There are many numerical methods, three of which have been used in the preparation of this volume by authors of the individual papers: Finite Differences Method (FDM) (Gawda, Zachwieja), (Zachwieja), Finite Elements Method (FEM, e.g. solver ANSYS) [2, 6], or Finite Volumes Method (FVM – solver FLUENT) (Tesař, Tippets, Allen). All these methods have one common feature which is digitization, however, in case of FDM it relates directly to equations, and in case of FEM and FVM – to integral domain. It leads to the replacement of differential equations with difference equations (in case of FDM) or with variation equations (in case of FEM and FVM). Finally, in all the methods a system (or systems) of algebraic equations is obtained whose solutions provide the unknown value (values) of the function in the discrete set of points referred to as nodes.

Numerical methods applied in scientific research for the last twenty years or so have been booming but surely there is still room for further research. In more complex processes nonlinear partial differential equations are researched (in fluid mechanics). This type of equations is not provided with a strict method of researching stability of solutions (iteration process). Nor there exist strict evaluations of error and evidence of convergence. Some progress has been made in proving existence and unambiguity of solutions, however, it is usually insufficient to provide an unambiguous answer to specific questions interesting for the designer.

In that situation FDM applications are, first of all, limited to linear cases and so simplified and remaining in a non-specified-in-detail relation to the reality. Sometimes one has to resort to heuristic assumptions, based on physical intuition and to replace strict evidence by trial and error or with numerical experiment. This experiment can replace neither physical experiment nor theoretical analysis due to inaccuracy of real material properties description with idealized equations (e.g. state equations), postulating unchangeability of some parameters which are, in fact, changeable. Finally the discretization process changes not only the accuracy of results but also sometimes qualitative character of solutions (Hošek, Trávníček, Peszyński).

Another limitation of the numerical experiment is an impossibility to consider some physical phenomena in the right way, mainly those whose spatial scale is too small to reconstruct them precisely on the differential grid (e.g. turbulence). The grid density is limited by computer memory and computer time-effectiveness. On the other hand, these phenomena important in micro scale can have an essential effect on

a further development of phenomena considered in macro scale (Tesař), which calls for introducing additional description parameters.

One has to remember about limitations of numerical experiment which come from the fact that it refers to specific parameters values. However the achievements of numerical methods so far provide non-experimental research results especially applicable when designing some devices and also justify the necessity of their further development based on new solvers. Yet the results of the numerical experiment should be, as indicated above, continuously confronted with experimental results.

3. NUMERICAL CALCULATIONS AND MODELING

In technique the term 'modeling' has different meanings, depending on the approach to the problem. As suggested by the heading of this section, experimental modeling (namely conducting experiments with product model) will not be covered although experimental research must be considered to be an important element of model verification. Modeling is understood as a procedure which, when applied to solving a given task, leads to final analytic or numerical solution.

Solving scientific problems, a model is always used, which means that the course and properties of a given phenomenon are not researched as a whole, but problems related to the course and characteristic properties of the model of this phenomenon in a given range of parameters and simplifying assumptions introduced while formulating the problem (model).

The widely applied term of *accurate solution* does not mean anything more than accurate analytical solution of a very simplified model which, due to those simplifications, can differ from the real state more than the solution of approximate model. The solution does not have to be anyhow related to the physical principle and models mathematically some of its characteristic properties. For the same reason usually numerical solution of the problem, derived from a more detailed mathematical model, is closer to the reality than the so-called accurate solution.

The introduction of computers has clearly changed the approach to mathematical modeling. Its limitations are not defined by analytic problem-solving skills, but by computer capacity and insufficient knowledge of the physical character of the phenomenon and possibilities of its description.

4. ELEMENTS OF MATHEMATICAL MODELING

Mathematical modeling involves a few stages:

4.1. Problem Formulating

Problem formulating, namely developing a convenient and most adequate physical model (description) of the phenomenon researched. This description should include:

- formulating initial and boundary conditions,
- geometrical, design, technological, and other limitations,
- approximation, which can be feasible, e.g. a selection of single-input single-output model, potential omission of 3D, omission of the effect of some phenomena, e.g. viscosity, turbulence etc.,
- considering general physical relations, e.g. thermodynamic relations defining gas (equation of state). Equation of state of perfect fluid is one of the greatest simplifications and limitations introduced to mathematical modeling,

- material relations which include all the relations defining transport fluid properties, e.g. viscosity, thermal conductivity. The same can be referred to solid: density, thermal conductivity,
- limiting the range of applications and references of all the above relations.

Limiting the range of references of the relations applied in the physical model is an *unconditioned* necessity since it also limits the range of results application possibilities. Sometimes the range of reference, or even the significance of approximations used can be already evaluated while developing the physical model. However, frequently it can be done only after completing calculation, or after comparing the results of calculations with experimental results.

While formulating the problem, it is necessary to realize that:

- differences between the results of calculations from the reality are most often due to an inadequate selection of the physical model,
- mathematical results can be always interpreted only within the selected physical model.

4.2. Developing Mathematical Model

Developing mathematical model of a given phenomenon involves a development of complete set of equations and formulating initial-boundary conditions. In most tasks the initial equations are made up of the system which results from *basic conservation* laws (e.g. equation of motion, continuity equation, and energy equation). It is recommended to start solving the problem always from that system of equations, even though, for some specific examples, this system could be simplified as early as over mathematical formulating of the task.

Usually the set of basic laws includes a greater number of unknowns than the number of equations, and so they must be supplemented with equations which characterrize material properties or motion character (e.g. turbulence model in fluid motion analysis). Although in many cases these supplementary equations can be obtained from generalized laws, almost in every case semi-empirical relations are applied.

The mathematical model is always developed from the point of view of its solving method (analytical, numerical). For that reason frequently different mathematical approximations are introduced. They involve such transformations of initial equations of the mathematical model which make practical solving of the model possible (e.g. linearization, asymptotic expansion etc.). The mathematical approximations cannot contradict the selected physical model, namely any mathematical transformations (simplifications) of initial equations must be adequate for the selected physical model.

4.3. Solution of the Boundary or/and Initial Task

Solution of the boundary or/and initial task (analytical, numerical) of a system of initial or transformed equations of the mathematical model. Modern computer solvers already comprise basic differential equations. The task of the user is to define boundary and initial conditions, which is essential as their inadequate selection can give totally wrong results (Hošek, Trávníček, Peszyński), (Tesař, Tippets, Allen).

4.4. Analysis and Interpretation of Mathematical Model Results

Analysis and interpretation of mathematical model results or their comparison with the reality (by experiment, experience etc.). At that stage it is also necessary to make the evaluation of the applicability of the mathematical model to describe the physical phenomenon. The term 'applicable description' refers to such description which gives

for a specific range of parameters such results which correspond most to the reality. However, this term poses at least two threats:

- the physical model can be applicable only locally (only in a limited range) and cannot be extended beyond a given area,
- the physical model can refer to the phenomenon which is difficult to research experimentally and so it is impossible to compare partial elements of the model with the experiment. The only comparison could be made by comprehensive characteristics which, however, does not show the effect of individual components of the model.

Each model is a specific reflection of the reality. It is developed based on knowledge acquired under specific conditions and its accuracy is connected with the description of the reality, and just like its general character, depends on how profound is our knowledge of the phenomenon observed. Although it is developed based on the requirements and objective criteria, in the general sense it cannot comprise anything else than what has been included into it. For that reason any extrapolation beyond the area of parameters it was derived for, must be very carefully verified by comparing it with the reality and theoretically justified. The applicability of the model beyond this area is a coincidence rather than signifies perfection of the model.

5. MATHEMATICAL MODELING AND EXPERIMENTS

Mathematical modeling, as mentioned above, cannot do without experiments which appear in the mathematical modeling process at two stages:

- at the initial stage, over physical model development,
- at the final stage over the verification of results and their confrontation with the reality.

The role of experimental research while mathematical modeling is different than while experimental modeling. The character of the experiment at the initial stage is mostly qualitative. For that reason different visualization processes can be essential here [4, 8]. The main function of experimental research at that stage is getting an image about the structure of the phenomenon observed, its physical mechanism, and mutual relations among characteristic variables as indispensable initial material for physically adequate formulation of the mathematical model, namely boundary condition describing most completely and most credibly the problem researched. The application of the capacity of the state-of-the-art computers clearly increases the requirements for preliminary experiments due to possibly most complete qualitative (phenomenological) experiments.

The verification experiments assumed at the final stage are to provide answers to the following questions:

- How do the results of the total mathematical modeling (which covers physical model, mathematical model, and all the simplifying transformations) comply quantitatively with the reality?
- How does the model selected (in what range of parameters and what accuracy) reflect and describe the physical structure of the phenomenon? (Tesař, Tippets, Allen). (Hošek, Trávníček, Peszyński).

Different requirements to be met by the experiment at both stages must be considered when selecting both the experimental method and the methodology of the measurement.

6. DATA ACQUISITION AND PROCESSING

Currently most experimental research is based on the application of personal computer both at data acquisition and processing. To obtain adequate results from DAQ system, each of the following elements is important:

- personal computer,
- sensors,
- signal conditioning,
- DAQ hardware,
- software.

The research presented included only the electrical measurements and so sensors refer to elements converting physical quantities into electrical signals, e.g. thermocouples, resistance thermometers, thermistors which converted temperature into voltage or electrical resistance. In other cases there occurred strain gauges, flow rate sensors, pressure sensors converting the physical quantities measured also into electrical signals. All the electrical signals show a great variation and so their applicability depends on signal conditioning interfaces with DAQ Hardware.

Signal conditioning accessories amplify low-level signals, isolate, filter, excite, and complete bridge configurations to appropriate signals for the measurement device. A thermocouple, for example, combines dissimilar metals to generate voltages that vary with temperature. Its electrical characteristics are: parasitic thermocouples, low-voltage output, low sensitivity, nonlinear output for which signal conditioning needs: cold-junction compensations, high amplification, high resolution and linearization, respectively.

There are measurements of analog physical quantities but everybody works with digital data. To understand how analog-to-digital conversion works, it is important to understand the Nyquist theorem and how it affects sampling rate and analog bandwidth. It is also important to understand the terms including input range, code width or vertical sensitivity, analog-to-digital converter (ADC) resolution, and triggering options. According to the Nyquist theorem, the minimum sampling rate must be twice the rate of the highest frequency component in the signal sampled. The frequency at one-half the sampling frequency is referred to as the Nyquist frequency. Theoretically, it is possible to recover information about signals with frequencies at or below the Nyquist frequency. Frequencies above the Nyquist frequency alias to appear between DC and the Nyquist frequency. Sampling rate is the rate at which a signal is acquired and digitized by an ADC. For example, in the audio domain, signals converted to electrical signals by a microphone commonly have frequency components up to 20 kHz. According to the Nyquist theorem, you need a digitizer with a sampling rate grater than 40 $kS \cdot s^{-1}$ to properly acquire the signals. Analog bandwidth is the frequency range (in hertz) in which a signal can be accurately digitized. This limitation is determined by the frequency response on the input path. Input signals with frequencies above this bandwidth result in loss of amplitude and phase information. Analog bandwidth is defined by the frequencies at which the measured amplitude is 3 dB below the actual amplitude of the signal (Hošek, Trávníček, Peszyński), (Zachwieja). Measurement services software integrates measurement hardware into application development environment. The three main components of this software are configurations utilities, applications programming interfaces and driver engines. Different types of applications

and measurement hardware sometimes require different application programming interfaces (APIs).

7. CONCLUSIONS

The papers presented at the seminars 'Developments in Machinery Design and Control', despite a wide range of topics, show numerous applications of digital techniques. One can say that a modern researcher can 'see, hear, taste, and touch' problems with accuracy hundreds of times higher than any other researcher twenty years ago. He can store all of the information from his sensors with very little error, then immediately process and communicate all of this information to anywhere in the world. Therefore the present volume includes reports developed distant from one another which have been, however, a common effort made to investigate a problem of common interest.

As it is seen from the papers analyzed, electronics (measurement techniques) and computer science have penetrated profoundly into mechanics. The synergy among these techniques is currently referred to as mechatronics [5]. And maybe it is simply modern mechanics?

REFERENCES

[1] Cichański A., Maciejewski J., 2003. Numerical Analysis of Chosen Parameters of an Industrial Robot PL-7. [In:] Sempruch J., Peszyński K. (eds.) Developments in Machinery Design and Control. Wyd. Uczeln. ATR w Bydgoszczy, Vol. 2, 15-24.
[2] Lipski A., 2002. Modelling by Using FEM Exemplified by a Complex Structural Unit. Proceedings of annular seminary: Developments in Machinery Design and Control, Bydgoszcz – Duszniki.
[3] Macko M., 2002. Computer-Aided Multiple-Disc-Shredding Research. [In:] Sempruch J. (ed.), Development in Control and Machinery Design. Wyd. Uczeln. ATR w Bydgoszczy, 41-46.
[4] Peszyński K., Trávniček Z., 2002. Jet Flow Visualisation for an Axisymmetric Nozzle. [In:] Sempruch J. (ed.), Development in Control and Machinery Design. Wyd. Uczeln. ATR w Bydgoszczy, 55-64.
[5] Sempruch J., Peszyński K., 2003. Selected Designing Ideas; Stages, Significance and its Role. [In:] Sempruch J., Peszyński K. (eds.) Developments in Machinery Design and Control, Wyd. Uczeln. ATR w Bydgoszczy, Vol. 2, 7-14.
[6] Skibicki D., 2002. AFEM in Calculation of the Stress and Deformation of Welding Constructions. [In:] Sempruch J. (ed.), Development in Control and Machinery Design. Wyd. Uczeln. ATR w Bydgoszczy, 87-94.
[7] Skibicki D., Farbotko M., 2003. Internet-Based Technical Projects Management System Allowing for Team-Work in Dispersed Environment. [In:] Sempruch J., Peszyński K. (eds.) Developments in Machinery Design and Control, Wyd. Uczeln. ATR w Bydgoszczy, Vol. 2, 63-72.
[8] Wawrzyniak S., 2002. Station for Continuous Visualization of Flow in Fluidic Elements. Proceedings of annular seminary: Developments in Machinery Design and Control, Bydgoszcz – Duszniki.
[9] Wawrzyniak W., 2002. CT Anemometric Velocity Profile Investigation Behind the Axisymmetric Nozzle. [In:] Sempruch J. (ed.), Development in Control and Machinery Design. Wyd. Uczeln. ATR w Bydgoszczy, 95-100.

[10] Wawrzyniak S., Peszyński K., 2003. Investigations of Turbulent Pulsation Changes and Mean Velocity Depending on Forcing Frequency in Annular Axisymmetric Nozzle. [In:] Sempruch J., Peszyński K. (eds.) Developments in Machinery Design and Control, Wyd. Uczeln. ATR w Bydgoszczy, Vol. 2, 91-96.

Adam Budzyński
University of Technology and Agriculture
Department of Machine Maintenance
Prof. S. Kaliskiego 7, 85-796 Bydgoszcz
Jerzy Małachowski
Military University of Technology
Department of General Mechanics
Prof. S. Kaliskiego 2, 00-098 Warsaw

NUMERICAL MOVEMENT ANALYSIS OF THE AIRCRAFT UNDERCARRIAGE FRONT GEAR 3D MODEL

Summary: The paper contains the effect of the numerical movement analysis of the 3D assembly model of the aircraft undercarriage front gear. The CAD model is created in the Solid Edge V11 environment. The analysis is examined in the visual Nastran 4D system. The mechanism movement is the effect of linear actuation of the part called the shock absorber's piston rod. During the movement simulation, chosen parts are tracked and values of their motion parameters, namely, location, dislocation, velocity and acceleration (linear or angular) are recorded.

Keywords: numerical motion analysis, CAD, aircraft undercarriage, simulation

1. INTRODUCTION

A majority of mechanisms contain elements that move on relatively long distances or/and with relatively high speeds (linear or angular). For that reason, modern engineers should add to their previous tasks (describing a project with values of geometric, dynamic and material parameters) a brand new one: simulating the behaviour of the machine that is currently designed. For the sake of simplicity of adjusting the project, if any mistakes are noticed, the designers are able to make the mechanism motion optimal already during the designing process.

Numerical movement analysis (referred to as *the simulation*) should be examined already at the early stage of the product lifecycle, which is the design process. It means the machine whose motion is to be simulated, has not been manufactured yet. The only way to carry such an examination is to test the digital model imported from the CAD system.

In the 1990s, about 95% of motion simulations was carried with the real (already manufactured) mechanisms [3]. The results of such an analysis are subjective as:

- many elements of the real mechanisms are manufactured imperfect, according to the design documents,
- it is not possible to measure the movement of real mechanisms with a desired high precision at low costs.

Furthermore, if the motion analysis enables engineers to detect serious motion errors:

- it takes much time to improve the designs,
- it is very dangerous (for the staff) to deal with such mechanisms, if they have already been available on the market.

In case of the numerical motion analysis, none of these disadvantages can be found. Numerical simulations are helpful in detecting all dangerous mechanisms conditions, which increases the safety and reliability of the maintenance process.

The role of the aircraft undercarriage front gear (except for being a fulcrum) is to enable the pilot to manoeuvre the aircraft on the airfield, by turning the front wheel (or wheels) on the surface. As for this object, the motion analysis created during the designing process is particularly important because object maintenance conditions [2] are supposed to be difficult. The aircraft carrying the front gear is prepared to operate on camp airfields or damaged ones, it belongs to the STOL [5, 6, 7] group ('Short Take-Off and Landing'), in Russian AKBP [4] ("Аєродина Короткого Взлета и Посадки").

2. OBJECT OF INVESTIGATION

The object of investigation is the 3D digital model of the aircraft undercarriage front gear (referred to as *the model*). It is the complex assembly built with 317 parts.

Fig. 1. Analysis of the aircraft undercarriage front gear system (assembly) with 14 subsystems (subassemblies)

The 3D model is understood as the system (assembly) and it is divided into 14 subsystems (subassemblies), according to their functions (Fig. 1). The scheme of the model with the location of chosen subsystems can be found in Fig. 2 (chosen parts are rendered as clear ones to make hidden elements visible).

3. DEFINITIONS OF CHOSEN MODEL CONFIGURATIONS

In the paper, model configuration means the set of information connected with values of location, dislocation, velocity and acceleration of important object parts in the chosen moment in time. To make the numerical motion analysis possible, general statements have been assumed before it was examined:

a. The axis of the shock absorber model is vertical, the model of a front wheel can move (by turning around its axis) only on a horizontal plane.
b. The main part of the model is the shock absorber piston rod. Its only degree of freedom is the ability of the linear movement along its symmetry axis between two extreme positions.
c. Piston rod Lower Extreme Position (*L.E.P.*) means such a piston rod location where it cannot move further outside of the cylinder anymore.
d. Piston rod Upper Extreme Position (*U.E.P.*) means such a piston rod location where it cannot move further to the bottom of the cylinder anymore.
e. Every position of the piston rod between *L.E.P.* and *U.E.P.* is called halfway.
f. Configurations of the model, when the piston rod can be found in *L.E.P.* or *U.E.P.* are called the main ones, respectively, Lower Main Configuration (*L.M.C*) and Upper Main Configuration (*U.M.C.*).
g. During the motion simulation only the most complex and the largest parts are tracked and include: the piston rod, rocking lever (one of the two symmetrically positioned ones), shock absorber connector and the front wheel (Fig. 3).

There is the iso view and the cross-section of the model found in the *L.M.C.*, see Fig. 4. The piston rod, moving outside the cylinder sleeve, hits with its upper bumper face (*UB*) the cylinder lower bumper one (*LB*), Fig. 5. The measurements are:

- linear distance between *LB* and *UB* is $L_{LB,UB} = 0$ mm,
- linear distance between the face of the piston rod head (*PH*) and, the face of the stifle division (*SD*) is $L_{PH,SD} = 99.6$ mm,
- α angle between a chosen vertical plane and the face of the shock absorber connector is $\alpha = 4.814°$,
- β angle between a chosen horizontal plane and the symmetry plane of the rocking lever is $\beta = 58.453°$.

Fig. 6 shows the isometric view and the cross-section of the model found in the *U.M.C.*. Such a configuration takes place when the piston rod, moving to the bottom of the cylinder, hits with the face of its head (*PH*) the face of the stifle division (*SD*), see Fig. 7. The measurements are:

- linear distance between *LB* and *UB* is: $L_{LB,UB} = 99.6$ mm,
- linear distance between the face of the piston rod head (*PH*) and the face of the stifle division (*SD*) is $L_{PH,SD} = 0$ mm,
- α angle between a chosen vertical plane and the face of the shock absorber connector is $\alpha = -17.957°$,
- β angle between a chosen horizontal plane and the symmetry plane of the rocking lever is $\beta = 6.293°$.

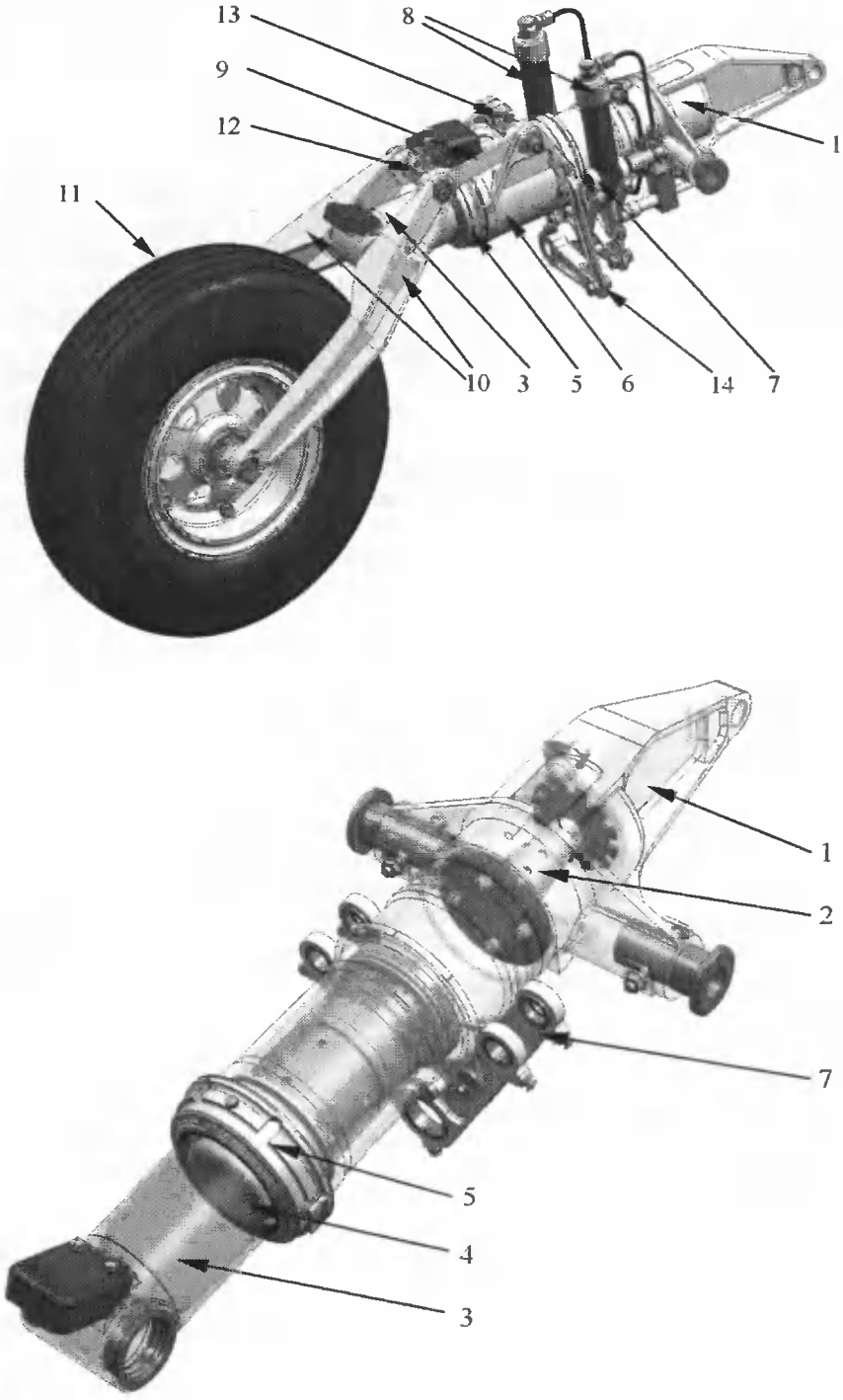

Fig. 2. Model where locations of chosen subsystems are indicated

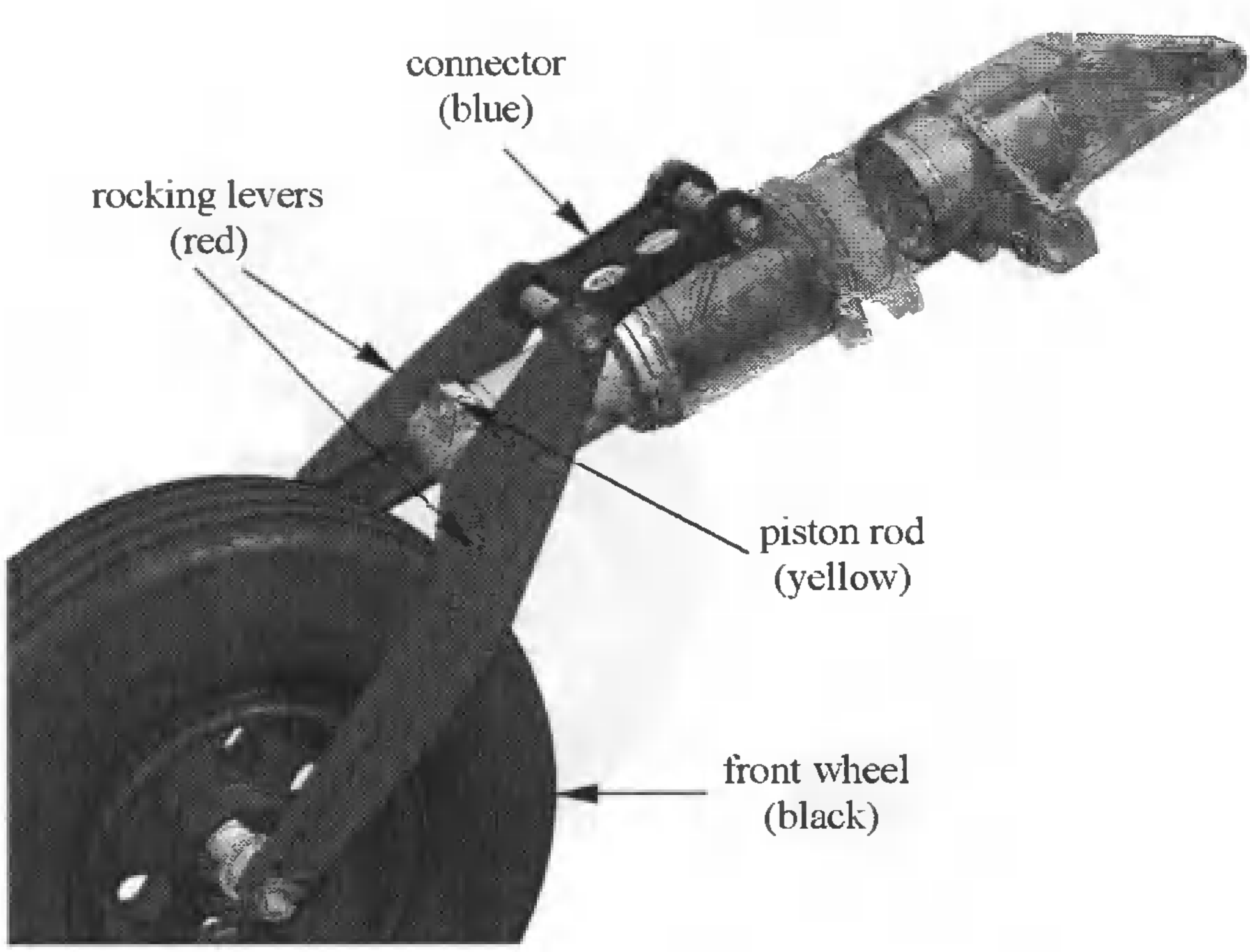

Fig. 3. Parts tracked during the movement simulation

4. NUMERICAL MOVEMENT SIMULATION OF THE AIRCRAFT UNDERCARRIAGE FRONT WHEEL

In the paper, to examine the numerical movement simulation means to find mathematical relationships between values of motor locations and locations of tracked parts. It is also possible to find out temporary values of velocity and acceleration (both linear or/and angular) of every single tracked part.

The 3D model of the aircraft undercarriage front wheel is an example of a simple motion chain. The general assumption is, that only one of assembly parts (the piston rod) can be active, i.e. to drive the model. The piston rod, i.e. the part that drives the assembly here referred to as *the motor*. It is also assumed that the piston rod is supposed to move from *L.M.C.* to *U.M.C.* (linear distance) with the constant velocity 99.6 [mm/s] to reach the destination (*U.M.C.*) in 1s. That means the piston rod is the model linear actuator.

While the simulation is on, the parts tracked are: the piston rod, rocking lever, connector and the front wheel. After the model is imported from the CAD Solid Edge V11 system [1] to the visual Nastran 4D environment, all constraints are defined automatically, according to relationships imposed on parts in the CAD system while assembly building. In the visual Nastran 4D environment, with the Constraint Navigator tool, every single constraint can be checked out, edited or removed if necessary. There is a chosen step of editing the revolute joint within the constraint of the connector and rocking levers shown in Fig. 8.

The preliminary simulation of the model is necessary to be examined to verify defined values of motor movement parameters. Then values of dislocation, velocity and acceleration of the piston rod (the driving part) are recorded, Fig. 9.

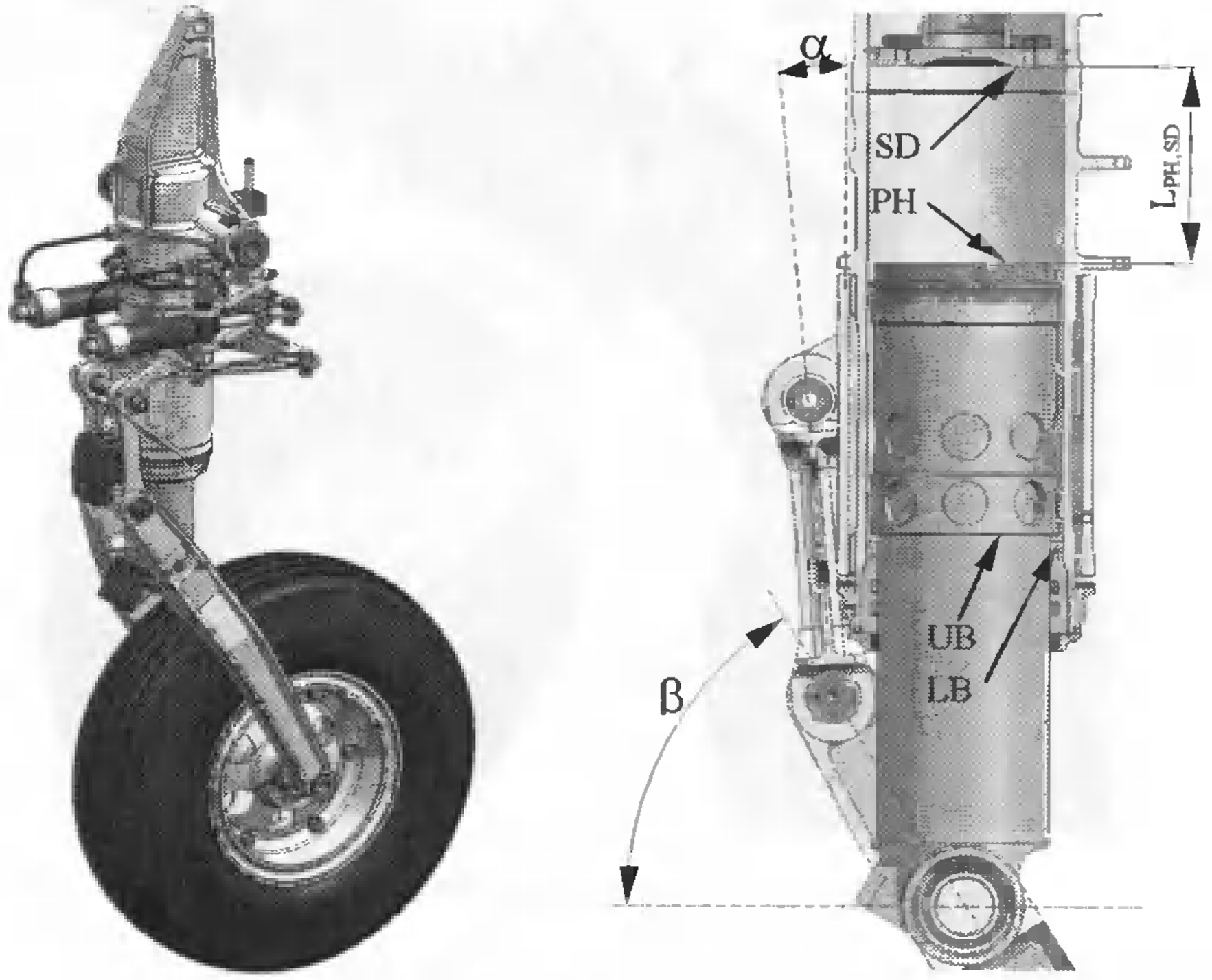

Fig. 4. Isometric view and the cross-section of the model found in the *L.M.C.*

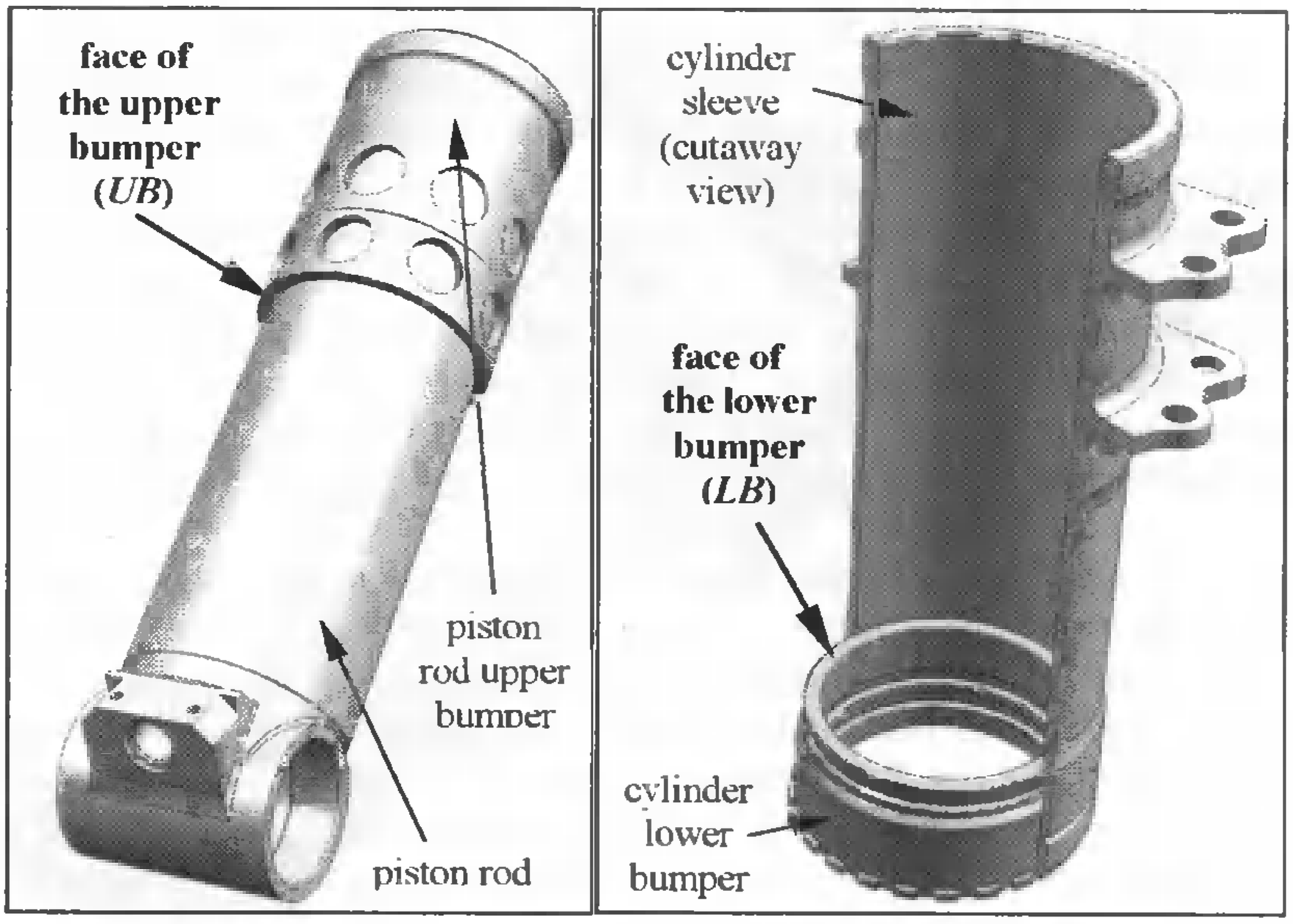

Fig. 5. Model will be found in the *L.M.C.* if the parts faces marked, shown above, contact each other

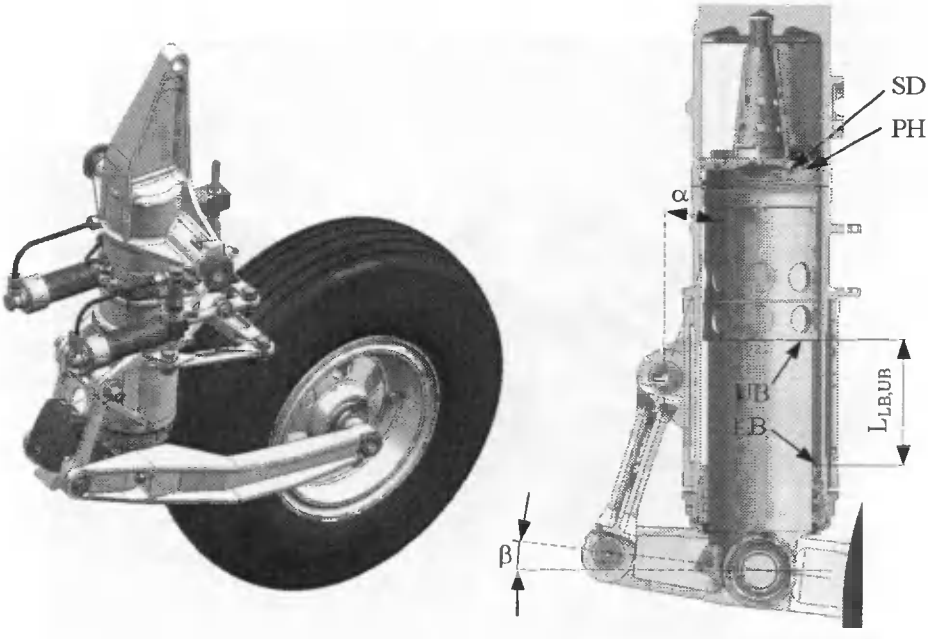

Fig. 6. Isometric view and the cross-section of the model in the *U.M.C.*

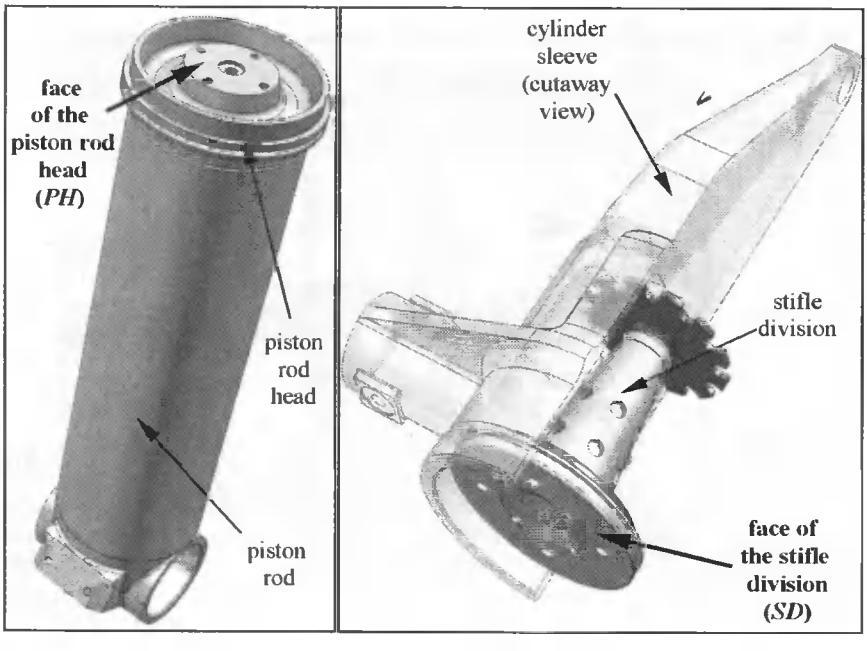

Fig. 7. Object of investigation will be found in the *U.M.C.* if the parts faces marked, shown above, contact each other

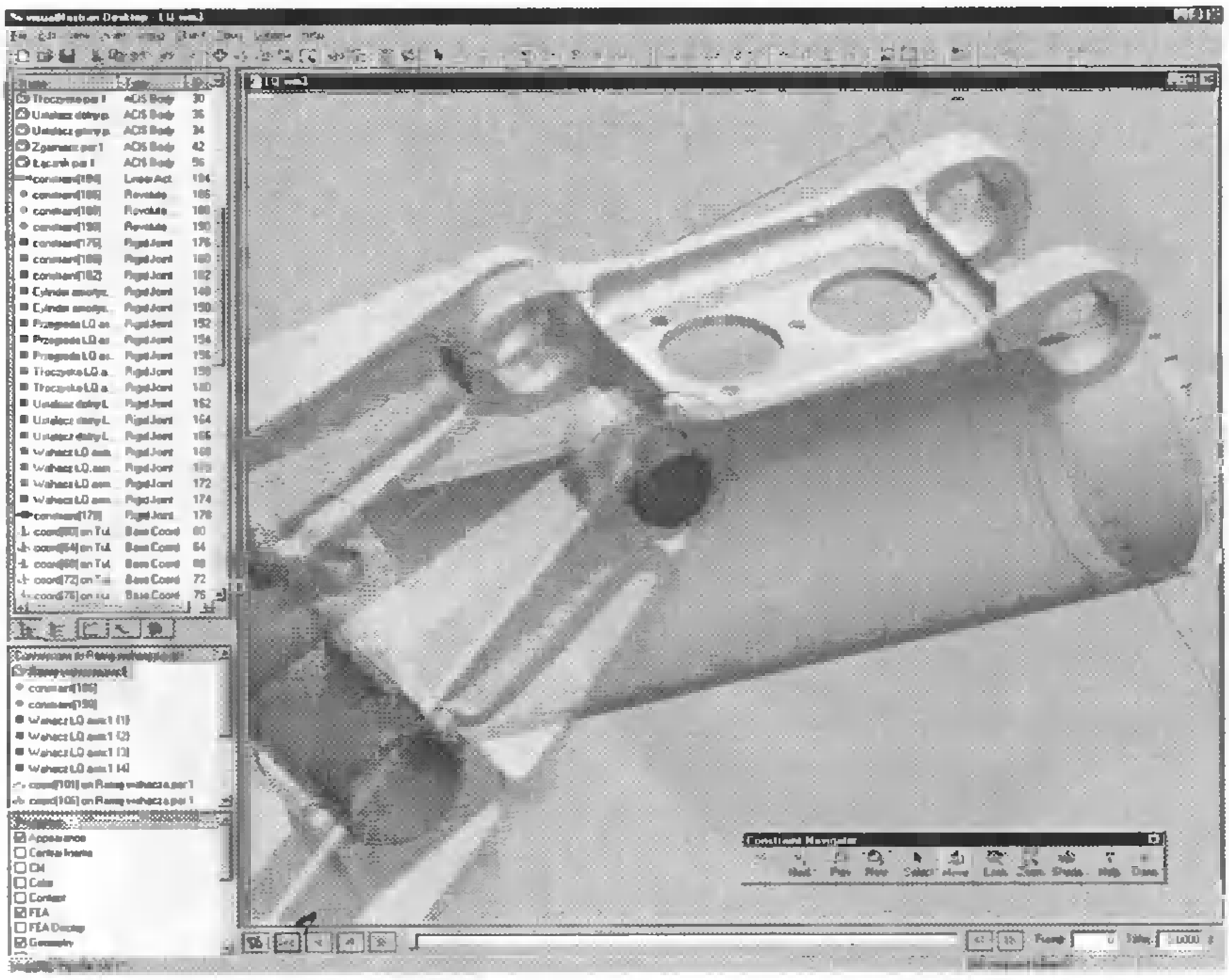

Fig. 8. All the constraint have to be specially defined to make the simulation run

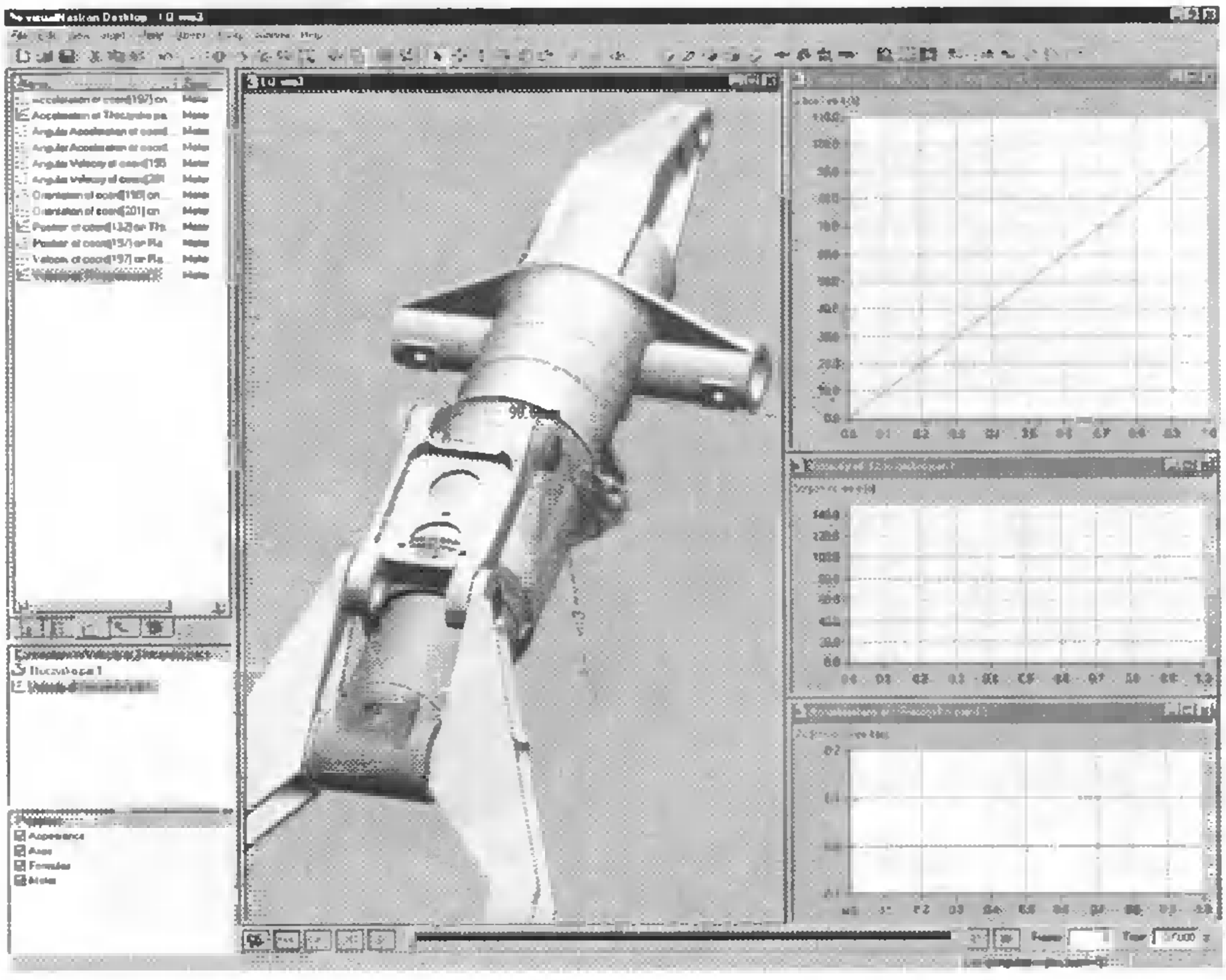

Fig. 9. Preliminary simulation. when only the motor behaviour is tracked and recorded. it is necessary to verify the correctness of motor movement parameters values defined

The full simulation supplies the user with information connected with the values of:

- angular: location, dislocation, velocity and acceleration (in relation to the vertical plane) of the rocking lever,
- angular: location, dislocation, velocity and acceleration (in relation to the horizontal plane) of the shock absorber connector,
- linear: dislocation, velocity and acceleration (in relation to the piston rod symmetry axis) of the front wheel.

For charts with the values of tracked parts movement parameters, see Fig. 10. The main effects of the motor motion from *L.E.P.* to *U.E.P.* are:

- angle of the connector rotation: $\Delta\alpha = 22.775°$,
- angle of the rocking lever rotation: $\Delta\beta = 52.160°$,
- linear vertical distance of the front wheel move: $L_{FW} = 355.791$ mm.

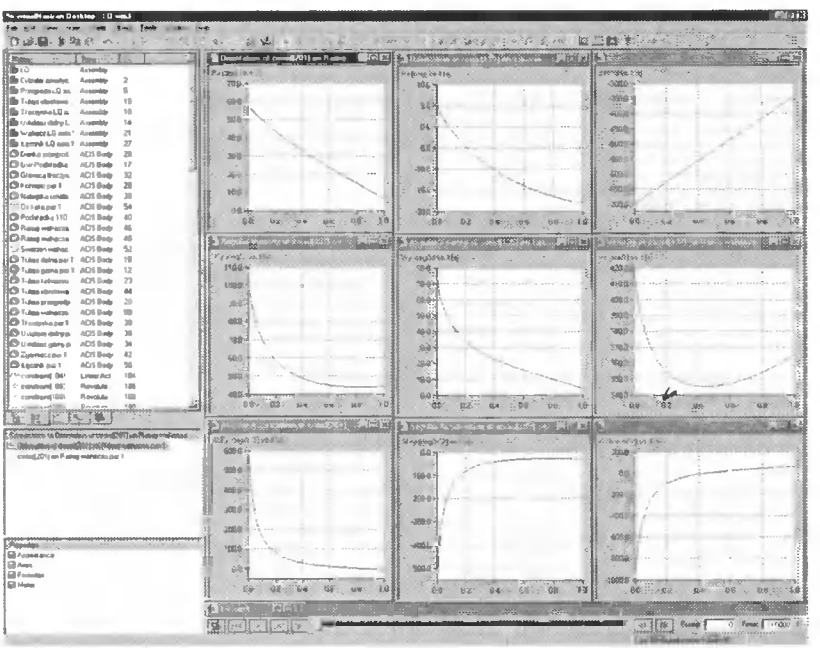

Fig. 10. Charts of the tracked elements movement parameters values

5. SIMULATION RESULTS

The process of the piston rod motion between its two (upper and lower) extreme positions is divided into 50 steps that last 0.02 s each. For every single one of them, desired values are recorded, see Fig. 10. The full simulation run effects are described with high order equations.

5.1. Piston Rod Movement

Analysing the piston rod movement (Fig. 11), motion functions were found:

– function of the axial dislocation:

$$S_t(t) = 99.6 \cdot t \ \text{[mm]} \tag{1}$$

– function of the linear velocity:

$$V_t(t) = \frac{dS_t(t)}{dt} = 99.6 \ [\text{mm}\cdot\text{s}^{-1}] \tag{2}$$

– function of the linear acceleration:

$$A_t(t) = \frac{dV_t(t)}{dt} = \frac{d^2S_t(t)}{dt^2} = 0 \ [\text{mm}\cdot\text{s}^{-2}] \tag{3}$$

t – time which has gone by since the process started – piston rod moved from the *L.E.P.*

5.2. Rocking Lever Movement

According to the charts received (Fig. 12), chosen motion functions were found:

– function of the angular location:

$$\alpha_w = 5\cdot10^{-9}t^6 - 10^{-6}t^5 + 8\cdot10^{-5}t^4 + \\ -3.1\cdot10^{-3}t^3 + 7.59\cdot10^{-2}t^2 - 2.05t + 60.4 \ \text{[deg]} \tag{4}$$

– function of the angular dislocation:

$$\beta_w = -5\cdot10^{-9}t^6 + 10^{-6}t^5 - 8\cdot10^{-5}t^4 + \\ +3.1\cdot10^{-3}t^3 + 7.59\cdot10^{-2}t^2 - 2.05t - 1.93 \ \text{[deg]} \tag{5}$$

– function of the angular velocity:

$$\omega_w(t) = \frac{d\alpha_w(t)}{dt} \ [\text{deg}\cdot\text{s}^{-1}]$$

$$\omega_w(t) = 3\cdot10^{-8}t^5 - 5\cdot10^{-6}t^4 + 3.2\cdot10^{-4}t^3 + \\ -9.3\cdot10^{-3}t^2 + 15.2\cdot10^{-2}t - 2.05 \ [\text{deg}\cdot\text{s}^{-1}] \tag{6}$$

– function of the angular acceleration:

$$\varepsilon_w(t) = \frac{d\omega_w(t)}{dt} = \frac{d^2\alpha_w(t)}{dt^2} \ [\text{deg}\cdot\text{s}^{-2}]$$

$$\varepsilon_w = 1.5\cdot10^{-7}t^4 - 2\cdot10^{-5}t^3 + 9.6\cdot10^{-4}t^2 - 1.86\cdot10^{-2}t + 0.152 \ [\text{deg}\cdot\text{s}^{-2}] \tag{7}$$

t – time which has gone by since the process started – piston rod moved from the *L.E.P.*

5.3. Shock Absorber Connector Movement

According to the charts found (Fig. 13), chosen motion functions were found:

– function of the angular location:

$$\alpha_1(t) = 5\cdot10^{-9}t^6 - 9\cdot10^{-7}t^5 + 6\cdot10^{-5}t^4 + \\ -2.6\cdot10^{-3}t^3 + 6.59\cdot10^{-2}t^2 - 1.47t + 6.18 \ \text{[deg]} \tag{8}$$

– the function of the angular dislocation:

$$\beta_1(t) = -5\cdot10^{-9}t^6 + 9\cdot10^{-7}t^5 - 6\cdot10^{-5}t^4 + \\ +2.6\cdot10^{-3}t^3 - 6.59\cdot10^{-2}t^2 + 1.47t - 1.37 \ \text{[deg]} \tag{9}$$

- function of the angular velocity:

$$\omega_1(t) = \frac{d\alpha_1(t)}{dt} \ [\text{deg}\cdot\text{s}^{-1}]$$

$$\omega_1(t) = 3\cdot10^{-8}t^5 - 4.5\cdot10^{-6}t^4 + 2.4\cdot10^{-4}t^3 + \\ -7.8\cdot10^{-3}t^2 + 1.32\cdot10^{-1}t - 1.47 \quad [\text{deg}\cdot\text{s}^{-1}] \tag{10}$$

- function of the angular acceleration:

$$\varepsilon_1(t) = \frac{d\omega_1(t)}{dt} = \frac{d^2\alpha_1(t)}{dt^2} \ [\text{deg}\cdot\text{s}^{-2}]$$

$$\varepsilon_1(t) = 1.5\cdot10^{-7}t^4 - 1.8\cdot10^{-5}t^3 + 7.2\cdot10^{-4}t^2 - 1.56\cdot10^{-2}t + 0.132 \ [\text{deg}\cdot\text{s}^{-2}] \tag{11}$$

t time which has gone by since the process started - piston rod moved from the *L.E.P.*

5.4. Front Wheel Movement

According to the charts found (Fig. 14), chosen motion functions were found:

- function of the linear (axial) location:

$$S_k(t) = -9\cdot10^{-9}t^6 + 2\cdot10^{-6}t^5 - 10^{-4}t^4 + \\ +5.2\cdot10^{-3}t^3 - 1.19\cdot10^{-1}t^2 + 8.4t - 8.2 \quad [\text{mm}] \tag{12}$$

- function of the linear (axial) velocity:

$$V_k(t) = \frac{dS_k(t)}{dt} \ [\text{mm}\cdot\text{s}^{-1}]$$

$$V_k(t) = -5.4\cdot10^{-8}t^5 + 10^{-5}t^4 - 4\cdot10^{-4}t^3 + \\ +1.56\cdot10^{-2}t^2 - 2.39\cdot10^{-1}t + 8.4 \quad [\text{mm}\cdot\text{s}^{-1}] \tag{13}$$

- function of the linear (axial) acceleration:

$$A_k(t) = \frac{dV_k(t)}{dt} = \frac{d^2S_k(t)}{dt^2} \ [\text{mm}\cdot\text{s}^{-2}]$$

$$A_k(t) = y = -2.7\cdot10^{-7}t^4 + 4.0\cdot10^{-5}t^3 + \\ -1.2\cdot10^{-3}t^2 + 3.12\cdot10^{-2}t - 2.29\cdot10^{-1} \quad [\text{mm}\cdot\text{s}^{-2}] \tag{14}$$

t – time which has gone by since the process started - piston rod moved from the *L.E.P.*

6. CONCLUSIONS

The numerical engineering environments, both Solid Edge V11 and visual Nastran 4D, are very helpful for the designer to create the 3D model of the aircraft undercarriage front gear and examine its motion analysis. Using them, the designer is able to predict the movement character of the complex assembly before it is manufactured.

For the sake of the simplicity of adjusting the project to the optimal form (if the motion errors are found or if the motion character does not fit the maintenance conditions) the numerical motion analysis is a very easy and efficient tool.

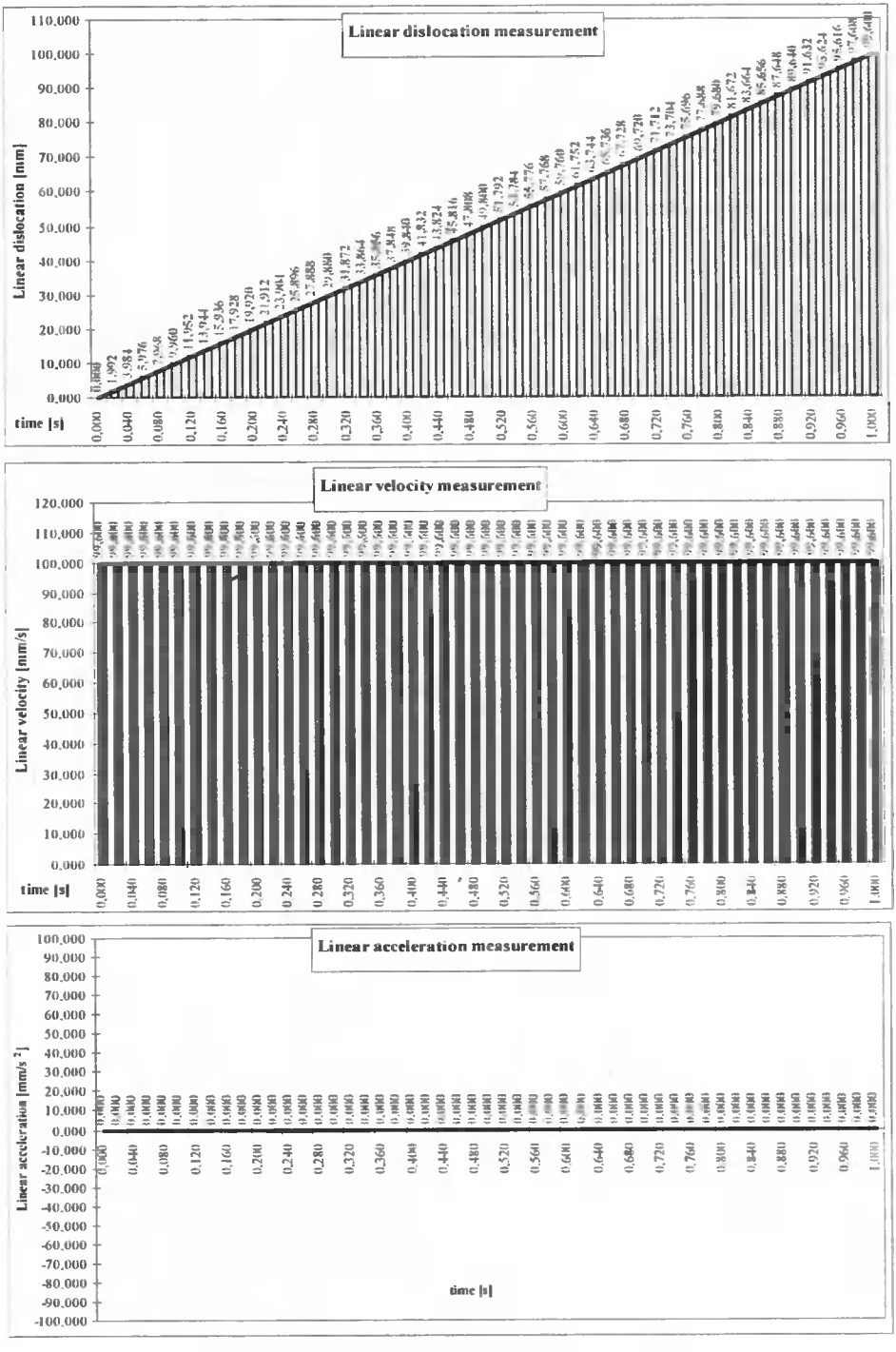

Fig. 11. Piston rod movement parameters values

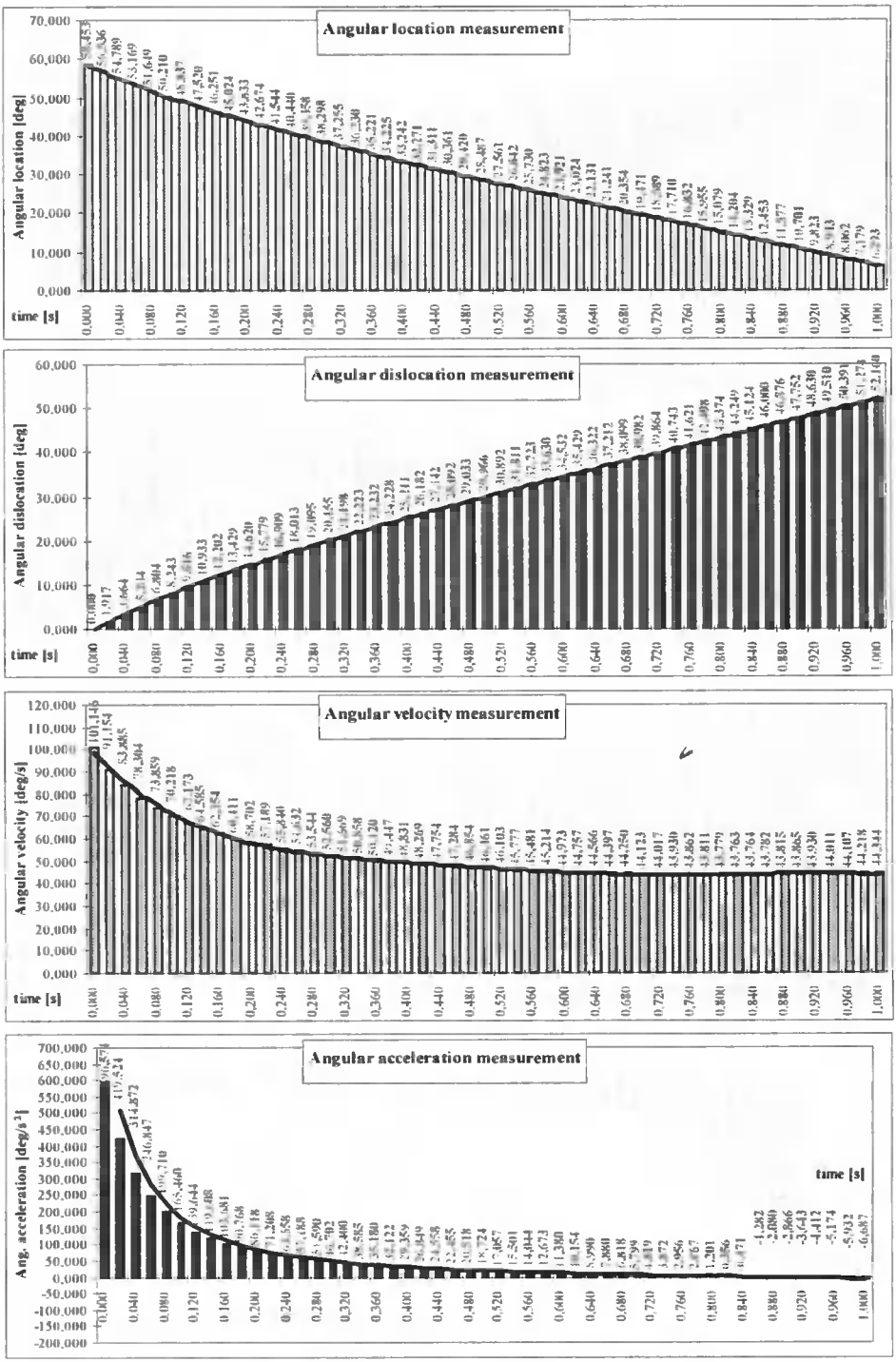

Fig. 12. Rocking lever movement parameters values

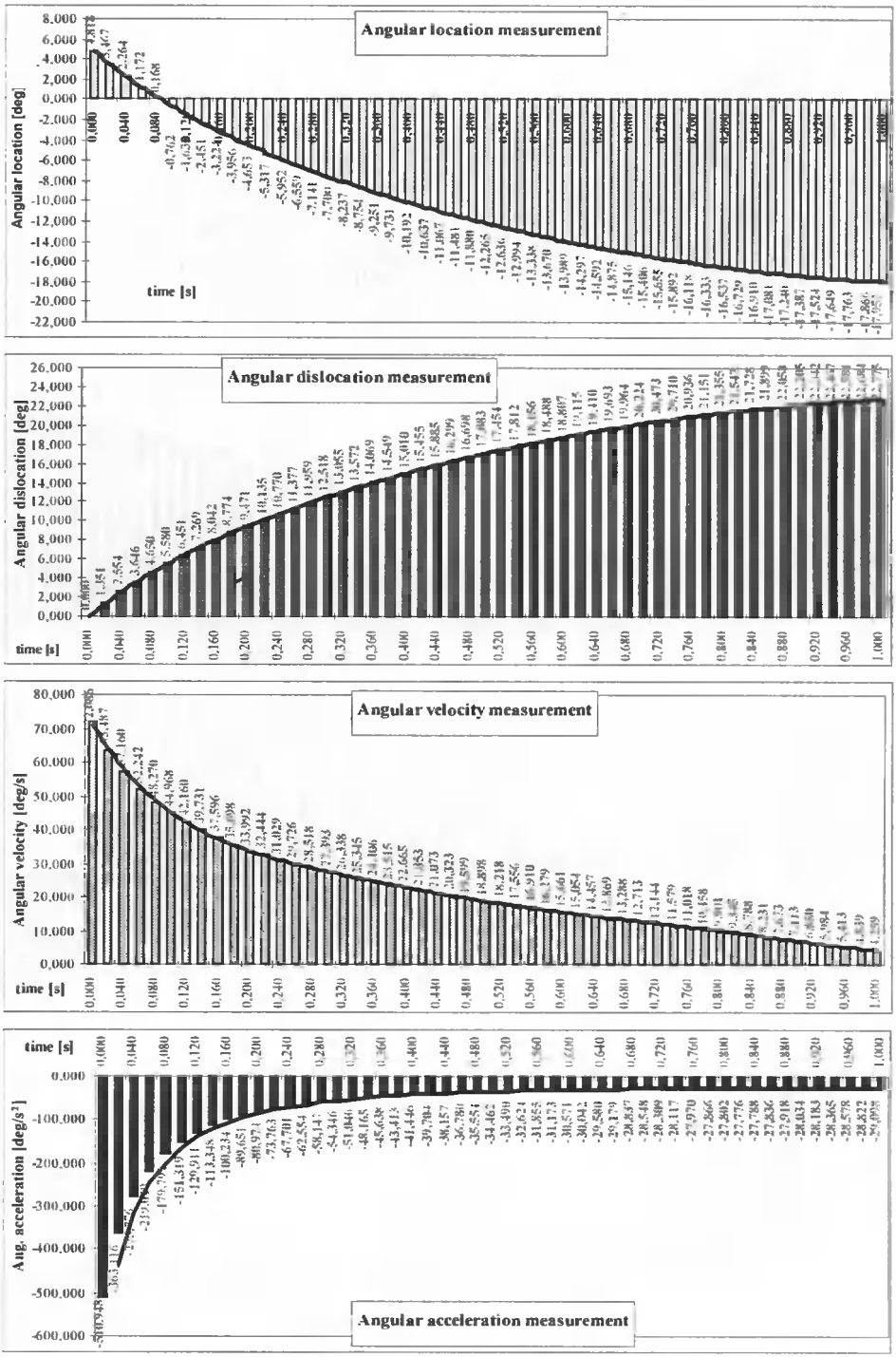

Fig. 13. Shock absorber connector movement parameters values

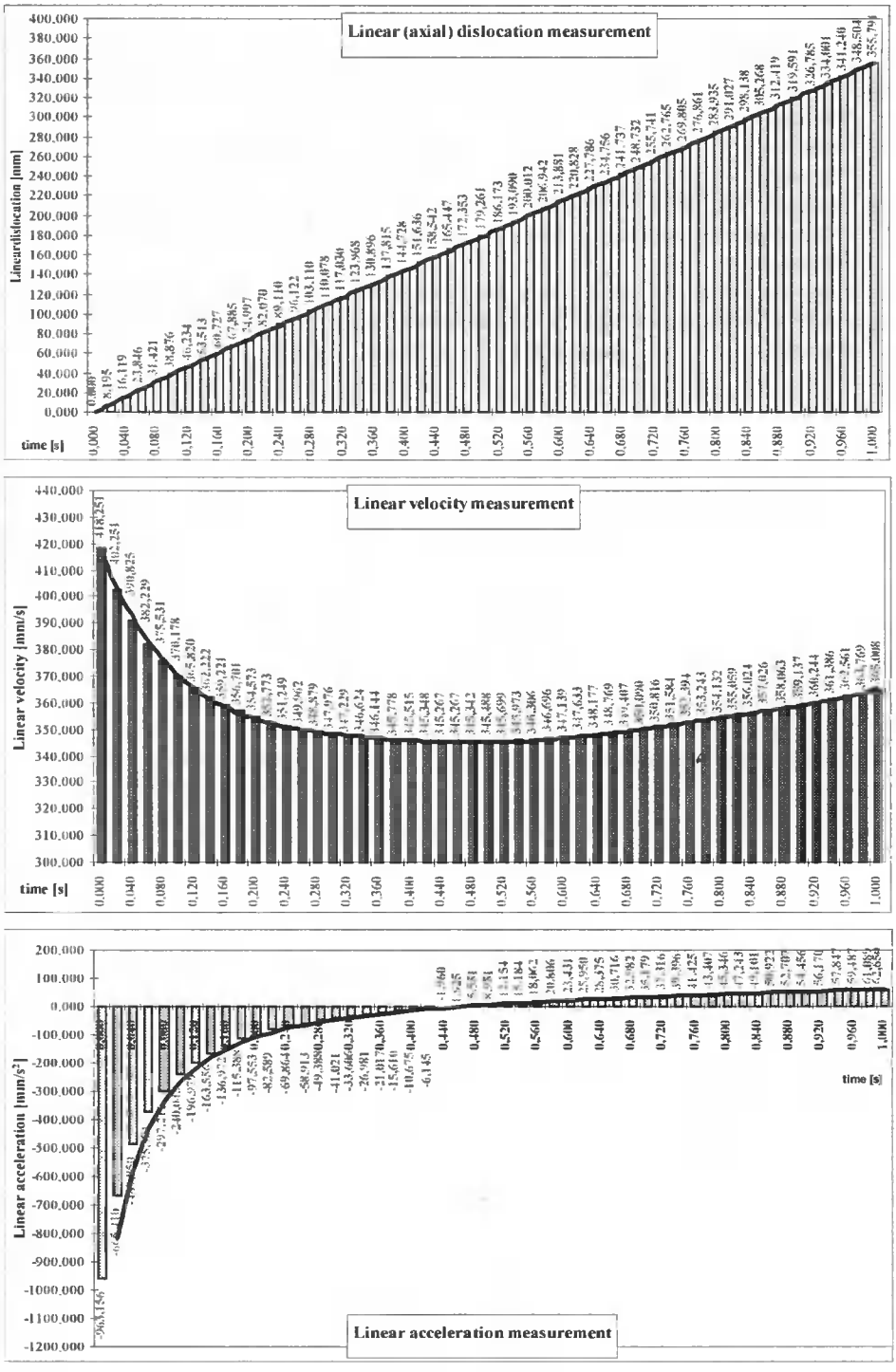

Fig. 14. Front wheel movement parameters values

REFERENCES

[1] Kaźmierczak G., 2001. Solid Edge 8/9. Helion Gliwice.
[2] Lewitowicz J., 2001. Podstawy eksploatacji statków powietrznych. ITWL Warszawa.
[3] Makowski T., 1992. Samoloty transportowe i komunikacyjne świata. Sigma Warszawa.
[4] Szulżenko M., 1975. Курс конструкции самолетов. Машиностроение Moskwa.
[5] Praca zbiorowa pod red. J. Modrzewskiego, 1978. Technika wojskowa. WMON Warszawa.
[6] Praca zbiorowa pod red. S. Szczecińskiego, 1992. Pionowzloty. WKŁ Warszawa.
[7] Praca zbiorowa pod red. S. Szczecińskiego, 1988. Technika lotnicza. WKŁ Warszawa.

Mieczysław Gawda

University of Technology and Agriculture
Department of Control and Machinery Design
Prof. S. Kaliskiego 7, 85-796 Bydgoszcz

Janusz Zachwieja

University of Technology and Agriculture
Department of Applied Mechanics
Prof. S. Kaliskiego 7, 85-796 Bydgoszcz

MODELING AND SIMULATION OF SINGLE ACTING PNEUMATIC CYLINDER

Summary: The work presents a linear model of single acting pneumatic cylinder with a return spring. For formulating equations describing the model there was used Lagrange's equation with the assumption of isothermic character of gas transformation occurring in the cylinder. Coupled differential equations of the first and second order were received, for whose solution the methods of Runge-Kutty were used. In the calculations pressure changes in the workchamber, the velocity and position of the piston in a time function were determined. Changeable parameters additionally included: the piston rod balance force, friction force, spring stiffness and the work factor temperature. Numerical algorithm constituted an element of the computer program elaborated by the authors to make the cylinder operation simulation possible. Two variants of servomotor work chamber supply were analyzed. In the first case the factor flow intensity was assumed to be constant in time, whereas, in the second case the flow intensity relation on pressure changes in the chamber was considered

Keywords: pneumatic cylinder, modeling, numerical algorithm

1. INTRODUCTION

Pneumatic drive sets perform a very important task in automatic systems and their main advantages are functioning reliability and simplicity. Automatic drive theory started to develop not a long time ago because of the complexity of processes occurring in pneumatic devices, which have not been fully accounted for so far. For further investigations it is necessary to take into account the true character of gas transformations which occur in the work chamber as well as the piston motion resistance. These factors are changeable in time.

Dynamics of a typical actuator is described by a system of nonlinear differential equations which, in a finite form, are unsolvable. Various simplifications have been suggested so far, such as: the constant air pressure in one or in both cylinder chambers, uniform or uniformly accelerated motion of the piston, or thermodynamic process isothermity in the cylinder. In order to meet the users' more and more strict requirements concerning the accuracy of a calculation method, it seems advisable to consider the so-far neglected factors such as: load and friction forces changeability, and heat exchange with the environment.

The general system of nonlinear differential equations is a mathematical record of single acting pneumatic cylinder dynamics in which simultaneous filling and emptying of work chambers take place. For the investigations of pneumatic actuators it is necessary to consider equations of motion and their elements together with the equations describing thermodynamic processes.

2. DESCRIPTION OF SINGLE ACTING PNEUMATIC PISTON CYLINDER WORK

Fig. 1 shows a scheme of single acting pneumatic cylinder with return spring. The movement of the piston and elements connected with it occurs after switching the distribution valve with signal Y. Compressed air with supply pressure p_z is supplied to the chamber of a cylinder with the volume causing pressure increase p_z in the filled chamber. Pressure p acting on piston surface A generates a force which overcomes the friction resistance, and a force resulting from the stiffness of the spring k, putting the piston into motion. After switching the distribution valve into the output position and connecting the servomotor chamber with the environment with pressure p_0, a return motion of the piston follows.

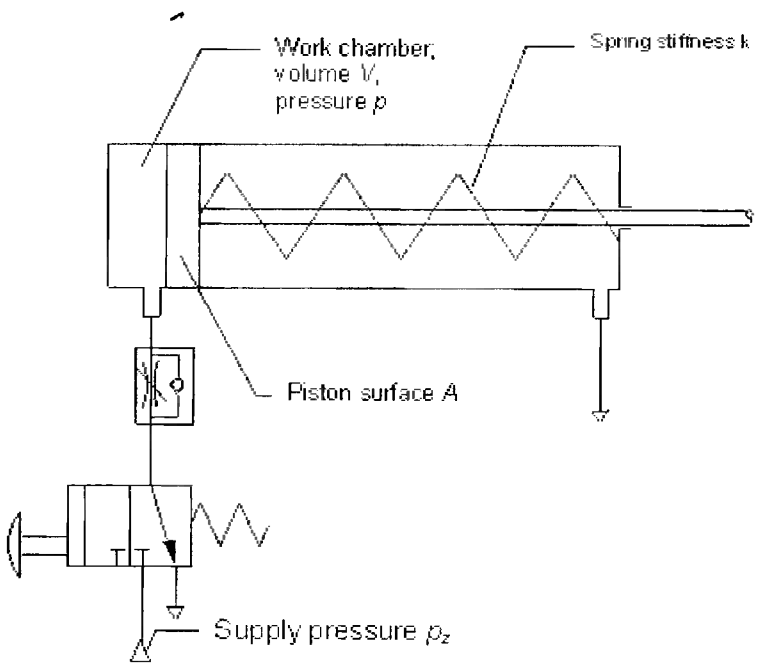

Fig. 1. Pneumatic single-acting servomotor

3. MATHEMATICAL MODEL OF SINGLE ACTING PNEUMATIC CYLINDER

The air mass in the chamber in front of the piston is a function of parameters of the state i.e. pressure, temperature and volume. It is described by:

$$m = \frac{pV}{RT} \tag{1}$$

where:

T – temperature,
p – pressure,
V chamber volume,
R gas constant.

Differentiating the equation in relation to time, we get:

$$\frac{dm}{dt} = \frac{1}{RT}\left(V\frac{dp}{dt} + p\frac{dV}{dt}\right) \tag{2}$$

Considering the piston movement changing the work chamber volume, we obtain:

$$\begin{aligned} V &= V_0 + dV = A(x_0 + x) \\ p &= p_0 + dp \end{aligned} \tag{3}$$

Taking into account the dependence (2) in equation (1) it yields:

$$\frac{dm}{dt} = \frac{1}{RT}\left[(V_0 + dV)\frac{dp}{dt} + (p_0 + dp)A\frac{dx}{dt}\right] \tag{4}$$

On the other hand, an increase in the air mass depends on supply pressure in the chamber:

$$\frac{dm}{dt} = \dot{Q}(t) = \alpha[p_z - p(t)] \tag{5}$$

Comparison of dependences (4) and (5) yields:

$$\frac{1}{RT}\left[V_0\frac{dp}{dt} + p_0 A\frac{dx}{dt}\right] = \alpha[p_z - p(t)] \tag{6}$$

In equation (6) small summands of higher order were neglected. After ordering summands, it assumes the form (7):

$$\frac{V_0}{\alpha RT}\frac{dp}{dt} + p(t) = p_z - \frac{p_0 A}{\alpha RT}\frac{dx}{dt} \tag{7}$$

The piston motion equation results from energy and external force work balance (Lagrange's second-order equation):

$$\frac{d}{dt}\left(\frac{\partial E_k}{\partial \dot{x}}\right) - \frac{\partial E_k}{\partial \dot{x}} + \frac{\partial E_d}{\partial \dot{x}} + \frac{\partial E_p}{\partial x} = F \tag{8}$$

whereas:

$E_k = \frac{1}{2}m\dot{x}^2$ piston kinetic energy,

$$E_d = \frac{1}{2}c\dot{x}^2 \quad \text{– dissipation energy,} \tag{9}$$

$$E_p = \frac{1}{2}kx^2 \quad \text{– piston potential energy,}$$

$$F = [p(t) - p_0]A \quad \text{– external forces resultant.}$$

Including the dependence (9) in the equation (8) yields:

$$m\frac{d^2x}{dt^2} + c\frac{dx}{dt} + kx = [p(t) - p_0]A \tag{10}$$

An assumption was accepted that the initial pressure was the same on both sides of the piston. Equations (7) and (10) form a system describing changes in pressure, piston velocity in a time function with the assumption that gas transformations in the cylinder are of isothermal character. To solve this system of differential equations, the method of Runge-Kutty was used.

Denoting:

$$\frac{dx}{dt} = v \tag{11}$$

We can write down:

$$\begin{aligned} &\frac{V_0}{\alpha RT}\frac{dp}{dt} + p(t) = p_z - \frac{p_0 A}{\alpha RT}v \\ &m\frac{dv}{dt} + cv + kx = [p(t) - p_0]A \end{aligned} \tag{12}$$

Relations (11) and (12) are written down in the form suitable for the algorithm of Runge-Kutty:

$$\begin{aligned} &\frac{dp}{dt} = \frac{\alpha RT}{V_0}[p_z - p(t)] - \frac{p_0 A}{V_0}v \\ &\frac{dz}{dt} = \frac{1}{m}[(p(t) - p_0)A - cv - kx] \\ &\frac{dx}{dt} = v \end{aligned} \tag{13}$$

For equation (13) dimensionless values will be introduced:

$$\begin{aligned} &\tilde{x} = \frac{x}{L} \\ &\tilde{p}(t) = \frac{p(t)}{p_0} \\ &p_z = \frac{p_z}{p_0} \\ &\tilde{v} = \frac{v}{L} \quad \left(\text{dimension} \quad \frac{1}{s}\right) \end{aligned} \tag{14}$$

With the equations (13) assume the form:

$$\begin{aligned}
\frac{dp}{dt} &= \frac{\alpha RT}{V_0}\left[p_z - p(t)\right] - \frac{AL}{V_0}\hat{v} \\
\frac{d\hat{v}}{dt} &= \frac{1}{m}\left[\frac{Ap_0}{L}(p(t)-1) - c\hat{v} - k\hat{x}\right] \\
\frac{dx}{dt} &= \hat{v}
\end{aligned} \tag{15}$$

The above equations describe the case in which the air flow intensity is not constant, but depends on the difference between the initial pressure in the cylinder chamber and supply pressure. If we assume a simplified condition allowing a constant air flow intensity from the supply source to the cylinder chamber, that is:

$$\frac{dm}{dt} = \dot{Q}(t) = const \tag{16}$$

then differential equation system of the piston motion and pressure changes in the cylinder chamber assumes the following form:

$$\begin{aligned}
\frac{dp}{dt} &= \frac{1}{V_0}\left[\frac{\dot{Q}RT}{p_0} - AL\hat{v}\right] \\
\frac{d\hat{v}}{dt} &= \frac{1}{m}\left[\frac{Ap_0}{L}(p(t)-1) - c\hat{v} - k\hat{x}\right] \\
\frac{dx}{dt} &= \hat{v}
\end{aligned} \tag{17}$$

Table 1. Selected parameters of the cylinder analyzed

Sprig stiffness	k	[N·m^{-1}]	692
Viscosity coefficient of friction	c	[Ns·m^{-1}]	1.7
Piston stroke	x	[m]	0.025
Piston section area	A	[m^2]	0.00125
Moveable parts mass	m	[kg]	0.15
Temperature	T	[K]	293
Initial air pressure in the cylinder work chamber	p_0	[Pa]	1E+5
Initial volume of the cylinder work chamber	V_0	[m^3]	6.3E-06
Input coefficient	α	[ms]	1E-10
Flow intensity mass	$\dot{Q}$	[kg·s^{-1}]	2.00E-05
Supply pressure	p_z	[Pa]	2.5E+5

4. DISCUSSION AND CONCLUSIONS

A computer cylinder operation simulation developed by Festo; model AVL– 40–25A, ESN–10–P was carried out. In this paper, computer simulation of the cylinder AVL–40–25A work was carried out. It is a single-acting pushing short-stroke cylinder.

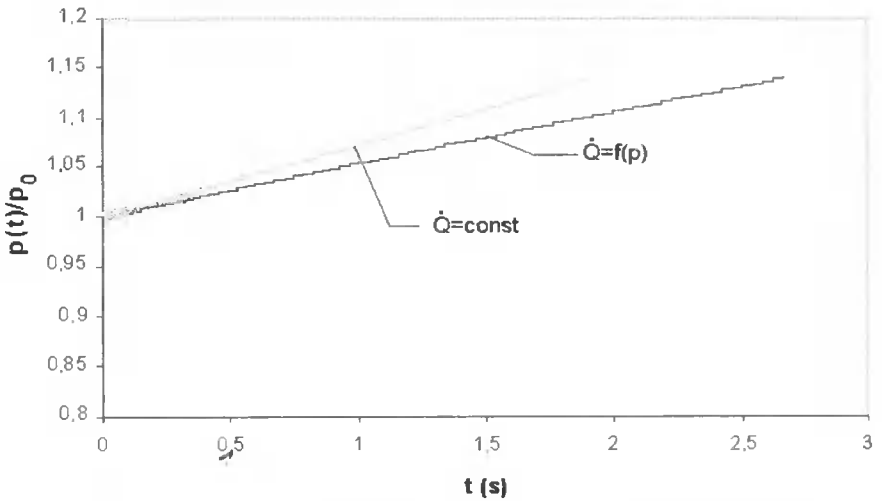

Fig. 2. Pressure changes in the cylinder work chamber as a function of time

For calculations, the catalogue data (Table 1) determined on the basis of laboratory research were accepted.

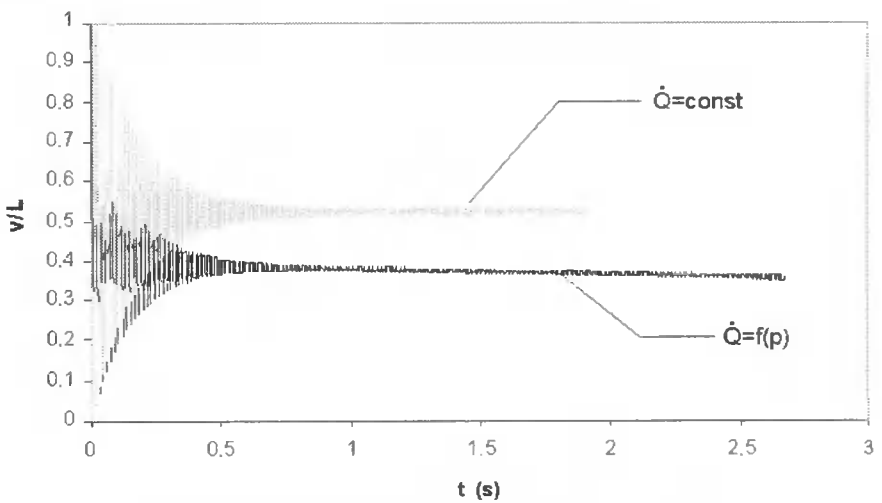

Fig. 3. Velocity of the piston stroke as a function of time

The achieved pressure dependencies in the chamber and velocities of the piston as a time function: $p = f(t)$, $v = f(t)$ were presented in Fig. 2 and Fig. 3. Curves 1 comply with the constant flow intensity condition. Curves 2 show changes in

parameters with the assumption that the flow intensity of the supply factor depends on the pressure in the work chamber, i.e. ($\dot{Q} = f(p)$).

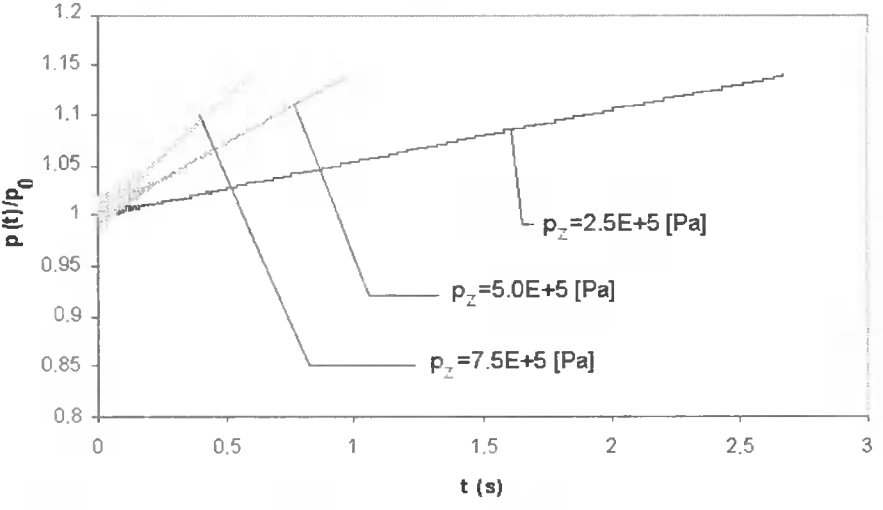

Fig. 4. Pressure changes in the work chamber of the cylinder as a time function and supply pressure

Even for a very small volume of the cylinder work chamber and a short stroke a quantitative difference in these parameters changes is visible even though their character i.e. the velocity and a pressure fluctuation in the initial period of the piston stroke is the same. A pressure rise increases the fluctuation range making the piston motion less constant (Fig. 4, Fig. 5).

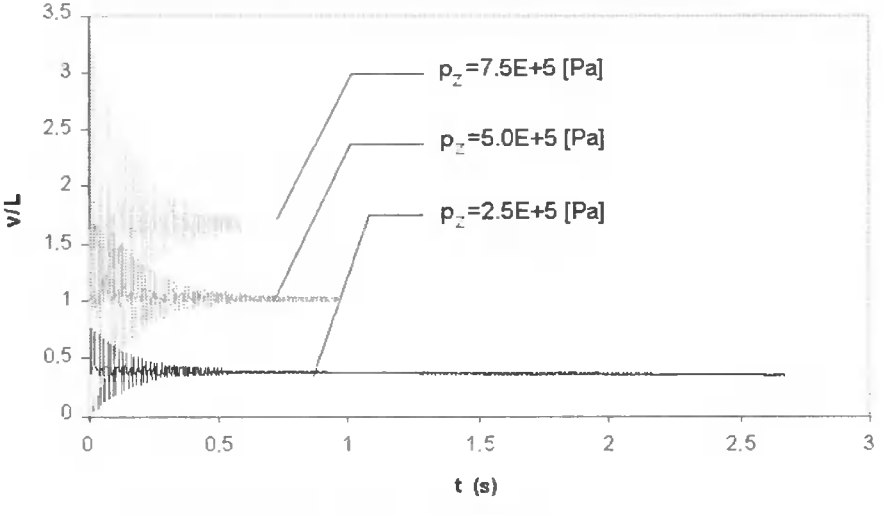

Fig. 5. Piston stroke velocity as a function of time and supply pressure

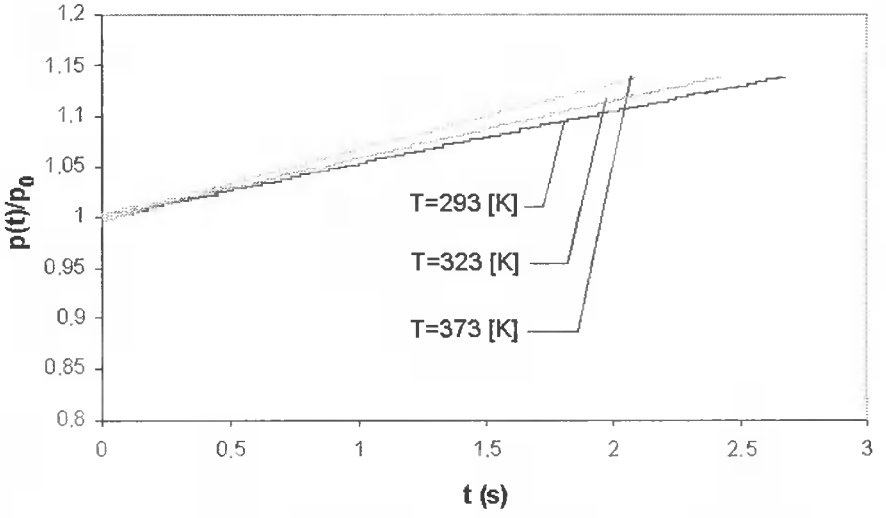

Fig. 6. Pressure changes in the cylinder work chamber as a time function and the work temperature

Temperature of the working factor has a similar impact on the cylinder as the supply pressure change (Fig. 6, Fig. 7).

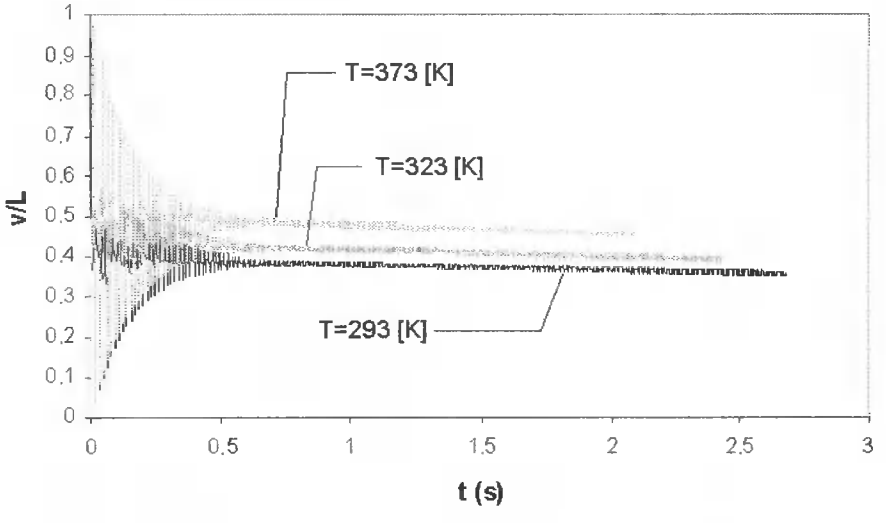

Fig. 7. Velocity of piston stroke as a time function and work temperature

Friction of viscous character shows a dumping effect on pressure changes and the cylinder velocity stabilizing its motions (Fig. 8 and Fig. 9). It can be then concluded that whenever it is very important to achieve great precision of the engine positioning, especially, in the range of its small strokes, cylinder motors with a high viscous friction coefficient value should be used as the change in spring stiffness does not create such conditions (Fig. 10).

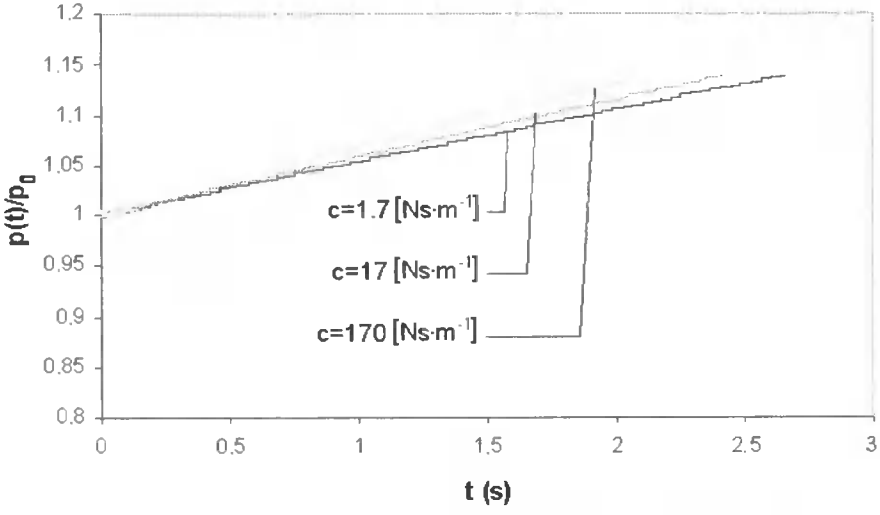

Fig. 8. Pressure changes in the work chamber of the cylinder as a time function

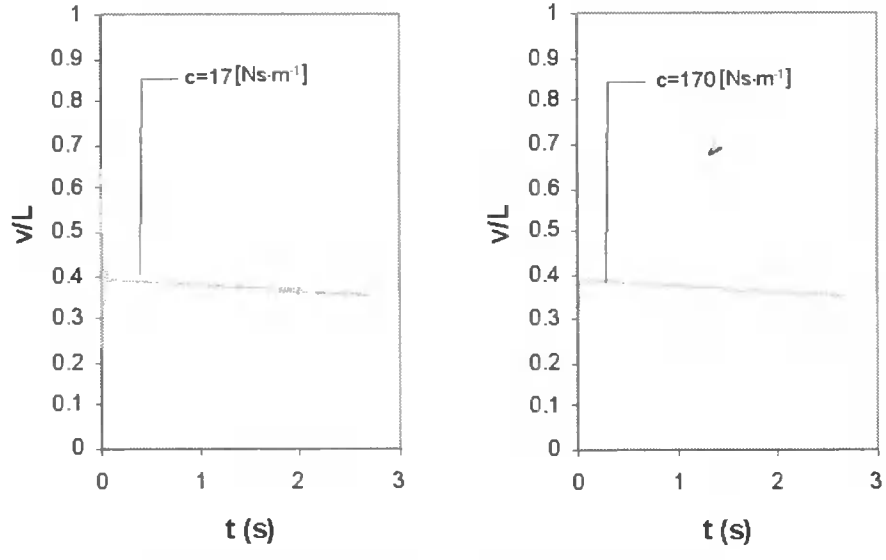

Fig. 9. Piston stroke velocity as a time function and viscous friction

Due to the convergence conditions, in order to verify the results, additionally equation system (15) was sold by means of Fehler's method and the differences in results were non-significant. Using the Runge-Kutty' method with an automatic choice of integration step optimized the calculation time.

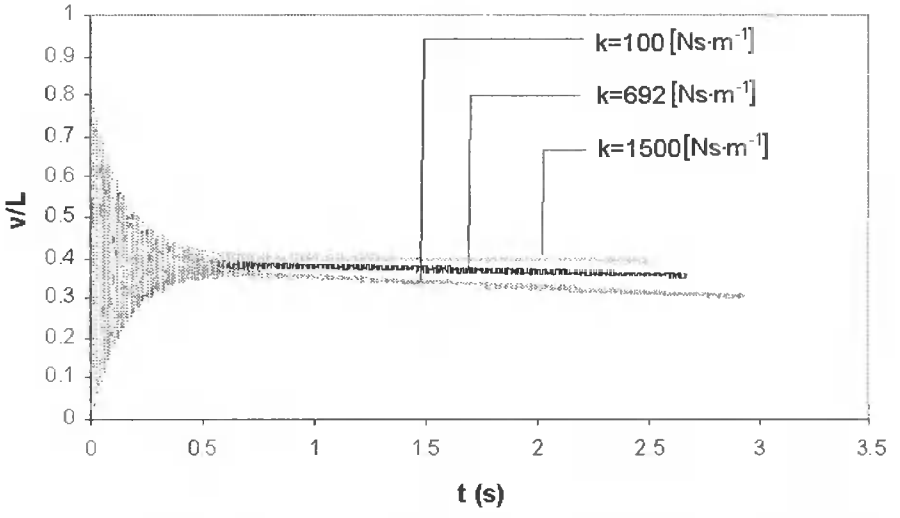

Fig. 10. Cylinder velocity changes of cylinder as a time function and spring stiffness

REFERENCES

[1] Gerc E.W., 1973. Napędy pneumatyczne. Teoria i obliczanie. WNT Warszawa.
[2] Kamiński L.M., 1996. Własności dynamiczne pneumatycznego siłownika jednostronnego działania. Zesz. Nauk. ATR w Bydgoszczy, Mechanika 40, 55-64.
[3] Szenajch W., 1992. Napęd i sterowanie pneumatyczne. WNT Warszawa.
[4] Schulz J., 1984. Próba określenia wpływu czasu spoczynku na siłę tarcia statycznego pneumatycznego siłownika tłokowego. Zesz. Nauk. ATR w Bydgoszczy, Mechanika 26, 37-51.
[5] Katalog FESTO, 2000. Program produkcyjny – 01/03.
[6] Iwaszko J., 1999. Opory przepływu powietrza przez elementy pneumatyczne. Oficyna Politech. Warszawskiej, Prace Nauk. 177.
[7] Szymański M., Łukasiewicz J., 2001. Termodynamika. Wyd. Uczeln. ATR w Bydgoszczy.

Jan Hošek
Zdeněk Trávníček

Institute of Thermomechanics
Academy of Sciences of the Czech Republic
Dolejškova 5, 182 00 Prague 8, Czech Republic

Kazimierz Peszyński

University of Technology and Agriculture
Department of Control and Machinery Design
Prof. S. Kaliskiego 7, 85-796 Bydgoszcz, Poland

NUMERICAL MODELING OF FLUIDIC FLIP-FLOP JET SWITCHING

Summary: This paper deals with numerical simulation of an annular, actively-controlled, fluid jet. The jet is generated by means of fluidic principles, thus no mechanical movable parts are applied. The present numerical investigation was performed using a commercial CFD code FLUENT, and it resulted in a better understanding of control process as well as in a further improvement of the particular nozzle geometry. A better location of the control jet has been designed. All the present numerical results have been confirmed experimentally in collaborative investigations.

Keywords: jets, flow control, fluidics, nozzle, numerical simulation, CFD

1. INTRODUCTION

Studies of submerged jet flows, as a part of fluid mechanics, involve many theoretical problems such as the stability phenomenon, laminar-turbulent transition, fluid entrainment, and mixing. The jets are utilized in various applications such as the propulsion of aircrafts and rockets, burners, mixers, etc. An interaction of the jet with a solid surface is of fundamental importance both for fluid dynamics and heat/mass transfer [1]. The so-called impinging jets can achieve very high heat/mass transfer onto the exposed wall as well as a very good adaptability to different surface shapes. Moreover, the applications can be relatively simple and cost-effective. Therefore, impinging jets are used in many applications for cooling (electronic component, turbine blades), heating, drying, etc. [2].

There are at least two essential advantages of numerical simulation of a jet impingement configuration which have motivated the present approach. Firstly, a great number of parameters affect the complex flow field and resulting heat mass transfer. A better understanding of the flow field and heat mass transfer processes requires distinguishing between all of these effects. Apparently, to examine the effects separately by means of experiments is extremely difficult due to the task complexity. Moreover, a comparison of experiments performed by different authors is often problematic because of different experimental conditions (different facilities, laboratories, methods, etc.). On the contrary, a numerical approach to the complex problem can identify and quantify particular influences more easily.

Secondly, an experimental investigation focused on a jet impingement system needs typically a great number of experiments. The design of many geometry variants, their manufacturing and experimentation need some time as well as financial recourses. Obviously, numerical simulations can radically reduce the number of experimentally investigated variants.

The aim of the present numerical modeling is to evaluate the flow field sensitivity to the control jet, particularly to the control nozzle location, and to the control flow rate. The numerical modeling is considered as a basis for a design and manufacturing of a new geometry variants. The numerical solution can (more or less) depend on methods and turbulence models, therefore it is meaningful to use it for relative comparisons (and with a careful interpretation). Results can be considered reliable only if a proper experimental validation is carried out in a subsequent step.

2. INVESTIGATED GEOMETRY

This work focuses on a bistable behavior of annular jets. An annular impinging jet was studied numerically by Kokoshima et al. [3], and a bistable behavior was predicted including a hysteresis character. Experimental investigation of annular impinging jets was presented by Maki and Yabe [4]; four flow regimes were identified, and three of them were characterized as a recirculating unsteady flow.

The bistability phenomenon was studied experimentally by Trávníček and Křížek [5] for a planar geometry. A two-dimensional impinging jet from a two-slot-nozzle (slot nozzle which is halved by a partition bar) has been investigated, and bistable switching and hysteresis effects were studied (flow visualization, measurements of pressure, and mass transfer) [5, 6].

A recent study by Tesař [7] presents an annular jet, when five flow regimes were identified by a numeric simulation, including bistability on a demarcation between two of them. Surprisingly, no hysteresis was referred to in [7], the phenomenon is, apparently, uncommon, but it depends on a specific geometry.

An idea of a planar jet, which is flipping by a control feedback loop as a fluidic oscillator, was originally suggested by Viets [8]. An annular bistable nozzle with a fluidic control was designed recently by Tesař, Peszyński [9, 10]. The nozzle design was based primarily on experience and intuition, a refinement of geometry has been supported by an experimental as well as numerical investigations in follow-up variations [2, 9, 11, 12]. Performance analysis of previous nozzle geometry has shown that a more systematic approach based on both experimental and numerical approaches can be very effective for the nozzle development. Moreover, an evident need of heat/mass transfer experiment has appeared. These were main motivations for the present experimental and numerical investigation of flow field and for naphthalene mass transfer experiment.

Fig. 1 shows schematic view on the present nozzle. Upstream of the nozzle, the main airflow passes through a horizontal tube; the control flow passes through a central tube. The main nozzle is annular, its outside and inside exit diameters are $D = 84.0\,\mathrm{mm}$ and $d = 74.0\,\mathrm{mm}$, respectively. The main nozzle contraction is 1.30 against the supply. The control nozzle is a radial slot $\Delta_c = 0.5\,\mathrm{mm}$ wide, its location is defined by a distance from the main nozzle exit, x_c (see Fig. 4 below); three variants were studied with x_c of 0.0, 10.0, and 15.0 mm.

The nozzle is equipped with the spoiler (flow divider) and a ventilation slot (see Fig. 1), the geometry of both was designed during previous investigation. A function of the spoiler and a ventilation slot is to suppress an undesirable hysteresis effect, which can occur during a jet switching, which was discussed in [2].

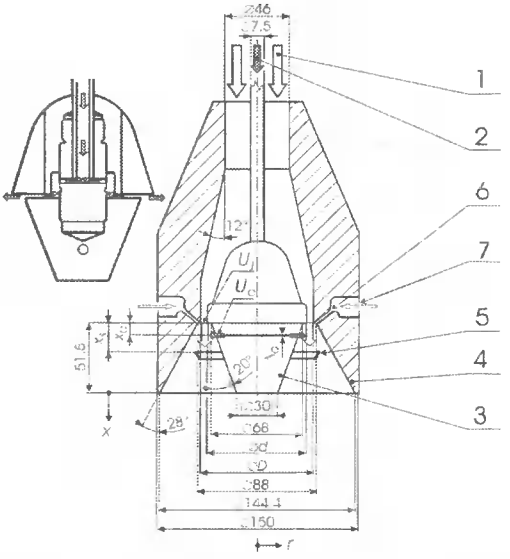

Fig. 1. Annular nozzle with the fluidic control. 1 : main flow supply, 2 : control flow supply, 3 : inner nozzle cone, 4 : outer nozzle cone, 5 : spoiler, 6 : ventilation slot, 7 : vent flow. Dimensions: $D = 84\text{mm}$, $d = 74\text{mm}$, $\Delta_C = 0{,}5\text{mm}$, $x_C = 0.0$, or 10.0, or 15.0mm, $x_s = 15.3$, or 20.0, or 25.0mm

The present numerical modeling has been performed in relation to the experiments described in [2], flow visualization, hot-wire velocity measurement, and mass transfer measurements by means of naphthalene sublimation.

3. NUMERICAL MODELING

Governing equations. The fluid flow is assumed to be incompressible, isothermal, turbulent, and statistically stationary. The fluid properties (density and viscosity) are assumed to be constant. With these simplifications, the following set of equations governs the mean velocity flow field: continuity equation, time-averaged momentum (Navier–Stokes) equations.

The equation for conservation mass, or continuity equation in Cartesian coordinates $i, j, l = 1,2,3$:

$$\frac{\partial \rho}{\partial t} + \frac{\partial}{\partial x_l}(\rho u_l) = S_m \tag{1}$$

where the Einstein summation rule is used, i.e., $\frac{\partial}{\partial x_l}(\rho u_l) = \sum_{l=1}^{3} \frac{\partial}{\partial x_l}(\rho u_l)$, and S_m are mass sources.

For 2D axisymmetric geometries, the continuity equation is given by:

$$\frac{\partial \rho}{\partial t} + \frac{\partial}{\partial x}(\rho u) + \frac{\partial}{\partial r}(\rho v) + \frac{\rho v}{r} = S_m \tag{2}$$

where x is axial coordinate, r is radial coordinate, u is axial velocity and v is radial velocity.

Momentum conservation equation:

$$\frac{\partial}{\partial t}(\rho u_i) + \frac{\partial}{\partial x_j}(\rho u_i u_j) = -\frac{\partial p}{\partial x_i} + \frac{\partial \tau_{ij}}{\partial x_j} + \rho g_i + F_i \tag{3}$$

where p is the static pressure, τ_{ij} is the stress tensor (described below), ρg_i is gravitational body force and F_i are external body forces.

The stress tensor τ_{ij} is given by

$$\tau_{ij} = \left[\mu\left(\frac{\partial u_i}{\partial x_j} + \frac{\partial u_j}{\partial x_i}\right)\right] - \frac{2}{3}\mu\frac{\partial u_l}{\partial x_l}\delta_{ij} \tag{4}$$

where μ is the molecular viscosity and the second term on the right is the effect of volume dilatation. The δ_{ij} is the Kronecker unit tensor ($\delta_{ij} = 1$ for $i = j$, $\delta_{ij} = 0$ for $i \neq j$).

For 2D axisymmetric geometries, when the gravitational body force is omitted, the axial and radial momentum conservation equations are given by:

$$\begin{aligned}&\frac{\partial}{\partial t}(\rho u) + \frac{1}{r}\frac{\partial}{\partial x}(r\rho uu) + \frac{1}{r}\frac{\partial}{\partial r}(r\rho vu) = \\ &= -\frac{\partial p}{\partial x} + \frac{1}{r}\frac{\partial}{\partial x}\left[r\mu\left(2\frac{\partial u}{\partial x} - \frac{2}{3}(\nabla\cdot\vec{v})\right)\right] + \frac{1}{r}\frac{\partial}{\partial r}\left[r\mu\left(\frac{\partial u}{\partial r} + \frac{\partial v}{\partial x}\right)\right] + F_x\end{aligned} \tag{5}$$

$$\begin{aligned}&\frac{\partial}{\partial t}(\rho v) + \frac{1}{r}\frac{\partial}{\partial x}(r\rho uv) + \frac{1}{r}\frac{\partial}{\partial r}(r\rho vv) = -\frac{\partial p}{\partial r} + \frac{1}{r}\frac{\partial}{\partial r}\left[r\mu\left(2\frac{\partial v}{\partial r} - \frac{2}{3}(\nabla\cdot\vec{v})\right)\right] + \\ &+ \frac{1}{r}\frac{\partial}{\partial x}\left[r\mu\left(\frac{\partial u}{\partial r} + \frac{\partial v}{\partial x}\right)\right] - 2\mu\frac{v}{r^2} + \frac{2}{3}\frac{\mu}{r}(\nabla\cdot\vec{v}) + \rho\frac{w^2}{r} + F_r\end{aligned} \tag{6}$$

where w is the swirl velocity (despite the 2D axisymmetric geometry, the solver uses this component); and the divergence of the velocity vector $\vec{v}$

$$\nabla\cdot\vec{v} = \frac{\partial u}{\partial x} + \frac{\partial v}{\partial r} + \frac{v}{r} \tag{7}$$

The turbulent kinetic energy equation and turbulent energy dissipation equation depend on the used turbulent model. For the renormalization group (RNG), $k-\varepsilon$ turbulence model was used [12].

CFD code and computing. The flow fields is computed with the commercial finite-volume code FLUENT [12], in implicit formulation, in absolute velocities (computing of impinging jets by means of the same solver has been discussed recently by Garimella, [1]). The problem to be solved has been simplified to be axisymmetric. The jet was solved only in one half of the meridian plane to decrease the number of mesh volumes. The problem of reducing from 3D to 2D axisymmetric had significant

influence to the computer time and the number of solved geometry variants have increased. This simplification has no significant effect on the simulation of both steady stages of the flow in the jet. On the other hand no asymmetrical effects can be simulated by this simplified solution. These asymmetrical effects can be expected especially during switching of the main flow between both stages. It implied that computed solutions could not give a true picture of the hysteresis effects for this case of simplification.

Continuity and momentum equation are coupled by the SIMPLE algorithm which works in predictor corrector steps, [14]. A standard scheme is used for the pressure discretization, and first order upwind is used in the momentum, turbulent kinetic energy, and turbulent energy dissipation equations.

The multi-grid method to accelerate the convergence and iterative technique with under-relax predictions of the velocity and pressure are used. Because of the nonlinearity of the equations being solved, it is necessary to control the change in each variable (Φ). This is typically achieved by under-relaxation, which reduces the change in Φ produced during each iteration. In a simple form, the new value of the variable Φ within a cell depends upon the old value, Φ_{old}, the computed change in variable $\Delta\Phi$, and the under-relaxation factor, α, as follows:

$$\Phi = \Phi_{old} + \alpha\Delta\Phi \tag{8}$$

Default under relaxation factors of the solver were used, which are 0.3, 0.7, 0.8, and 0.8 for the pressure, momentum, turbulent kinetic energy, and turbulent energy dissipation, respectively.

The results of iterations are evaluated by means of convergence criteria based on residual evolutions. The solution was considered to be converged when the sum of normalized residuals was less than $1 \cdot 10^{-3}$.

The present computations were performed using multiprocessor Silicon Graphic computer, and usually took less than half an hour per task.

Turbulence model and the present near-wall modeling. The Boussinesq turbulent-viscosity concept is incorporated with the renormalization group (RNG) $k-\varepsilon$ turbulence model [12]. It has been chosen as sufficient for the present computation purposes, i.e. for a comparison of several variants, which differs in geometry or control flow rates. The RNG $k-\varepsilon$ model is recommended for a stagnation flow computation – [12]. In comparison with more sophisticated models (Reynolds Stress Model and Large-Eddy Simulation model are available in code FLUENT), the RNG $k-\varepsilon$ model requires a relatively shorter computing time.

Near wall modeling is based on the standard wall function. It is assumed that two distinct fluid layers exist in the near-wall regions very close to the wall, namely a viscous sublayer up to $y \approx 11.225$, and a fully turbulent logarithmic region above it [12]. The former exhibits dominant molecular viscosity, the latter dominant eddy viscosity, respectively. The default set of empirical constants was taken from [12]:

- $C_\mu = 0.0845$ (the eddy viscosity is calculated as $\mu_t = C_\mu \rho k^2 / \varepsilon$),
- $C_{1\varepsilon} = 1.42$, $C_{2\varepsilon} = 1.68$ (the constants in the turbulent energy dissipation equation),
- $\beta = 0.012$, $\eta_0 = 4.38$ (the constants of the strain-dependent turbulent production in the turbulent energy dissipation equation).

The domain, grid and boundary conditions. Nozzle geometry was used basically the same as at experiments (see Fig. 1). Fig. 2 shows the computational domain and grid. The grid was designed for an expected flow field in the jet geometry and is given with the symmetry in relation to the jet axis to reduce the number of volumes elements.

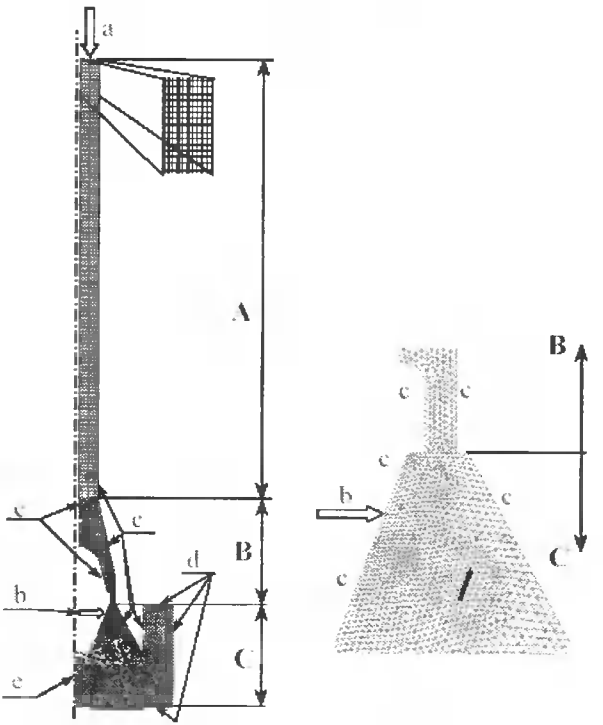

Fig. 2. Computational domain, grid, and boundary conditions. (a) entire domain, (b) detail of the grid near the nozzles and spoiler

The grid is composed of three grid areas, A, B, C, which are bound together. The first area, A, is located just behind the inlet; and it contains the pipe for the flow evolution. A is grid part designed to be structured rectangle grid for laminar flow in this chamber. The next two grid areas, B and C, contain the contraction (located upstream the nozzle lip) and final part (downstream the nozzle lip), respectively. B and C grid parts are designed as unstructured grid of triangles, due to a rapid change in flow regime expected in these two areas. The density of grid elements is also changed to enhance the density of the grid at the main nozzle lip as well as in the parts of expected higher flow velocity (in both areas A and B).

The grid is generated by GAMBIT 1.3.0; generator associated with the solver. Numbers of volumes (2D axisymmetric zones) and nodes were 19886 and 8208. A refined grid at both main and control nozzles makes it possible to capture a strong velocity gradient of the jet shear layers.

Grid independence was tested using the Grid Adaptation Procedure of the FLUENT code. The grid was refined according to velocity gradients and numbers of cells and nodes were increased 3.6-4.0 times. However, the problems with a convergence required a decrease in all the under-relaxation factors approximately into half-values.

Therefore a negligible effect on the computed flow field has been found, see Fig. 6 (c), (d), and their short comment later.

Input data. The prescribed boundary conditions (a-e) are plotted in the Fig. 2, where respective letters stand for:

a) Inlet of the main flow: since the tube length was set to be long enough (500 mm), the velocity profile at the inlet was set as uniform, $U_{in} = 6.52\,\mathrm{m \cdot s^{-1}}$ (i.e., $U_j = 8.50\,\mathrm{m \cdot s^{-1}}$, $\mathrm{Re}_D = 49400$, $\mathrm{Re}_W = 2900$). The tube had $40.8\,\mathrm{mm}$ hydraulic diameter, a value of the turbulence intensity was chosen as $k = 3\%$.

b) Inlet of the control flow: the velocity profile at the control flow inlet was set as uniform, the velocity magnitude, U_c, varied from 0 to $30\,\mathrm{m/s}$. The turbulence intensity was chosen as $k = 3\%$.

c) Walls, including the spoiler surface: A no-slip boundary condition was employed on the walls (all velocity components are zero).

d) Outlet: A static pressure was prescribed as the reference value, 98000 Pa. It allows a recirculation flow (fluid entering the exit) at the outlet. The hydraulic diameter, and turbulence intensity (for fluid entering), were chosen 200 mm and 10%, respectively.

e) Nozzle axis: standard symmetry conditions were employed.

Fluid properties of working fluid (the air) were prescribed as follows: fluid density $\rho = 1.125\,\mathrm{kg \cdot m^{-3}}$, dynamic viscosity $\mu = 1.7894 \cdot 10^{-5}\,\mathrm{kg \cdot m^{-1} \cdot s^{-1}}$.

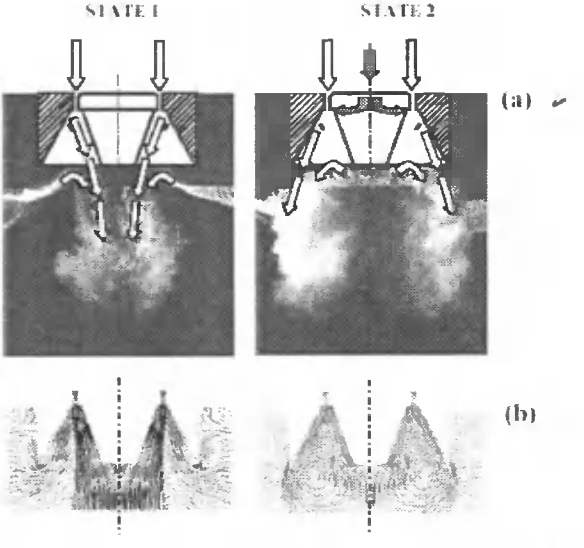

Fig. 3. Two states of the present annular jet. $x_c = 0$, without ventilation. (a) Smoke visualization mm at the $\mathrm{Re}_D = 23000$. ($\mathrm{Re}_W = 1400$. $U_j = 4.4\,\mathrm{m \cdot s^{-1}}$). $x_s = 15.3\,\mathrm{mm}$: $r_c = 0$ and 9.7% in state 1 and 2, respectively; (b) Computed pathlines at the $\mathrm{Re}_D = 49400$. ($\mathrm{Re}_W = 2900$. $U_j = 8.5\,\mathrm{m \cdot s^{-1}}$), without spoiler. $r_c = 0$ and 21.1% in state 1 and 2, respectively

4. RESULTS AND DISCUSSIONS

Fluidic control of the annular jet – two flow field states.

The present annular jet is characterized by two flow field states, see the results of the smoke visualization in photographs in Fig. 3 (a) (visualization experiments were described precisely in [2]):

- State 1, control jet is off. The air issuing from the main annular nozzle is inclined by means of Coanda Effect towards inner nozzle cone, reattaches some area of the cone surface, and continues along it. The resulting jet is focused along the nozzle axis.
- State 2, control jet is on. The air issuing from the main annular nozzle is immediately forced by control jet toward outer nozzle cone, reattaches a surface of outer cone, and flows along it. The resulting jet is spread in diagonal direction out of outer cone edge. A cross section area of the jet is larger and velocity lower, as compared with state 1.

Fig. 3 (b) shows a typical result of numeric simulation, namely the distribution of the time-mean pathlines in states 1 and 2. A reason for practically half-value Re_D of visualizations in Fig. 3 consists in experimental limits with visualization at higher flow velocities. Regardless of the values, a qualitative comparison of experiments and computed flow field pattern is quite satisfactory.

Effect of control nozzle location.

The motivation of this step is a consequence of the following contrast: the control jet has to be sufficient for a reliable jet state switching, but the control flow rate should be as small as possible (a low-energy demand).

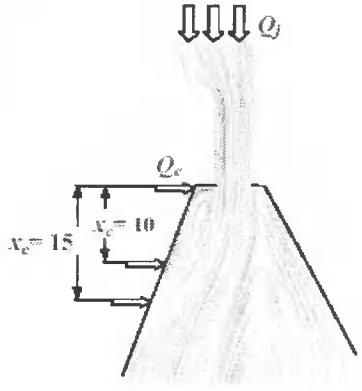

Fig. 4. Detail of flow field in state 1 from Fig. 3 (b) – separation "bubble" flow, and flow reattachment. Locations of three tested control nozzles ($x_c = 0$, 10, and 15mm) are plotted

A control nozzle location has been designed with a support of computing results. Fig. 4 shows the separation "bubble" flow and a flow reattachment in detail. The separation region is located from the inner nozzle lip up to the reattachment region on the inner cone. The most sensitive region of the flow field towards the intended control jet action is estimated near the reattachment region, approximately $x_c = 10\,\text{mm}$. The location of all three tested control nozzles ($x_c = 0$, 10, and 15mm) are plotted in

Fig. 4. The most sensitive region of the flow field towards the intended control jet action has been estimated near the reattachment region, (see, e.g. a dotted arrow in Fig. 6 (a)). Numerical simulation of the control nozzle locations $x_c = 10\,\text{mm}$, and $15\,\text{mm}$ was performed. Neither a spoiler nor ventilation was used. The control flow rate magnitude (U_c) varied from $5 \div 15\,\text{m}\cdot\text{s}^{-1}$ (dimensionless control flow rate r_c was $55 \div 21\%$).

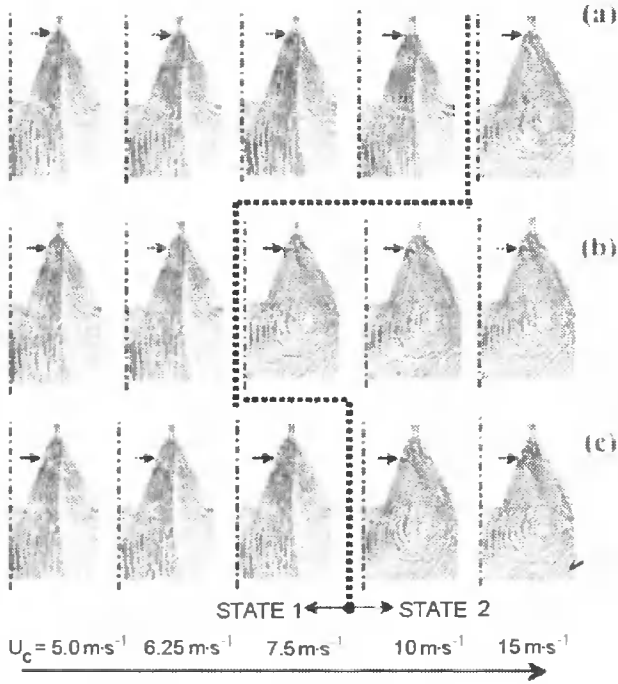

Fig. 5. Numerical simulation of the sensitivity of the bistable flow field to the control jet action. The dotted polyline represents a boundary between states 1 and 2. Neither spoiler nor vent was used. $\text{Re}_D = 49400$ (a) $x_c = 0\,\text{mm}$, (b) $x_c = 15\,\text{mm}$, (c) $x_c = 20\,\text{mm}$

Fig. 5 shows the computed pathlines. At a small control jet velocity, the flow field remains in state 1, similarly as without any control. If the control action is powerful enough, the main flow is switched into state 2. The dotted polyline represents a boundary between states 1 and 2, which occurs on the left and right from the polyline, respectively. Fig. 5 (b) shows clearly the best control nozzle location, namely $x_c = 10\,\text{mm}$, since the switching is achieved at the minimum control jet velocity, ($U_C = 7.5\,\text{m}\cdot\text{s}^{-1}$, i.e., $r_c = 9.4\%$). This result proves a high sensitivity of the flow field towards a control jet action near the reattachment region. Experimental confirmation was shown in [2].

Grid independence

Figs. 6 (a), (b) show the controlled jet inside the nozzle in detail. Computed mean pathlines are plotted for state 1 and 2, respectively. The result shows the proper function of the spoiler:

- In state 1 (Fig. 6 a), the main air stream passes the spoiler, thus its influence is relatively small.
- In state 2 (Fig. 6 b), the spoiler deflects permanently a small part of the jet centripetally. The resultant very complex flow field structure with many large vortices is not studied in detail, for the time being, a sufficient result is that the spoiler in state 2 counteracts the centrifugal control flow effect effectively (as proved experimentally in [2]).

Figs. 6 (c), (d) show results of computation performed using a refined grid. The grid was refined according to velocity gradients, and numbers of cells and nodes were increased 3.6 – 4.0 times. The problems with a convergence required to decrease all the under–relaxation factors approximately into half-values. A comparison of Figs. 6 (a), (b) with Figs. 6 (c), (d) demonstrates that an effect of the grid on computed flow fields can be neglected.

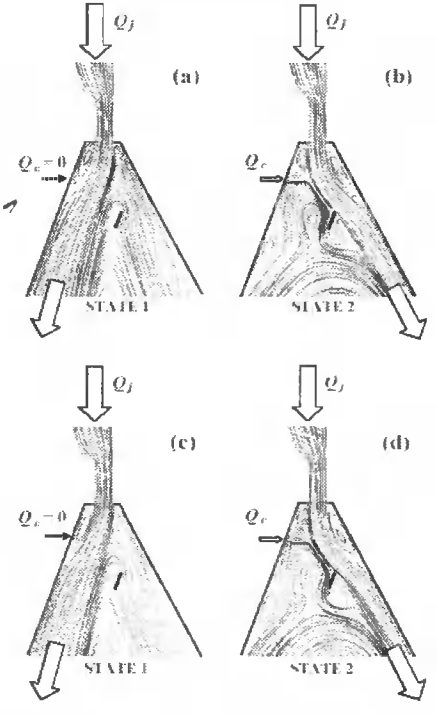

Fig. 6. Computed mean pathlines inside the nozzle in detail. $\mathrm{Re}_D = 49400$. $x_c = 10\,\mathrm{mm}$, $x_c = 20\,\mathrm{mm}$, without ventilation. (a) State 1, control is off, $r_c = 0$; (b) state 2, control is on, $r_c = 10.9\%$; (c) repeated computation of state 1 using a refined grid; (d) repeated computation of state 2 using a refined grid

Mean flow fields

Fig. 7 (a) shows computed velocity magnitude profiles, Fig. 7 (b) shows comparable results which were measured by means of hot-wire anemometer in [2]. The left column of figures shows state 1 (flow control off, $r_c = 0$), while the right one – state 2 (flow control on, $r_c = 10.9\%$). The computation and experiments are in quite

good qualitative agreement. The results correspond to the present concept of fluidic control - the jet is focused along the nozzle axis in state 1, or it is spread out in state 2. It is worth underlining here that this good agreement between the computed and measured results of fluidic control is an essential point for the present work.

Fig. 7 shows that a quantitative agreement is satisfactory in state 1. On the other hand, differences between the computation and the experiment are much bigger in state 2, a computed span of the velocity maxima is smaller than the measured one, thus the computed separation bubble is smaller. A reason can be that the present computation is focused on the jet switching, for which the present domain was designed. However, the present domain is too small for a correct computation of an annular jet development. Therefore an outlet of the domain is under a very strong influence of a large recirculation flow, and the computation near the outlet does not agree with the measurement.

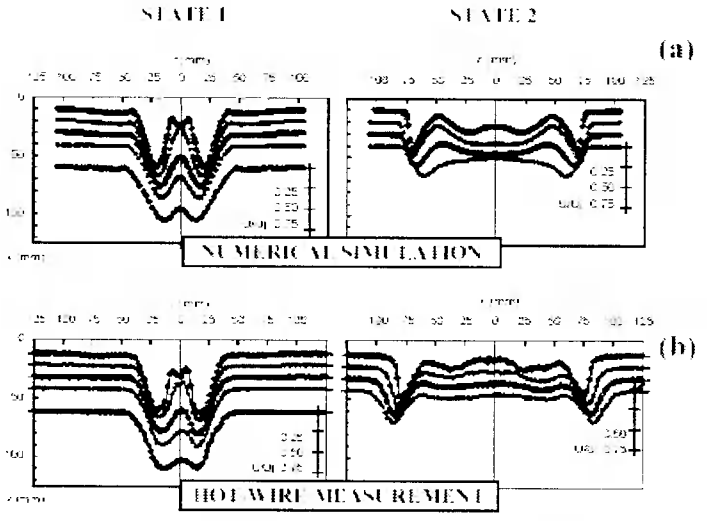

Fig. 7. Profiles of velocity magnitude. Left column of figures shows state 1 (flow control off, $r_c = 0$; $x = 10, 20, 30, 40, 60\,\text{mm}$), right column shows state 2 (flow control on, $r_c = 10.9\%$, $x = 10, 20, 30, 40\,\text{mm}$); $x_c = 10\,\text{mm}$, $x_s = 20\,\text{mm}$, without ventilation: (a) computation at $Rs_D = 49400$, (b) measurements at $Rs_D = 49000$

5. CONCLUSIONS

Numerical simulation of an annular actively-controlled jet has been performed. A design fundamental has been already known from the previous experimental study. Sequentially, a numerical simulation (using a commercial CFD code FLUENT 5.5.14) has given a basis for a geometry adaptation. A better location of the control jet has been designed, which decreases the control flow rate.

The present numerical results have been confirmed in an experimental investigation [2]. A yield of both numerical and experimental investigations lies in a better understanding of mechanisms involved in controlled impinging jets, as well as in a further improvement of the particular nozzle geometry.

ACKNOWLEDGEMENT

We gratefully acknowledge the support by the Grant Agency of the Academy of Sciences of the Czech Republic (project No. A2076301) and by the State Committee for Scientific Research, Poland, (project No. Z 19/3/98, ATR BW-8/98).

REFERENCES

[1] Garimella S.V., 2000. Heat transfer and flow fields in confined jet impingement. Annual Review of Heat Transfer XI, 413-494.

[2] Trávníček Z., Peszyński K., Hošek J., Wawrzyniak S., 2003. Aerodynamic and mass transfer characteristics of an annular bistable impinging jet with a fluidic flip-flop control. International Journal of Heat and Mass Transfer 46, Pergamon-Elsevier Science Ltd., 1265-1278.

[3] Kokoshima Y., Shimizu A., Murao T., 1991. Numerical analysis of annular turbulent jet impinging on a flat plate. Proceedings of the 3rd Triennial International Symposium on Fluid Control, Measurement, and Visualization, FLUCOME '91, ASME San Francisco, 205-210.

[4] Maki H., Yabe A., 1989. Unsteady characteristics of the annular impinging jet flow field and reverse stagnation point heat transfer. Proceedings of the National Heat Transfer Conference Heat Transfer in Convective Flows, Vol. 107, Philadelphia, 163-168.

[5] Trávníček Z., Křížek F., 1999. Impinging jet and combined slot nozzle [Impaktströmung und die Zusammengesetzte Schlitzdüse]. Heat and Mass Transfer 35 (5), 351-356 [in German].

[6] Trávníček Z., Maršík F., 2002. Flow visualization and mass transfer with a bistable two-slot impinging jet. Proceedings of the 10th International Symposium of the Flow Visualization, Kyoto.

[7] Tesař V., 2001. Topology changes in an annular impinging jet flow. Proceedings of the Topical Problems in Fluid Mechanics 2001, Institute of Thermomechanics CAS, Prague, 121-124.

[8] Viets H., 1975. Flip-Flop Jet Nozzle. AIAA Journal 13 (10), 1375-1379.

[9] Tesař V., 1997. Řízená tryska pro generaci impaktního proudění. Sborník semináře – Aktuální problémy mechaniky tekutin '97, Institute of Thermomechanics CAS, Prague, 59-60.

[10] Peszyński K., 1998. Flow control by axisymmetric fluidic device with radial switching. Engineering Mechanics '98, Czech Academy of Sciences, 583-588.

[11] Peszyński K., Hošek J., Kuszyński Z., Trávníček Z., Wawrzyniak S., 2000. Active control of annular bistable jet. Engineering Mechanics '2000, Czech Academy of Sciences, Vol. IV, 149-154.

[12] Peszyński K., Trávníček Z., 2002. Jet flow visualization for an axi-symmetric nozzle. [In:] Sempruch J. (ed.), Development in Control and Machinery Design. Wyd. Uczeln. ATR w Bydgoszczy, 55-64.

[13] FLUENT User's Guide, Release 5.5.14, 1998. FLUENT Inc. Lebanon.

[14] Patankar S.V., 1980. Numerical Heat Transfer and Fluid Flow. Hemisphere, Washington D.C.

Kazimierz Peszyński

University of Technology and Agriculture
Department of Control and Machinery Design
Prof. S. Kaliskiego 7, 85-796 Bydgoszcz, Poland

Zdeněk Trávníček

Institute of Thermomechanics
Academy of Sciences of the Czech Republic
Dolejškova 5, 182 00 Prague 8, Czech Republic

MASS TRANSFER MEASUREMENTS OF A FLIP-FLOP JET USING THE NAPHTHALENE SUBLIMATION TECHNIQUE

Summary: The naphthalene sublimation method can be used to study heat/mass transfer for a variety of applications. The heat transfer coefficient, which is often desired, can be readily obtained from the measured mass transfer results using heat/mass transfer analogy. The naphthalene sublimation method can be particularly useful in complex flows and geometries, and can be applied widely and conveniently. However, there are several limitations to this method, such as low-velocity and high velocity limitations. In the former case the run time needed can be too long, in the later case an aerodynamic heating (recovery effect) can cause a non-uniformity of the thermal boundary conditions. The naphthalene sublimation method has been used for a study of impinging jets, when a jet flow control was applied to enhance heat/mass transfer onto exposed walls. An axi-symmetric jet from an "intelligent nozzle" (namely annular nozzle equipped by an active fluidic control) has been used to generate a bistable annular impinging jet. Local mass transfer has been obtained, and the relationships between jet flow stage and heat/mass transfer have been discussed.

Keywords: annular nozzle, heat transfer, mass transfer, impinging jet

1. INTRODUCTION

An experimental approach to many heat transfer problems requires a quantification of heat flux (heat transfer per unit area) onto body surfaces. Typically, wall temperature is measured (as a basic information at almost each of experimental methods), and heat flux is evaluated by means of a concept of the convective heat transfer coefficient [1]. One of the alternative experimental methods is based on heat/mass transfer analogy: Firstly, mass transfer experiments are performed and the mass transfer coefficient is evaluated [2]. Secondly, heat/mass transfer analogy is taken into account and mass transfer data are converted into a heat transfer prediction (material properties of working fluid have to be known for this conversion).

A history of experimental investigation of mass transfer by means of sublimation from a solid body dates back to the late thirties and forties [2]. However, a bit wider practical application of this method began much later, within the sixties, [3, 4]. A sublimating material has been (almost always) naphthalene, [5, 6]. The wall, which is made out of this material, is located into an investigated flow field. Working fluid is

the air, and the thermal boundary conditions are approximately isothermal (i.e., temperatures of naphthalene wall, air, and laboratory are approximately the same).

Impinging jets (fluid jets impinging normally onto a body surface) may be used to achieve enhanced convection heat transfer [7]. The impinging jets are used in variety of industrial applications such as cooling (highly heat-dissipated electronic components, turbine blades, rotating disks), heating (including annealing and tempering of glass and sheet metal), and drying (paper, textile, veneer), see literature referring to this topic [8-14, 29]. Three typical advantages of impinging jet applications are (1) high intensity of heat/mass transfer, (2) good adaptability to a different surface shape with good localization of heat/mass transfer surface area, and (3) relatively simple and cost-effective applications. An investigation of impinging jets (logically) has started with basic configurations of round and slot nozzles [4, 8, 15]. Further enhancement of heat/mass transfer process is typically jointed with a (passive or active) flow control. The former method, *a passive control of flow field*, is based on a geometry modification, namely on intentional nozzle shaping – [16-20]. The latter method, *an active control of flow field*, lies in an interaction of the main flow with the control flow [21].

The present paper deals with naphthalene mass transfer experiments, and an axisymmetric impinging jet is studied. An annular nozzle is equipped with an active flow control, namely with a flip-flop jet switching controlled by fluidic principles. The nozzle has been designed recently [22], and it has been gradually developed up to the present time [23-26, 29]. It seems to be a very promising variant for a desirable augmentation of convective heat/mass transfer.

2. NAPHTHALENE SUBLIMATION METHOD

Principle of method. Driving force of mass flow of vapor sublimated from a naphthalene surface and carried away to the surrounding air is their concentration gradient $\frac{p_N}{r_n T}$, where p_N is the partial pressure of naphthalene vapor, r_N is the gas constant of naphthalene , and T is temperature.

Mass flux of naphthalene vapor can be quantified by means of the concept of a mass transfer coefficient $\beta\,[\mathrm{m\cdot s^{-1}}]$, referring to difference of component concentration:

$$n_N = \beta\left(\frac{p_N''}{r_N \cdot T_W} - \frac{p_{Ne}}{r_N \cdot T_e}\right) \quad [\mathrm{kg\cdot m^{-2}\cdot s^{-1}}] \tag{1}$$

Quantities which are presented in this equation will be discussed in the next part of this text, at step A.

Modeling. Naphthalene sublimation method is based on modelling, performed in some steps:

A. As model is used measured quantity in which sublimation of naphthalene vapor occurs. Near surface (index W at equation (1)) partial pressure of naphthalene vapor p_N'' and wall temperature T_W is assumed. The analysis concerns the case where in the supplied air there is no naphthalene vapor $(p_{Ne} = 0)$, then the second element in parentheses of equation (1) is zero.

B. Measurement of the mass transfer coefficient $\beta(x)$. Considering steady (in mean-flow sense) process, quantity of mass flow of sublimated vapor density is determined by weighing or by measuring the loss of thickness of naphthalene specimen:

$$n_N = \frac{dm}{dS \cdot \Delta\tau} \text{ or } n_N = \frac{\rho_N \cdot \Delta h(x)}{\Delta\tau} \left[\text{kg} \cdot \text{m}^{-2} \cdot \text{s}^{-1}\right] \qquad (2a, 2b)$$

where dm is naphthalene mass which was sublimated from the surface with an active element dS, $\Delta\tau$ is duration of location of the naphthalene plate at measurement space (so-called 'exposition time'), ρ_N is the density of solid naphthalene, $\Delta h(x)$ is net local sublimation depth.

If density of the mass flow n_N is determined on the basis of Δm sublimated naphthalene mass, the result is average value of transfer mass coefficient at the surface ΔS; if the n_N is determined from sublimation depth, the real local value is obtained:

$$\left[\overline{\beta}(x)\right]_{\Delta S} = \frac{r_N \cdot T_W \cdot \Delta m}{p''_N \cdot \Delta S \cdot \Delta\tau} \text{ respectively } \beta(x) = \frac{\rho_N \cdot r_N \cdot T_W \cdot \Delta h(x)}{p''_N \cdot \Delta\tau} \qquad (3a, 3b)$$

The individual quantities which occur in this equation will be discussed in the following part of this text. Introduced by the equation (3b) transfer mass coefficient β should be understood as local, while its average value β_R (average referred to surface on which mass transfer occurs) is often used. For an axisymmetric case analysed, for the circle with radius R equation (3) can be expressed as:

$$\beta_R = \frac{2}{R^2} \int_0^R \beta(r) \cdot r \cdot dr \qquad (4)$$

C. For non-dimensional description of mass transfer, the Sherwood number is used, its local and average values are defined in the following way: $Sh_D = \frac{\beta(r) \cdot D}{D_c}$, $Sh_{DR} = \frac{\beta_R \cdot D}{D_c}$. The first relation is Sherwood number calculated from local values of the mass transfer coefficient, the second from its average value. In both cases, as characteristic dimension, the outer diameter of annular nozzle outlet D was chosen, and in the denominator the mass diffusion coefficient of naphthalene vapor to air $D_c \left[\text{m}^2 \cdot \text{s}^{-1}\right]$ is placed. Similarity of physical properties of the flowing medium is described by Schmidt number $Sc = \frac{\nu}{D_c}$.

D. In the next step we can use the *analogy between heat transfer and mass transfer processes*. Convectional heat transfer is described by the "Newton's cooling law": $q = \alpha(T_W - T_e) \left[\text{W} \cdot \text{m}^{-2}\right]$, where $\alpha \left[\text{W} \cdot \text{m}^{-2} \cdot \text{K}^{-1}\right]$ is the heat transfer coefficient, T_W is temperature of the exposed wall, and T_e is temperature of the outer flow, i.e. usually at a nozzle outlet. In case of high velocity of the outer flow an aerodynamic heating of the wall may be considered, and instead of temperature T_W substitute adiabatic wall temperature, determined adiabatically for experiment without heat/mass

transfer (see 'recovery effect'), which is described in the following text in connection with exact determining of naphthalene surface temperature.

In the case analysed it is the so-called partial analogy where Lewis number $Le = \frac{Sc}{Pr} \neq 1$. For our case of both small concentration and small density of mass flow,

$$\frac{Nu}{Re^m \cdot Pr^n} = \frac{Sh}{Re^m \cdot Sc^n} \tag{5}$$

is required.

Substituting $Nu = \frac{\alpha \cdot D}{\lambda}$ and $Sh = \frac{\beta \cdot D}{D_c}$, where λ $\left[W \cdot m^{-1} \cdot K^{-1}\right]$ is the heat conduction, and substituting of the thermal diffusivity: $a = \frac{\lambda}{c_p \cdot \rho}$, where c_p is the specific heat at constant pressure, the following relation is obtained:

$$\frac{\alpha}{\beta} = \frac{a \cdot c_p \cdot \rho \cdot Pr^n}{D_c \cdot Sc^n} \tag{6}$$

Finally, substituting definitions $Pr = \frac{\nu}{a}$ and $Sc = \frac{\nu}{D_c}$, we obtain the following ratio of the heat and mass transfer coefficients:

$$\frac{\alpha}{\beta} = c_p \cdot \rho \cdot \left(\frac{Sc}{Pr}\right)^{1-n} \tag{7}$$

E. Non-dimensional description of heat/mass transfer in a form of correlation equations. Generally accepted forms are following:

$$Sh = f\left(l_1^+, l_2^+, \ldots, l_N^+\right) \cdot Re^m \cdot Sc^n \quad \text{respectively} \quad Nu = f\left(l_1^+, l_2^+, \ldots, l_N^+\right) \cdot Re^m \cdot Pr^n \tag{8}$$

where $l_1^+, l_2^+, \ldots, l_N^+$ are parameters of geometry, alternatively respecting also influence of other boundary conditions.

Partial problems of experimentation which have to be solved:

- manufacturing of naphthalene plate,
- measuring of quantity of sublimated naphthalene,
- evaluation of naphthalene properties,
- analysis of uncertainties and limitations: verification of the results.

Manufacturing of naphthalene plate. There are some known methods of manufacturing the naphthalene specimen. Small naphthalene specimen can be produced by cold pressing using high pressure [8], bigger ones can be produced from molten or dissolved naphthalene [6]. Many different manufacturing processes are used such as painting, submersion, spraying on a metal base or casting naphthalene to metal mold. If metal mold is not used, mostly it is essential to combine manufacturing with following thermal or mechanical equalization of naphthalene such as pressing or mechanical machining. In that case the achievement of the high quality surface and good repeatability of the experiment may be questionable. For this reason the naphthalene

specimen for our experiments, in principle, is manufactured by us by casting molten naphthalene to metal mold.

The sectional steel mold, used in the experiments described in this study, has total dimensions $(130 \times 450 \times 25.5)\,\mathrm{mm}$. The cover of $8.5\,\mathrm{mm}$ thickness, which generate naphthalene surface, is polished to metallic lustre. This surface before casting has to be perfectly devoid of all pollutions, and degreased with perchloroethylene. Casting is performed in a reversed position, where a future naphthalene surface is directed down. Insignificant inclination, which assure good filling of mold by molten naphthalene and venting, is approximately 3° in relation to horizontal orientation.

Naphthalene melting point is $80.2^{\circ}\mathrm{C}$, boiling point is $217.993^{\circ}\mathrm{C}$ [6]. Some minutes before casting it is convenient to exceed the boiling point, in the aftermath of this better homogeneity of naphthalene is achieved after its solidification for lowering its porosity. Casting temperature is usually at least $140^{\circ}\mathrm{C}$. The mold should be heated to $50^{\circ}\mathrm{C}$. After casting the mold is left in laboratory temperature for some hours. In this time both naphthalene solidification and temperature equalization is achieved. After cooling the cover is disassembled (the best by sheared impact). In this way manufacturing of naphthalene specimen is completed. Its thickness is $4.5\,\mathrm{mm}$ and active surface is $(100 \times 420)\,\mathrm{mm}$. Usual deviations from flatness of the whole active surface are less than $0.2\,\mathrm{mm}$, surface quality is equal to quality of the polished cover. All the remaining surfaces are restricted by mold, for good adhesion the mold on these surfaces is chased.

Total mass of the mold including the naphthalene specimen is $12.0\,\mathrm{kg}$, including the part without cover as $7.7\,\mathrm{kg}$. Relatively robust design is important both for achieving high thermal capacity of mold (i.e. for good casting conditions, evenly cooling, and good specimen quality) and for sufficient stiffness (necessary for accurate surface measurement, see the following text).

Measuring quantity of sublimated naphthalene. There are two basic measuring methods: weighing the naphthalene plate and measuring the sublimation depth of the naphthalene plate:

A. Weighing naphthalene

- naphthalene plate is weighed before the experiment,
- plate is placed into the measurement space where the experiment is performed. Regular duration is $\Delta\tau = (15 \div 180)\,min$,
- after the experiment naphthalene plate is weighed again. The difference between before and after the experiment is naphthalene sublimated mass Δm, see equation (3a).

If the naphthalene palate is manufactured as one piece, it is possible to determine only an average value $\overline{\beta}$ following equation (3a). This inconvenience may be removed by manufacturing the naphthalene plate from rectangular prisms, see [4, 5]:

- individual naphthalene prisms are weighted before experiment run,
- the naphthalene plate is carefully put together, with special care of surface levelling and preventing all of them from damaging,
- naphthalene plate is placed into the measurement space, where it is exposed,
- the plate is then taken to pieces to be weighted one by one. The mass difference before the exposition and after it is the mass of sublimated naphthalene Δm, see

equation (3a). It should be mentioned that manipulation of rectangular prisms must be carried out very carefully. A potential damage (for example breaking off the corner) can significantly influence the calculation of the mass transfer coefficient from the equation (3a), since it is interpreted as an addition to the sublimated naphthalene mass.

B. The measurement of sublimation depth of naphthalene. This method is used in the present study.

- Naphthalene plate is placed on the measuring table (SOMET, Teplice, CR). The position sensors LVDT (Linear variation differential transformer, TOMES, Krupka, CR) measure the profile of the naphthalene surface. The continual displacement at the velocity 1 mm/s is carried out simultaneously with 8 sensors, placed evenly side by side 10 mm away from each other. Measured values are digitised (hw National Instruments, DAQ-board AT-MIO-16E-10, sw Labview 3.1.1) and entered to computer memory. Typical step of the displacement is $0.1\,\mathrm{mm}$, the average value of the 10 measures is registered for each sensor.
- The plate is displaced out of measurement space where it was exposed. Typical exposition time is $\Delta\tau = (20 \div 60)\mathrm{min}$. Maximum thickness of sublimated layer should range from $0.05\,\mathrm{mm}$ to $0.1\mathrm{mm}$.
- The plate is again placed on the measuring table where the profile of the surface is measured for the second time. The absolute value of the difference of the profile before exposition and after it is a thickness of the sublimated layer Δh. The course of this thickness along the displaced coordinate $\Delta h(x)$ is than worked out according to equation (3b).

The material properties of naphthalene, see, for example [6]: Naphthalene is an aromatic hydrocarbon, its chemical formula is $C_{10}H_8$, and the molecular weight is $M_N = 128.17\ \mathrm{kg \cdot kmol^{-1}}$. Density of naphthalene (at temperature $20°C$) is $\rho_N = 1175.0\,\mathrm{kg \cdot m^{-3}}$, and the gas constant is $r_N = 64.87\,\mathrm{J \cdot kg^{-1} \cdot K^{-1}}$ (the r_N is the ratio of the universal gas constant, $R = 8.3143\,\mathrm{kJ \cdot kmol^{-1} \cdot K^{-1}}$, and the M_N).

Pressure of the naphthalene saturated vapor p''_N

$$\log p''_N = \frac{1}{T_W}\left[\frac{a_0}{2} + a_1 x + a_2(2x^2 - 1) + a_3(4x^3 - 3x)\right] \tag{9}$$

where $x = \dfrac{(2T_W - 574)}{114}$, $a_0 = 301.6247$, $a_1 = 791.4937$, $a_2 = -8.2536$, $a_3 = 0.4043$.

Mass diffusion coefficient for naphthalene vapor in the air depends on temperature and pressure

$$D_C = 0{,}0681\left(\frac{T_{BU}}{298{,}16}\right)^{1.93}\left(\frac{1{,}013 \cdot 10^5}{p_B}\right)10^{-4} \quad \left[\mathrm{m^2 \cdot s^{-1}}\right] \tag{10}$$

Schmidt number:

$$\mathrm{Sc} = 2.28\left(\frac{T_{BU}}{298.16}\right)^{0.1526} \tag{11}$$

Temperature usually ranges $T_{BU} = (22 \div 28)°\mathrm{C}$, and the Sc – value is typically around 2.28.

Verification the method, its accuracy and limitations. Natural sublimation of naphthalene during the experiment occurs continuously, i.e. during the measurement and during any other activities. This influence should be corrected according to the experimental evaluation. The correction during the experiments is $0.00023\ \mathrm{m \cdot s^{-1}}$. The final value of β is calculated from equation (3b) and than reduced by above mentioned correction.

Temperature of the naphthalene surface T_w (namely, the air temperature of the boundary layer near the surface) is not usually measured directly. To calculate the equation (3) we use temperature measured in the working chamber of the device, corrected in respect to temperature influence near the naphthalene surface. In usual conditions the temperature of naphthalene surface is approximately $0.25\,\mathrm{K}$ lower than the temperature in working chamber of the device.

Jet impingement on the wall, results in the aerodynamic heating: static temperature of the jet, T, increases up to the so called, recovery temperature, T_{REC}. The T_{REC} – is a bit higher than static temperature of the jet T, but lower than total temperature:

$$T_{REC} = T + \frac{r_f \cdot w^2}{2 \cdot c_p}, \tag{12}$$

where the c_p is approximately $1006\,\mathrm{J \cdot kg^{-1}K^{-1}}$. The recovery factor r_f for example, for laminar boundary layer on the longitudinal flow around wall is $r_f = \mathrm{Pr}^{0.5} = 0.84$ for $298.16\,\mathrm{K}$, see [6].

As we measure total temperature T_{BU} with very good approximation in the working chamber upstream the nozzle, we compute T_{REC} as:

$$T_{REC} = T_{BU} - \Delta T_{REC} \tag{13}$$

where:

$$\Delta T_{REC} = \frac{(1 - r_f) \cdot w^2}{2 \cdot c_p} \tag{14}$$

The value of density of the mass vapor flow is determined by the definitional dependence for mass transfer coefficient (1). In the supplied air no naphthalene vapor is found; hence:

$$n_N = \beta\left(\frac{p''_N}{r_N \cdot T_W}\right) \quad \left[\mathrm{kg \cdot m^2 \cdot s^{-1}}\right] \tag{15}$$

Heat balance near the naphthalene surface shows that all the heat needed for its sublimation is supplied by the convection from the surrounding air:

$$n_N \cdot l_{subl} = \alpha(T_{REC} - T_W)\left[\mathrm{W \cdot m^{-2}}\right] \tag{16}$$

The l_{subl} is the specific latent heat of naphthalene sublimation, which was evaluated as the $l_{subl} = \frac{i_{subl}}{M_N}$, where the i_{subl} is the enthalpy of naphthalene sublimation (the i_{subl} was taken from [6] as $i_{subl} = 70360\ \mathrm{kJ \cdot kmol^{-1}}$, thus the $l_{subl} = 549\ \mathrm{kJ \cdot kg^{-1}}$).

From both the latter equations the mass flux of naphthalene vapor can be eliminated.

$$\beta\left(\frac{p''_N}{r_N \cdot T_W}\right) = \alpha\,\frac{(T_{REC} - T_W)}{l_{subl}} \tag{17}$$

Then these may be substituted the above derived coefficients ratio $\frac{\alpha}{\beta}$, resulting from analogy, derived in equation (7):

$$\beta\left(\frac{p''_N}{r_N \cdot T_W}\right) = \beta \cdot c_p \cdot \rho\left(\frac{\mathrm{Sc}}{\mathrm{Pr}}\right)^{1/n}\frac{(T_{REC} - T_W)}{l_{sub}} \tag{18}$$

Air density is substituted from the state equation $\rho = \frac{p_,}{r_{air} \cdot T} = \frac{p_, \cdot M_{air}}{R \cdot T}$.

The gas constant of the air is defined as a ratio of the universal gas constant and the molecular weight of the air, $r_{air} = \frac{R}{M_{air}}$ (where the M_{air} was taken $28.964\ \mathrm{kg \cdot kmol^{-1}}$); similarly for naphthalene: $r_N = \frac{R}{M_N}$. After substituting and rearranging, we obtain

$$T_{REC} - T_W = \left(\frac{l_{subl}}{c_p}\right)\left(\frac{M_N}{M_{air}}\right)\left(\frac{T_,}{T_W}\right)\left(\frac{\mathrm{Pr}}{\mathrm{Sc}}\right)^{1/n}\left(\frac{p''_N}{p_,}\right) \tag{19}$$

Let us denote first four parenthesis as the value K, which can be computed as constant. The temperatures relation $\frac{T_,}{T_W}$ can be approximated as the value 1, and we have:

$$K = \left(\frac{l_{subl}}{c_p}\right)\left(\frac{M_N}{M_{air}}\right)\left(\frac{\mathrm{Pr}}{\mathrm{Sc}}\right)^{1/n}\ [\mathrm{K}] \tag{20}$$

The temperature drop of the sublimating surface in the air surrounding can be expressed as:

$$\Delta T_{subl} = T_{REC} - T_W = K\,\frac{p''_N}{p_,} \tag{21}$$

Finally, the temperature of the sublimating wall is:

$$T_W = T_{BU} - \Delta T_{REC} - \Delta T_{subl} \tag{22}$$

The accuracy of the computed value β depends on the accuracy of the individual measurements, which determine the quantities occurring in equation (3b): the sublimation depth difference, pressure, temperature, and exposition time. For example the accuracy of the position sensors LVDT was estimated by calibration using a set of the gauge blocks (SOMET, CR) and standard deviation was not higher than $0.002\,mm$. The results are significantly dependent on the accuracy of the relations approximating the naphthalene material properties, first of all its saturated vapor (9). The uncertainty of β value has been evaluated by usual methods [27] as $\pm 0.003\,m \cdot s^{-1}$ (i.e. standard deviation of β): it corresponds to the relative value approximately $\pm 3\%$ in the stagnation point of the jet; hence, the uncertainty of β value within $\pm 6\%$ (in the stagnation point) based on a 95% confidence level (doubled value of the standard deviation).

The method of the naphthalene sublimation is used for experimental determination of the averaged in time local values of the mass transfer coefficient β; typical experiment duration ranges from $20\,min.$ to $60\,min.$ This main limitation of the method may be treated sometimes as an advantage, as the result is averaged in sufficient time directly after the experiment (naphthalene specimen), than it cannot be under the influence of the readout method, signal sampling and data processing.

The method is used for flows with little temperature differences, with the almost isothermal heat boundary conditions, see above: analysis of temperature T_W. The jet velocity for which this method is usually used is approximately $30\,m \cdot s^{-1}$, the usage for very little velocity is questionable since it requires a long exposition time (even a few hours at jet velocities of $1\,m \cdot s^{-1}$. At higher velocities, a local surface temperature differences would appear as a result of the "recovery" effect. Higher temperature differences could cause an additional error. For example, the temperature difference of $0.1K$ results in about 1% error of the naphthalene saturated vapor. Moreover, a mechanical erosion effect can appear at higher velocities. Because of that, using this method for naphthalene sublimation during mass transfer for circular impinging jets system showed in [28] is comparatively unusual since jets velocity reaches even $140\,m \cdot s^{-1}$(!).

A reliability of the method, and a validity of the results obtained were being tested in the past. The results have been compared with another experimental data (based on different principles such as fluid evaporation from porous wall or heat transfer measurement). The comparisons are satisfactory, and they fully confirm a usability of the naphthalene sublimation method for precise measurement of transport processes [8, 15].

3. ANNULAR IMPINGING JET WITH AN ACTIVE CONTROL

An annular nozzle equipped with fluidic switching was designed recently [22], its present variant of geometrical shape is a result of experimental research of

axisymmetric velocity field, partially supported with computer simulations [23-26]. The nozzle during the experiment is situated horizontally, its diagram with designation of both possible states of output jet is shown in Figs. 1a and b.

Main nozzle is annular with diameters of 74mm and 84mm, counteraction of output pipe cross-section in the ratio to supply pipe cross-section is 1.41. The air is supplied from centrifugal ventilator whose efficiency is regulated with frequency converter. Terminal is made using flexible metal pipe of inner section 83mm, its end before the nozzle is a horizontal pipe of 47.2 mm inner cross-section and length of approximately 90 cm, inside which the measuring orifice is installed. Average air flow velocity is determined by measurement of the flow with measuring orifice, maximum velocity with Prandtl probe of a diameter 2mm.

Control nozzle is shaped in radial slot of width 0.5mm and it is placed near the inner edge of the main nozzle. It is supplied with compressed air from laboratory system, flow rate control is executed by pressure adjustment. Attachment of the control nozzle is made of flexible polyethylene pipe of inner section approximately 8mm. Detailed draft of the newest geometric system shown in dissertation [25].

Drawings 1a and 1b show both states of the jet:

- Fig. 1a shows state 1 without control flow. Annular jet flowing out of the main nozzle as a result of the Coanda Effect adheres to inner cone, moves along the cone and a final flow out is concentrated along the axis of the nozzle. As usual the inner mixing area is placed behind the nozzle core, and outer mixing area is placed on its outer diameter. The border between inner and outer mixing areas is a position of local maximum velocity (in drawing 1a assigned by dashed line), existence of both areas ends at the reattachment point, at which this border crosses axis of the nozzle. Further along the jet the velocity profile has one maximum located on the axis of the nozzle.
- Fig. 1b shows a state of the jet, marked with digit 2, after switching on the control flow. Annular jet flowing out of the main nozzle is strut by radial control flow in the direction of outer cone, as a result of the Coanda Effect it adheres to this surface and flows along it. Resulting flow has a divergent shape - direction of the flow converges with extension of the outer cone surface.

The nozzle is equipped with a spoiler, which is schematically assigned both on Figs. 1a and 1b. The spoiler is made out of the aluminium sheet of thickness 0.35mm and it is shaped in cut cone surface, parallel to inner cone of the nozzle. The length of its chord is 5mm. The spoiler is glued to the outer surface of the nozzle with 8 grips of the same sheet, each grip is 5mm wide and 9mm long. The task of the spoiler is hysteresis-removing, causing an immediate switch of the jet from state 2 to state 1 after switching off the control flow [25].

An annular impinging jet with active control was formed as a result of placing a plate perpendicularly to the axis of the nozzle in a way shown in drawings 1a and 1b. Visualisation of the jet, described in dissertation [25], was performed with 400mm×450mm plywood plate. Experiments connected with mass transfer used to be performed for a wall of outer dimensions corresponding to those of the steel mold in which the naphthalene plate was made.

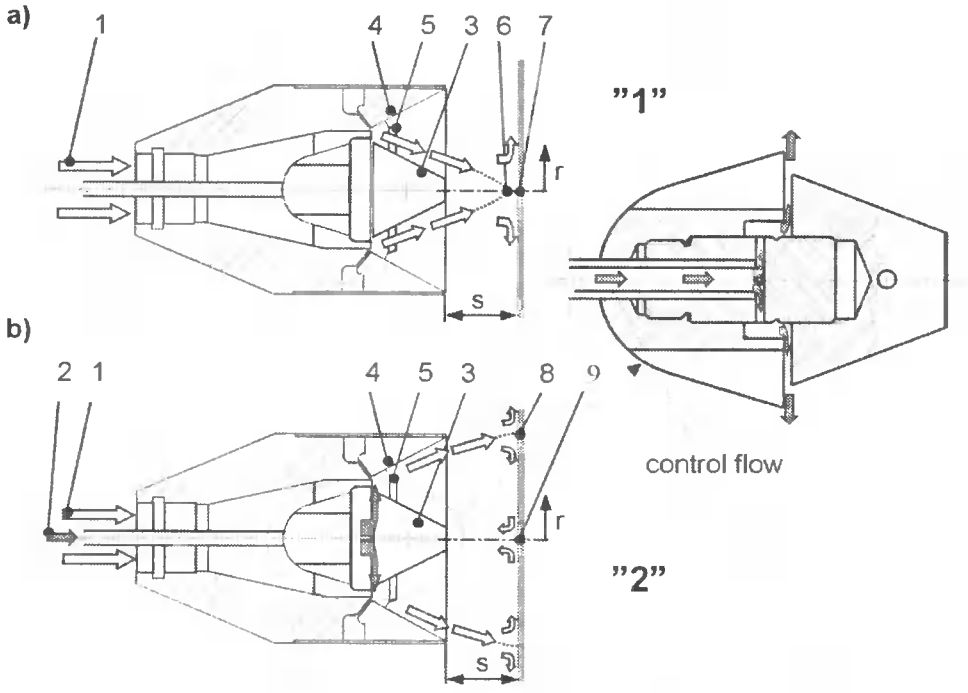

Fig. 1. Annular impinging jet with an active control. (a) State 1 (control jet off), when the jet is focused along a central nozzle body; (b) State 2 (control jet on), output flow has a divergent character. 1 – main flow supply, 2 – control flow supply, 3 – inner nozzle cone, 4 – outer nozzle cone, 5 – spoiler, 6 – reattachment point, 7 – stagnation point, 8 – stagnation circle, 9 – reverse stagnation point

The mass transfer measurement was performed at the nozzle–to–wall distance $s = 80\,\mathrm{mm}$. Reynolds number calculated based on the maximum velocity in the cross-section of the flow-out was $\mathrm{Re}_D = \frac{v_0 \cdot D}{\nu} = 56900$, $\mathrm{Re}_D = 53600$ in state 2 (velocities $v_0 = 10.9\,\mathrm{m \cdot s^{-1}}$, $v_0 = 10.3\,\mathrm{m \cdot s^{-1}}$). Jet contraction coefficient was measured in state 1 and it amounted to $\varepsilon = \frac{V_{AV}}{V_0} = 1.08$ (i.e. ratio of mean jet velocity at the nozzle mouth and maximum velocity in the same cross-section). Control flow, switching the main flow to state 2, accounted for 6% of the flow through the main nozzle.

Typical examples of measured courses of local mass transfer coefficient are shown in Fig. 2 for both states of output jet:

– In state 1 for 'sufficient distance' between the wall and the nozzle a character of flowing around the stagnation point similar to impinging jets from traditional circular nozzle may be expected, as well as local maximums on the graph of transportation coefficients courses in stagnation point. Yet 'sufficient distance' would be appropriate for a wall placed as far as behind the reattachment point.

The location of the reattachment point depends on the total configuration i.e. not only on the outflow of the nozzle but also on wall placing. Measured course '1' shows that the wall was not placed behind the reattachment point and the profile of velocity of the jet dropping on the wall must have had a saddle on the axis (local minimum). Therefore a course of transportation coefficients in stagnation point also has a minimum in the stagnation point. In state 1 it reaches relatively high values

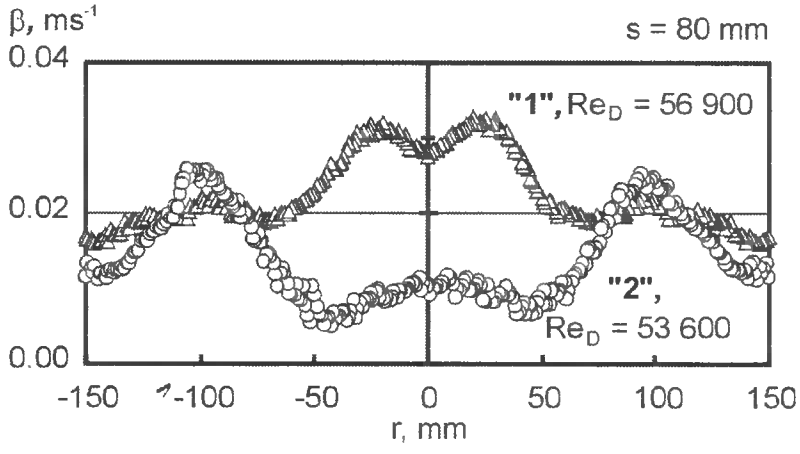

Fig. 2. Behavior of local mass transfer coefficient for both states of flow

– Velocity field in state 2 is designated with 'huge' recirculation area, reaching as far as the wall, on the axis of the nozzle the so-called "reversed" stagnation point is located. Specific stagnation point has transformed in the stagnation circle around this point. Transportation coefficients course corresponds to this character of the flow, since in 'reversed' stagnation point on the axis a vague local maximum is located, and near the stagnation circle – a local maximum of transfer coefficient.

4. CONCLUSIONS

The naphthalene sublimation method can be used for measurement of the local mass transfer coefficient. The mass transfer data obtained can be converted, by means of heat/mass transfer analogy, into the domain of heat transfer, where the convection heat transfer coefficient can be predicted. The naphthalene sublimation method is a typical experimental tool used in many world-leading laboratories to investigate of transport phenomena. It can be expected that the method will be used also in the future. The uncertainty of the local mass transfer coefficient (for the present variant of the method, for an evaluation in the stagnation point) falls within ±6% based on a 95% confidence level (doubled value of the standard deviation).

An active control of flow fields is an essential possibility for desirable enhancement of convection heat/mass transfer. It is already known that flow fields can be effectively controlled by means of fluidic principles. Nozzles, which are designed according to this idea, are frequently called 'intelligent nozzles'. The present paper deals with an annular nozzle equipped with a fluidic flip-flop control. The nozzle is

used for generation of an axisymmetric impinging jet. The results of naphthalene sublimation experiments confirm a proper flip-flop function of the nozzle: the resultant impinging jet is either focused towards the centre spot or spread onto a large area around it. Maximum local heat/mass transfer coefficient is achieved either in the center spot or in the stagnation circle, respectively.

The geometry proposed seems to be a very promising variant for a desirable augmentation of convective processes and a further development is considered meaningful for many applications.

ACKNOWLEDGEMENT

We gratefully acknowledge the support by the Grant Agency of the Academy of Sciences of the Czech Republic (project No. A20760301) and by the State Committee for Scientific Research, Poland, (project No. Z 19/3/98, ATR BW-8/98).

REFERENCES

[1] Doebelin E.O., 1990. Measurement systems application and design. 4th ed., McGraw-Hill New York.

[2] Spalding B.D., 1963. Convective mass transfer. London.

[3] Sogin H.H., 1958. Sublimation from disks to air streams flowing normal to their surfaces. Trans. ASME 80, 61-69.

[4] Korger M., Křížek F., 1966. Mass-transfer coefficient in impingement flow slotted nozzles. International Journal Heat and Mass Transfer 9 (5), 337-344.

[5] Souza Mendes P.R., 1988. The naphthalene sublimation technique. [In:]. Shah R.K., Ganic E.N., Yang K.T. (eds.), Experimental Heat Transfer, Fluid Mechanics, and Thermomechanics, 1st World Conf., Dubrovnik, Elsevier New York.

[6] Goldstein R.J., Cho H.H., 1995. A review of mass transfer measurements using naphthalene sublimation. Experimental Thermal and Fluid Science, 416-434.

[7] Incropera F.P., DeWitt D.P., 1996. Introduction to heat transfer. 3rd ed., J. Wiley & Sons New York.

[8] Dyban E.P., Mazur A.I., 1982. Konvektivnyj teploobmen pri strujnom obtekanii tel. Naukova dumka, Kiev [in Russian].

[9] Downs S.J., James E.H., 1987. Jet impingement heat transfer – a literature survey. National heat transfer conference, Pittsburgh, Pennsylvania, 87-HT-35.

[10] Jambunathan K., Lai E., Moss M.A., Button B.L., 1992. A review of heat transfer data for single circular jet impingement. International Journal Heat and Fluid Flow, 106-115.

[11] Viskanta R., 1993. Heat transfer to impinging isothermal gas and flame jets. Experimental Thermal and Fluid Science 6, 111-134.

[12] Polat. S., 1993. Heat and mass transfer in impinging drying. Drying Technology 11 (6), 1147-1176.

[13] Webb B.W., Ma C.F., 1995. Single-phase liquid jet impingement heat transfer. Acad. Press London, Advances in Heat Transfer 26, 105-107.

[14] Garimella S.V., 2000. Heat transfer and flow fields in confined jet impingement, Annual Review of Heat Transfer XI, 413-494.

[15] Martin, H., 1977. Heat and mass transfer between impinging gas jets and solid surfaces. Advances in Heat Transfer 13, 1-60.
[16] Popiel, C.O., Boguslawski L., 1986. Mass or heat transfer in impinging single, round jets emitted by a bell-shaped nozzle and sharp-ended orifice. Proc. 8th International Heat Transfer Conf., Vol. 3, San Francisco, USA, 1187-1192.
[17] Křížek F., 1990. The wall mass transfer under annular jet impact flow. Part I. Coating 23 (3), 74-77. Part II. Coating 23 (4), 128-132.
[18] Trávníček Z., Křížek F., 1994. Intenzifikace přenosu hmoty na stěně užitím impaktních proudů s cirkulační oblastí. Kolokvium Dynamika tekutin '94, ÚT AV ČR, Praha, 49-50 [in Czech].
[19] Colucci D.W., Viskanta R., 1996. Effect of nozzle geometry on local convective heat transfer to a confined impinging air jet. Exp. Thermal and Fluid Science 13, 71-80.
[20] Huber A.M., Viskanta R., 1994. Impingement heat transfer with a single rosette nozzle. Experimental Thermal and Fluid Science 9, 320-329.
[21] Trávníček Z., 1996. Aktivní řízeni impaktních proudů u složených štěrbinových trysek. Engineering Mechanics '96, Czech Academy of Sciences, 99-102 [in Czech].
[22] Peszyński K., 1998. Flow control by axisymmetric fluidic device with radial switching. Engineering Mechanics '98, Czech Academy of Sciences, 583-588.
[23] Peszyński K., Kamiński A., 1999. Modelowanie numeryczne strumieniowej dyszy pierścieniowej, IX Międzynarodowa Konf. Nauk. Tech. IX ICMR '99, Bydgoszcz [in Polish].
[24] Peszyński K., Hošek J., Kuszyński Z., Trávníček Z. Wawrzyniak S., 2000. Active control of annular bistable jet. Engineering Mechanics '2000, Czech Academy of Sciences, Vol. IV, 149-154.
[25] Peszyński K., Trávníček Z., 2002. Jet flow visualization for an axi-symmetric nozzle. [In:] Sempruch J. (ed.), Development in Control and Machinery Design. Wyd. Uczeln. ATR w Bydgoszczy, 55-64.
[26] Tesař V., Peszyński K., 2001. Computational and anemometric investigations of impinging flows generated by an annular bistable nozzle. XI Międzynarodowa Konf. Nauk. Tech. IX - ICMR '01, Bydgoszcz.
[27] Kline S.J., McClintock F.A., 1953. Describing uncertainty in single-sample experiments. Mechanical Engineering 75, 3-8.
[28] Christ A., Weinmann M., Weinmann A., 1977. Berechnungsgrundlagen zur Konvektionstrocknung von Papier mit Düsenhauben. Escher Wyss Mitteilungen, 11-16.
[29] Trávníček Z., Peszyński K., Hošek J., Wawrzyniak S., 2003. Aerodynamic and mass transfer characteristics of an annular bistable impinging jet with a fluidic flip-flop control. International Journal Heat and Mass Transfer 46 (7), 1265-1278.

Václav Tesař

University of Sheffield
Department of Chemical and Process Engineering
Mappin Street, Sheffield S1 3J, United Kingdom
on leave from CVUT Czech Technical University, Prague, Czech Republic

NEW FLUID FLOW PARAMETER - ITS MEANING AND IMPORTANCE, IN PARTICULAR FOR MICROFLUIDICS

Summary: The paper discusses a dimensionless number recently introduced for characterization of fluid flow conditions – and its practical uses for design and operation of fluidic devices, in particular pressure driven microfluidic valves at low Reynolds number. Originally intended just as a convenient tool for adjustment of conditions, it is found to posses interesting physical meanings and also direct relation to the commonly used characterisation parameters, Reynolds and Euler numbers.

Keywords: fluidics, characterisation parameters, Reynolds number, Euler number.

1. INTRODUCTION

Fluidics is the technology of generating and handling fluid flows [1, 2]. In contrast to classical pumps and valves (which may be termed '*mechanofluidic*' devices, being based on action of their moving mechanical components), the interest has been shifting towards purely fluidic no-moving-part devices [3]. These offer a number of attractive advantages, such as high operating frequency, long life, high reliability, resistance to adverse effects of temperature, fluid aggressivity, etc. They are essentially formed by constant geometry cavities, performing their task by using hydrodynamic phenomena such as the raction of fluid jets, Coanda jet attachment, etc. [4]. What appears to be of increasing importance is currently microfluidics; a part of fluidics using very small size devices [5], also e.g. [6, 7, 8, 9].

To characterize fluid mechanics of the devices, dimensionless parameters are used, the best known being Reynolds number, Re. Its importance is due to fluid flow undergoing a fundamental change, the transition from laminar to turbulent character, at a certain critical value of Re. Another fact, of particular importance for laboratory investigations, is that two flows (e.g. in a pump and in its scaled-down laboratory model) are hydrodynamically similar if Re is the same in both flows.

A new dimensionless number, denoted by provisional symbol Te (in ref. [7]), was recently introduced for a similarly useful flow characterisation in microfluidics. The present paper discusses its meaning and uses.

2. CHARACTERISATION OF DEVICES

The new parameter is particularly useful for design and investigation of ***multi-terminal*** pressure-driven devices. It is, nevertheless, also useful for characterization of devices having only two terminals, Fig. 1. The internal geometry is irrelevant for the present discussion and Fig. 1 shows a '*black box*' representation of what may be

a simple connecting pipe, nozzle, diffuser, or even a quite elaborate circuit, provided it connects with the rest of the system by only two terminals. A perfect description of the fluid flow would involve all the details of the internal flowfield. In fluidic systems, the interest is limited to a description giving the information necessary to build circuits.

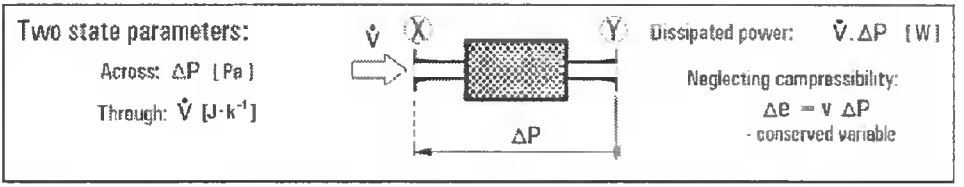

Fig. 1. Schematic representation of a two-terminal fluidic (or micro-fluidic) device. Its state is determined by the two state parameters. Note that only the value of the flow rate at the inlet X is needed, the value in the outlet Y being identical due to mass conservation

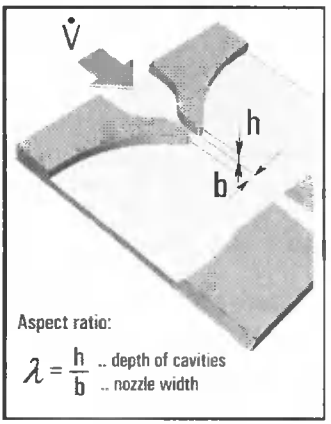

Fig. 2. Typical fluidic devices consist of rectangular cross section cavities having a constant depth. The smallest cross section (and highest velocity) is usually in the jet-generation nozzle

For this purpose, the state of the device is sufficiently specified by only two parameters (analogous to voltage across and current through an element in electric circuits, note that similarly as there, the product should be power in correct unit). Circuits are governed by the two Kirchhoff laws – conservation of the across variable differences in all loops, and conservation of the through variable in all circuit nodes. The two state parameters thus should be quantities for which conservation laws apply. The mass flow rate $\dot{M}$ (in kilograms per second) and the difference of the fluid specific energy Δe (measured in joules per kilogram) between the two terminals would be a perfect choice. The disadvantage is the difficulty associated with evaluation of the specific energy drop from directly measurable quantities, requiring knowledge of details of internal thermodynamic processes. The situation is much more simple if fluid compressibility and thermal effects do not need to be considered, as shown in the bottom part of Fig.1, the specific energy drop is then simply proportional to the directly measured pressure difference ΔP. It is then acceptable to use as the state parameters the volume flow rate $\dot{V}$ (measured in cubic metres passing through the device per second) as the through parameter and the pressure difference ΔP (in pascals) as the across parameter. Although somewhat deficient from theoretical point of view [10], these two state parameters are in common use.

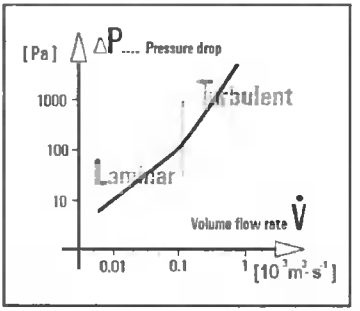

Fig. 3. Typical characteristic of a two-terminal fluidic device. When plotted in logarithmic co-ordinates, both laminar and turbulent part are (nearly) straight lines

The most modern fluidic devices are of planar layout, with constant depth cavities – similar to the nozzle design shown in Fig. 2. They are commonly made by etching or laser cutting. Individual devices differ in their properties, described by the dependences between the state parameters. These dependences are called *constitutive relations* – dependent upon the consitution, internal arrangement of the device. Their graphical representation is called the *characteristic*, the term sometimes applied also to the constitutive relation itself. In steady two-terminal incompressible case it is a single line graph $\Delta P = f(\dot{V})$. The change in the flow character at the critical Reynolds number causes it to split into two different but interconnected parts, laminar and turbulent, Fig. 3. In the logarithmic co-ordinates used there, the slope of the line in the turbulent regime is usually very near to 2.0 (dissipation of kinetic energy of the vortices, which is proportional to square of flow rate due to kinetic energy being proportional to square of velocity). In the laminar regime its slope is usually very near to 1.0 (purely frictional loss without vortex shedding).

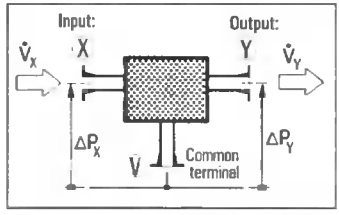

Fig. 4. Schematic representation of a three-terminal device. There are two independent flows (the third one is determined from mass conservation) and also two independently variable pressure differences between the terminals

Much more interesting flow phenomena, due to the effects resulting from mutual interaction of the flows, take place in devices having more than two terminals. Characterising their behaviour is accordingly more complicated. It involves by $n-1$ simultaneous equations specifying the constitutive relations between the $2(n-1)$ independent variables of a n-terminal device. To avoid excessive complexity, the discussion of these multi-terminal devices will be here limited to those having only three terminals, as shown schematically in Fig. 4. Even then graphical presentation of characteristics is not simple, since a diagram can present a relation between at most three variables [13]. Typical solution of this problem is to plot two diagrams: the input characteristic $\Delta P_X = f(\dot{V}_X)$ with a family of lines with $\dot{V}_Y$ as the parameter, and the

output (loading) family of characteristic lines $\Delta P_Y = f(\dot{V}_Y)$ with parameter $\dot{V}_X$ kept constant for each line in the family.

3. CLASSICAL REYNOLDS AND EULER DIMENSIONLESS PARAMETERS

In discussing electric circuits, the component properties are usually characterized by a single characterization quantity, such as e.g. the resistance of a resistor. It would be quite inconvenient if the characterization of a device in fluidics would require instead a full diagram of the characteristic. Moreover, such a diagram is valid only for a particular fluid, assuming its properties (specific volume v [$m^3 \cdot kg^{-1}$], viscosity ν [$m^2 \cdot s^{-2}$], ...) are constant (while they actually vary e.g. with varying temperature). Another fluid or a change in temperature means laborious replotting of the diagrams. This is avoided so that a simple universally valid description by a single numercal value is obtained by using the dimensionless parameters, Reynolds number (Fig. 5) and Euler number (Fig. 6). The fact that many values of Reynolds number may be defined for a single particular device, depending upon the choice of the reference dimension and reference velocity, requires some convention: because of the prevalence of jet-type flow phenomena in classical fluidics, the reference velocity and dimension are usually the values in the supply nozzle, Fig. 2.

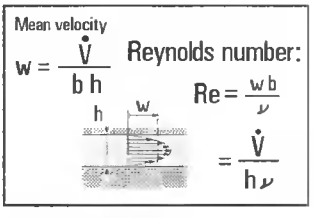

Fig. 5. Reynolds number is usually defined by the conditions in the nozzle exit: velocity w, width b, and fluid viscosity v

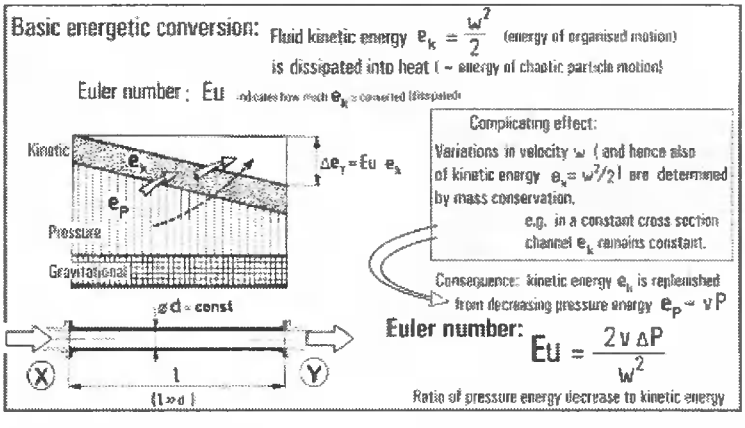

Fig. 6. Another important dimensionless parameter is the Euler number, essentially representing the relative magnitude of dissipation of kinetic energy. Mass conservation constraint (kinetic energy e_k determined by cross sectional areas – it is constant in the case of constant diameter pipe shown at left) causes it to represent a relation between kinetic and pressure energy

The characteristic from Fig. 3 is converted into the dependence shown in Fig. 7 using Re as the nondimensional measure of the flow rate and Eu as a measure of the pressure drop. In large-scale devices, the interest is usually in the turbulent, high-Re part of the diagram. Were the hydraulic losses only due to flow separation, the characteristic there would be a horizontal line. In fact there is usually a small Re-dependent frictional loss component. However (with the exception of extremely long constant-area pipes) Eu of the friction loss is usually small and decreases with increasing Re., so that the characteristics are usually sufficiently near to the single-valued horizontal at high Re. A rough rule is that Eu is practically constant for Re values above $Re = 15 \cdot 10^3$ (constancy limit). Admitting small variations, comparable to the usual accuracy of instruments and measurement errors, the tolerance limit is roughly at $Re = 10 \cdot 10^3$. Above these limits, the invariance of Eu makes it an excellent characterisation parameter for engineering purposes.

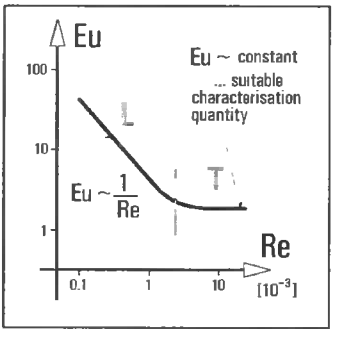

Fig. 7. In the turbulent regime, at large Re, the properties of a large-scale device are fully characterised by a single numerical value Eu, the loss coefficient

4. DEFINITIONS OF THE NEW PARAMETER

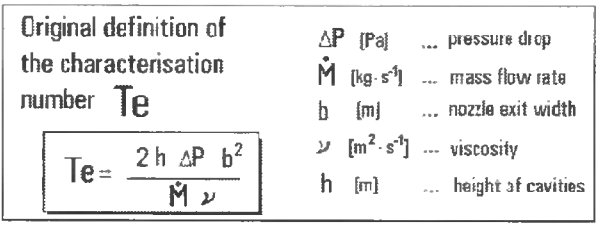

Fig. 8. Original definition of the new characterisation parameter, as it was introduced in ref. [11] for use in adjustment of circuits with micro-fluidic valves. N.B.: The pressure differences in [7] were negative and the expression in [7] and [11] involved absolute value of the pressure difference

The new parameter Te was originally introduced in [11] to non-dimensionalise the measured or computed driving pressure drops. Similarly as in its later use in [7], no considerations were initially given to its further importance. It was used just as a convenient tool for adjusting the conditions in a microfluidic circuit containing pressure assisted [11] – and later pressure driven [7, 9] – valves. The original definition is given in Fig. 8 (with a small change in the figure caption). Both that form as well as the others

discussed here are written for rectangular channel cross sections, as shown in Fig. 2. An alternative version for other cross sections is easy to derive. In Fig. 9, there is a slightly different definition suitable for cases where compressibility may be neglected, so that the specific volume v of the fluid may be considered constant and the volume flow rate $\dot{V}$ is used as the through variable.

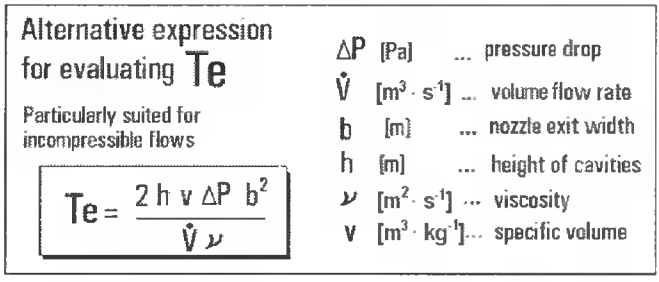

Fig. 9. Another more or less equivalent definition of the newly-introduced parameter Te. This is a definition suitable for working with the incompressible state parameters. $\dot{V}$ and ΔP

The standard way to non-dimensionalise measured or computed pressure values is, of course, to use the Euler number Eu. It relates the pressure difference to dynamic effects, to the dynamic pressure evaluated from the characteristic velocity. In contrast, Te is based upon non-dimensionalisation with respect to viscous effects. It is this feature that makes it particularly useful for microfluidics (Fig. 10) where viscous effects tend to dominate as the scale of the devices decreases, even if fluid viscosity were the same (which is often not the case: microfluidics often handles very viscous fluids such as e.g. biological samples).

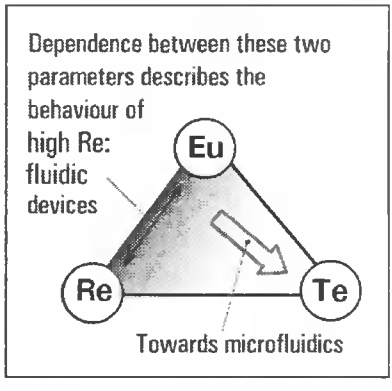

Fig. 10. The dimensionless number Te becomes more important as the small scales, typical for microfluidics, are approached

Dimensionless characterisation numbers Re and Eu may be seen as ratios of various forms of fluid specific energy and the same interpretation may be applied to Te. The expressions for the kinetic and pressure energy in Fig. 11 are standard ones, known e.g. as the corresponding terms in the Bernoulli equation. What is unusual in Fig. 11 is the analogous expression for the specific dissipated energy. The processes, taking place in fluidic devices, may be viewed as mutual conversions between the three forms of energy: (e.g. an acceleration in a nozzle is a conversion of the pressure energy into the kinetic one, partly also irreversibly converted the dissipation form).

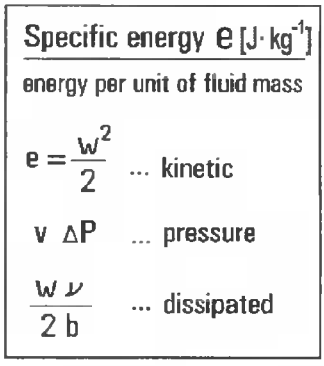

Fig. 11. Expressions for the three forms of specific energy undergoing mutual conversions in fluidic devices. Rather than the pressure energy itself, in present context its drop vΔP is of special interest

Fig. 12 offers another alternative definition of the new parameter, which uses the mean velocity instead of the flow rate – in line with the analogous usage of expressing Reynolds number Re (Fig. 5). According to Fig. 12, the three dimensionless parameters may be visualised as forming a tripartite system: e.g. Euler number on top characterises the ratio between the kinetic energy on the left and the pressure energy on the right. These locations correspond to the three dimensionless numbers at tips of the triangle in Fig. 10.

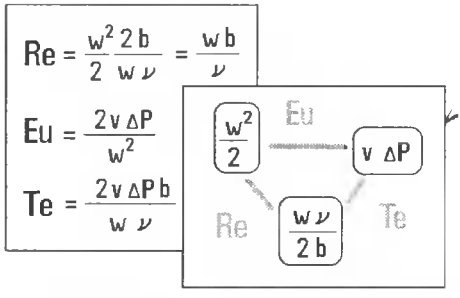

Fig. 12. Three dimensionless numbers, Re, Eu and the new Te represent the mutual ratios of the various forms of energy from Fig. 11

The important fact following from the diagram Fig. 12 is that multiplying mutually Re and Eu, the kinetic energy cancels out:

$$Te = Re \cdot Eu \tag{1}$$

This product of the two well-known dimensionless numbers has been already mentioned in the literature avilable and there has been unsuccessful attempts at namig it. Nogid [14] refers to the product Re.Eu as the Lagrange number, which is, unfortunately, hardly acceptable in the view of the Lagrange number having already a different standard meaning [18]. Čarnogurská [16] mentions the product Re·Eu without giving any details as Günter number while Zierep [15] calls it Stokes number, which is an even less suitable name since there are already enough problems with the Stokes number, the name apart from its well established meaning of the product of Reynolds and Strouhal number in unsteady fluid dynamics being also applied to characterisation of inertial effects in impacting aerosol particles [19].

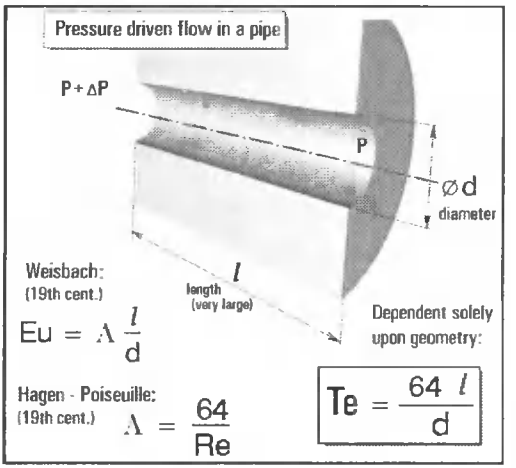

Fig. 13. Fully developed laminar flow in a round, constant diameter channel. This is a classical solution for, leading to invariant numerical value for Te (dependent only upon dimensions: length *l* and diameter *d*)

5. CHARACTERISATION OF LAMINAR REGIME

A philosophical approach suggests that the basic task of scientific investigations is search for invariants. Original studies of using Te in multi-terminal microfluidic valves [7, 9, 11] have led to interesting relationships and it was considered a certain disappointment that for two-terminal devices evaluating Te did not lead to similar relationships – only to a constant value. Yet this constancy is, in fact, a great triumph. The value of Te for laminar flow regime in two-terminal fluidic devices is actually a case of an invariant, sought after by scientific investigations. It provides the highly valuable characterisation of a device by a single numerical value.

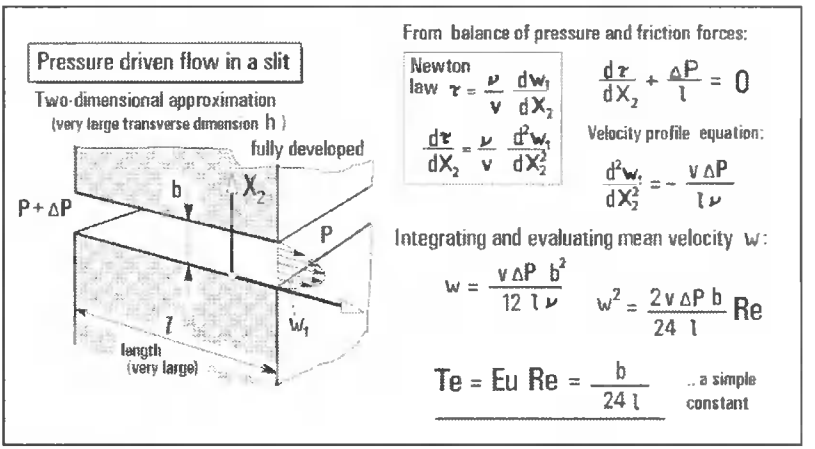

Fig. 14. Laminar flow through a space bounded by two parallel plane walls, which is of special importance for microfluidics. Again, Te is a constant value dependent solely upon the geometry of the cavity

As the simplest example, the classical case of the fully developed laminar flow in a constant-diameter circular pipe, of length l and diameter d, is considered in Fig. 13. The nondimensionalised pressure drop across the length of the pipe is determined by the well-known Weisbach formula, with the friction loss parameter Λ dependence upon Reynolds number given by the Hagen-Poiseuille law. Evaluating the product $Re \cdot Eu$ according eq. (1) leads to the constant value of Te presented at the bottom of Fig. 13. This is the invariant value, independent of the flow rate conditions and fully determined by the dimensions (length and diameter) of the pipe.

A similar result is obtained in Fig. 14 for the rectangular channel of small height h. For simplicity, the derivation there is for a large (theoretically infinite) aspect ratio λ. Also the streamwise length l is assumed to be very large, so that the flow may be considered fully developed. Again, the value of Te is found to be an invariant, dependent only upon the device geometry, but not on the flow rate or on the phenomena inside. The case from Fig. 14 is of particular interest since fluidic and microfluidic devices typically posses constant-depth cavities (as were shown in Fig. 2). Of course, the simplifying assumptions adopted here make the result not directly applicable, though they provide a useful starting point for the more realistic geometries.

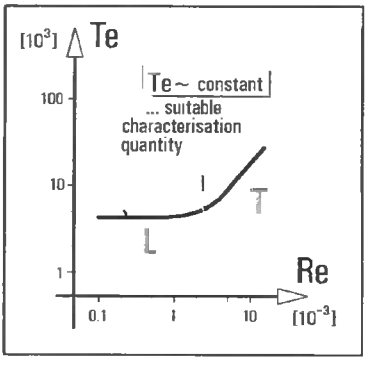

Fig. 15. Parameter Te is the sought after invariant for a laminar flow in a microdevice at small Re (where its meaning and importance matches that of Eu for the analogous characterisation of turbulent flows at large Re, as shown in Fig. 7)

These two cases are particular examples indicating how useful the transformation from the natural co-ordinates is in Fig. 3 into the nondimensional ones shown in Fig. 15 for low Re flows, equally useful as the classical nondimensional transformation from Fig. 3 to Fig. 7 for high Re flows.

6. HYDRAULIC RESISTANCE

The concept of hydraulic resistance is not widely used in fluidics [2]. It is a direct counterpart of the electric resistance (measured in ohms), a quantity of everyday use in electrical engineering, defined by the well-known Ohm's law, the linear dependence between the electric current I and the corresponding voltage drop ΔU. In a perfect analogy, the hydraulic resistance R (measured in somewhat unusual units, $kg \cdot m^{-4} \cdot s^{-1}$) is defined by the linear dependence between volume flow rate $\dot{V}$ and the corresponding pressure drop ΔP, Fig. 16. The main reason for the small popularity and rare use is the fact that in traditional hydraulic engineering, and in large-scale fluidics at high Reynolds

numbers the actual relation between ΔP and $\dot{V}$ is usually far from linear. However, the situation is totally different at the very low Reynolds numbers, prevalent in microfluidics. Even if the flow is laminar, the characteristic may contain a quadratic component due to the vortex shedding, yet the recent progress towards very small devices has already reached the realm of Reynolds numbers so low that hardly any quadratic effects due to vortex shedding take place.

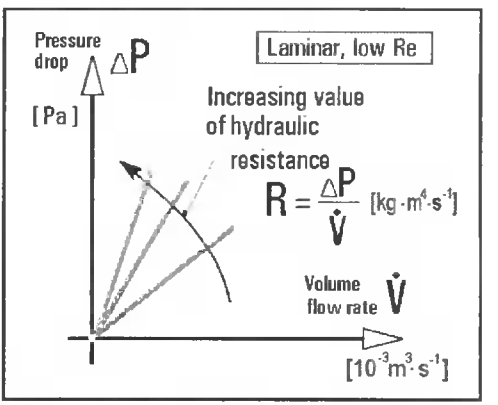

Fig. 16. Hydraulic resistance R as a direct analogy to electric resistance based upon the Ohm's law

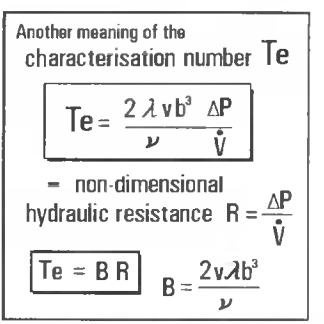

Fig. 17. Alternative physical meaning of the new characterisation parameter Te: it is a dimensionless expression of the hydraulic resistance R from Fig. 16

An inspection of the alternative definition of Te presented in Fig. 17 shows that the expression actually contains the same ratio of pressure drop to the volume flow rate as the definition of R in Fig. 16. Another alternative interpretation of the physical meaning of the newly introduced flow characterising parameter Te is a nondimensional measure of the hydraulic resistance, Fig. 17 and Fig. 18. This is hardly surprising, after all, any alternative characterisation of device properties must be in some way mutually related. To give an idea about the numerical magnitudes of R, R_c, and Te Fig. 19 shows a numerical example of what may be typical values. Note that typical magnitudes of Te are rather high (or, to put it in another way, the characteritic resistance $R_c = 1/B$ tends to be quite small).

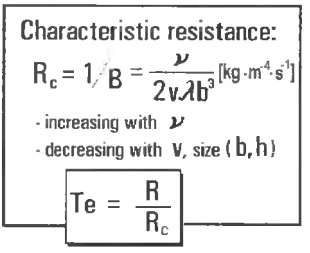

Fig. 18. Coefficient B in Fig. 17 may be interpreted as a characteristic resistance, here for a rectangular b x h cross section channel

7. DIMENSIONLESS DISSIPATED POWER

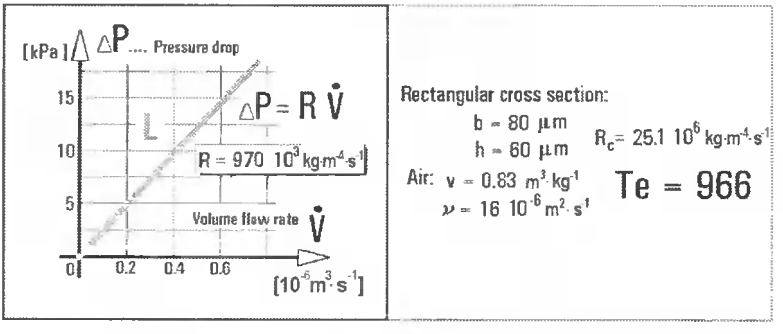

Fig. 19. Numerical example showing typical magnitudes of resistance R and the corresponding Te in a microfluidic device: air issuing from a 80 micrometer wide nozzle

When the steady flow characteristic of a fluidic device, Fig. 3, is represented in the dimensionless form $Eu = f(Re)$, according to Fig. 7, the Reynolds number Re plotted on the horizontal co-ordinate is the nondimensional representation of the magnitude of the flow rate passing through the device, while Euler number Eu on the vertical co-ordinate is the nondimensional expression of the pressure drop. The product of the pressure drop and the flow is the dissipated power (Fig. 1). If the dimensionless characterisation quantities Re and Eu are similarly mutually multiplied, we may expect the product to be a dimensionless representation of the dissipated power. This product, however, was already shown above, in eq.(1), to be Te.

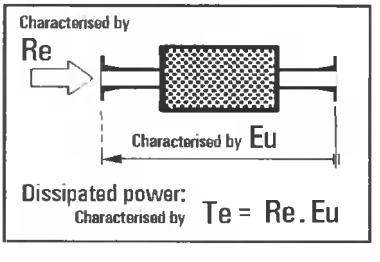

Fig. 20. Characterisation of the state in a two-terminal device by dimensionless parameters. The flow rate magnitude is characterised by Reynolds number Re and the pressure drop across the device by Euler number Eu. The product of the two state parameters, representing the dissipated power (Fig. 1), is characterised by Te

This means, according to Fig. 20, that there is yet another possibility of an alternative physical interpretation of Te. It is also a nondimensional measure of the hydraulic power dissipated inside the device investigated. This may be shown by re-writing in Fig. 21 the definition from Fig. 9. The product $\dot{V} \cdot \Delta P$, the dissipated power from Fig. 1, is shown in Fig. 21 to be present in the rewritten Te, divided there by the expression in the central box of Fig. 22. The dimension of this expression is watt, and therefore may be interpreted as a reference power, using the expression for the specific dissipated energy in Fig. 11. According to this view, Te is a ratio of the power $\dot{V} \cdot \Delta P$ and the reference power in Fig. 19.

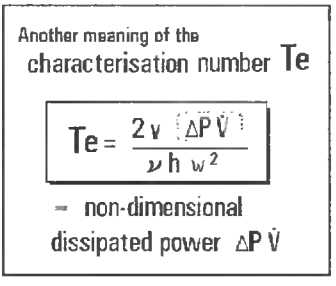

Fig. 21. The definition from Fig. 9 rewritten to show the alternative meaning of Te as a nondimensionalised dissipated power

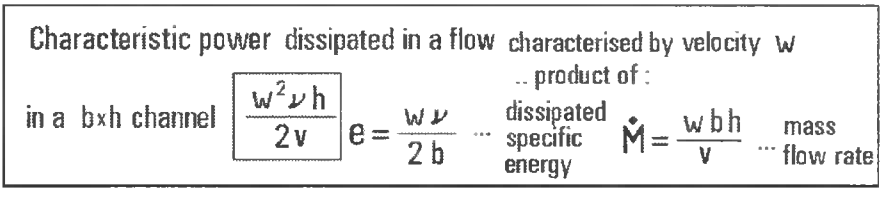

Fig. 22. Proportionality factor between Te and the dissipated power in Fig. 21 is an inverse of the characteristic dissipated power, evaluated using the expression from Fig. 11

There are several uses of this interpretation. Quite obvious is the pedagogical use: elucidating one disadvantage of the traditional dimensionless presentation of device properties by the dependence $\mathrm{Eu} = f(\mathrm{Re})$, as shown in Fig. 7. Turbulent flow, with its effective mechanism of energy dissipation in turbulent eddies, dissipates power more than laminar flow. This, however, is not reflected in the classical representation according to Fig. 7 where turbulent flow seems to be the more advantageous one, possessing a smaller value of the loss coefficient Eu (cf. its interpretation in Fig. 6). Engineering students are taught to minimise power dissipation but they may find the higher loss in turbulent flow not immediately apparent, finding there the lower Eu. However, when the same behaviour is re-plotted into the form corresponding to Fig. 23, the visual impression is completely different: the nondimensional dissipated power Te is seen to be small in laminar regime and increases in turbulent flows with increasing Re.

8. CIRCUITS AND THE MATCHING PROBLEM

A disappointment quite often encountered in fluidics is caused by an improper adjustment of operating conditions and improper matching of individual components in

a circuit. When tested alone, a particular device may operate perfectly – and yet it may fail to perform as expected (or even perform at all) when used with other devices in a system. The new dimensionless number Te is a particularly suitable tool for identifying the adjustment and matching conditions.

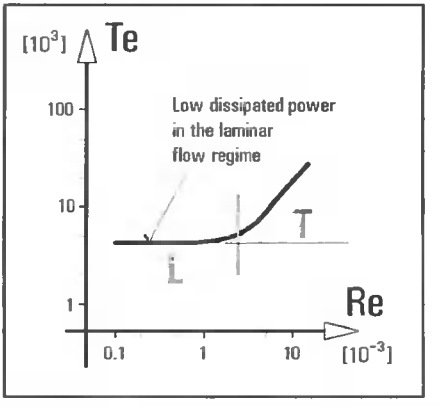

Fig. 23. Pedagogical advantage of the nondimensional presentation of characteristics using Te: it is instructive to see the dissipation to be higher in the turbulent regime

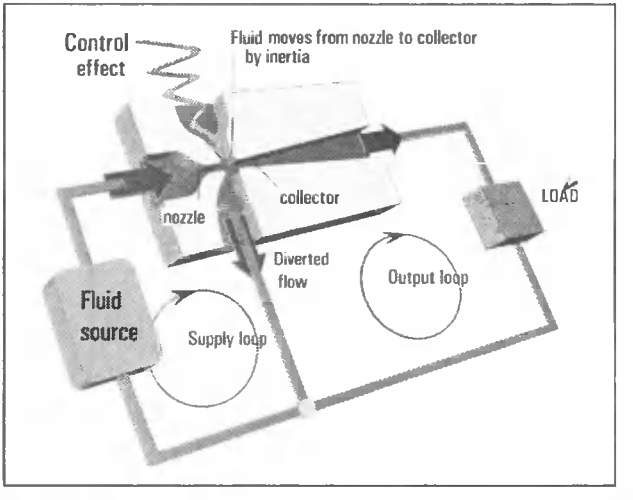

Fig. 24. Typical by-pass type fluid flow control by a fluidic control valve diverting away from the load some fluid supplied by the source

There are, of course, countless circuit types and it is impossible to discuss them all. Nevertheless, the main features of the problem may become apparent from a simplified version of the typical case in Fig. 24. This shows a by-pass, diverting control of fluid flow in a load. To present a more specific picture, we may consider the fluid source being a pump delivering some reactant to a microchemical reactor. For proper operation, the reactor flow rate is to be set and maintained by the fluidic control valve. The reactor resistance may change during the operation, e.g. due to a varying temperature and hence fluid viscosity caused by the heat generated in the chemical reaction. This would call for a re-adjustment by varying the control action – in some feedback loop employing a signal from some sensor monitoring the reactor. This

feedback and the control actions in the four-terminal valve are too complex for the present introductory discussion. Let us, therefore, limit the attention to the simplified version of the problem: the conditions in the output loop, as shown in Fig. 25, and the initial adjustment of the load resistance.

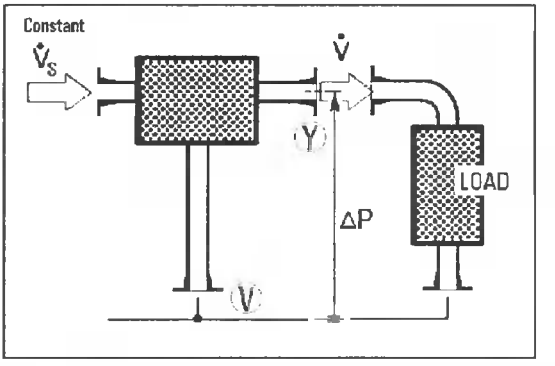

Fig. 25. Schematic ('*black-box*') representation of the loading problem in the output loop of the valve: a variable two-terminal load is connected to a vented three-terminal device supplied with constant supply flow. To simplify the analysis (the actual valve in Fig. 24 has four terminals) the attention is limited to the initial investigation step: evaluating the full output flow (no diverting control action)

This problem of load selection may be simplified thanks to the load-isolating character of the vent, which makes it possible to consider the input variables to be constant. The valve behaviour from the loading point of view (changes in the output loop) is described by the loading characteristic, the dependence of the available output pressure drop ΔP on the output flow rate $\dot{V}$ taken from the device and, of course, passing through the load.

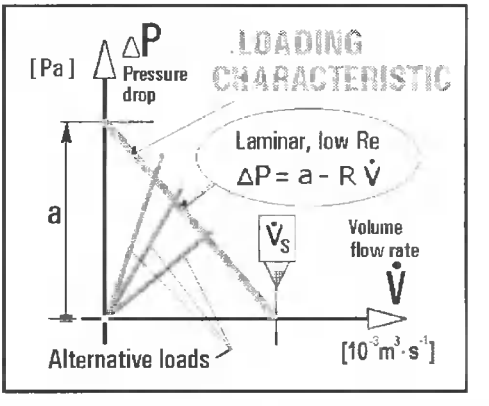

Fig. 26. Output (loading) characteristic of the upstream device (valve) from Fig. 25 is linear for the low-Re conditions in microfluidics. For constant supply flow rate $\dot{V}_S$ (and no control action) the flow $\dot{V}$ through the load is determined by the intersection with load characteristic

Generally, the shape of the output characteristic is a curve sloping down – the output pressure drop ΔP decreases with output flow rate $\dot{V}$. This may be modelled as an

effect of an internal restrictor inside the output (representing all the losses taking place in the upstream device). Fig. 26 shows the linear decrease in a very low Re laminar device.

9. DRIVING PRESSURE FOR HIGH NO-CONTROL OUTPUT FLOW

In Fig. 25, the fluidic diverter valve is shown to employ the typical high Re jet-type mechanism. The supplied fluid is accelerated in the nozzle and this ensures its reaching the collector as long as there is no control action. If Re is decreased to the values typical for microfluidic devices, the dominating viscous friction decelerates the jet and the amount reaching the collector is too small. The valve control then has very little room for any sizable effect, the no-control value is simply too little for something to subtract from it by the diverting action. One possible solution of particular importance for present-day microfluidics [6, 7, 9] is to drive the fluid through the valve output, and through the load as well, by a constant driving pressure difference ΔP applied between the vent V and output terminal Y. This necessitates an addition of a pressure regulator but makes it possible to achieve any desirable no-control initial value of the output flow. A proper choice of the driving pressure to get the suitable one is not easy – the more so it depends upon the magnitude of the supply flow. The decision is made easier by the near-universality of the dependence of the relative output flow μ (this choice of this Greek letter is due to the original definition considering the ratio of *mass* flow rates; here it could be applied to the ratio of volume flow rates because of the underlying assumption of incompressibility) on the parameter Te as shown in Fig. 27. This approach was first discovered in [7], see the practical example in Fig. 28. As Re decreases towards the sub-dynamic regime, the data approach the ideal universal linear dependence:

$$\mu = \text{const} \cdot \text{Te} \tag{2}$$

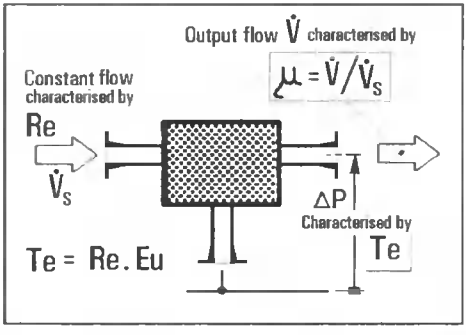

Fig. 27. Nondimensional variables of interest in adjusting the maximum achievable output flow from the upstream three-terminal device. The constant supply flow is characterised by the supply nozzle Re and the driving pressure drop is characterised by Te.

10. OPTIMUM FOR POWER TRANSFER

While getting a large output flow may be a frequent task, there are other fluidic circuits in which it is desirable to transfer into the donwstream load the maximum power – the product of the two state parameters output pressure drop ΔP and output

flow rate $\dot{V}$. Its magnitude varies with the output flow rate $\dot{V}$, being zero in extreme cases, both when there is zero flow rate $\dot{V}$ as well as when the output pressure drop ΔP is zero. Obviously, the transferred power assumes its maximum between these extremes, Fig. 29. The infinite family of possible power characteristics may be usefully converted into a single universal curve using another definition of the new parameter, written here as Te_L (Fig. 30). Note the same constant B as in the expression for the nondimensional hydraulic resistance of two-terminal devices, Fig. 17. The index L is used here to emphasise the important difference: Te for two-terminal devices was dimensionless *dissipated* power. Here it is nondimensional available power at the device output.

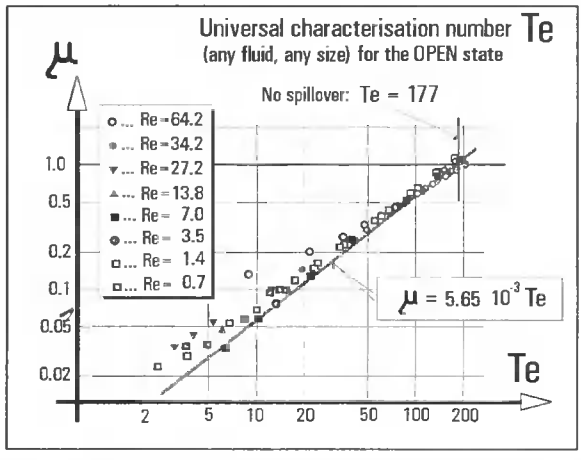

Fig. 28. An example of processing experimental results [7] plotted using the nondimensional variables from Fig. 27. The experiment was made for adjusting the driving pressure of a microvalve to get a high output flow rate in the open state

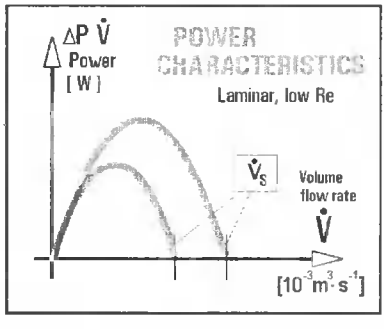

Fig. 29. Variation of the power transferred to the connected downstream load with the output flow rate $\dot{V}$. Two dependences are shown for two different supply flows

The expression for Te_L in Fig. 30 is a general one. It is adapted for a particular device by incorporating its constitutive relation. For the very low Re laminar flow three-terminal devices, the constitutive relation is the liner loading characteristic Fig. 26:

$$\Delta P = a - R_S \cdot \dot{V} \tag{3}$$

– where R is the resistance of the imaginary internal restrictor modeling the downwards sloping of the characteristic. One of the two constants in this expression may be removed by noting that for the maximum flow $\dot{V} = \dot{V}_S$ in Fig. 26 there is $\Delta P = 0$ so that from eq. (3):

$$a = R_S \cdot \dot{V} \tag{4}$$

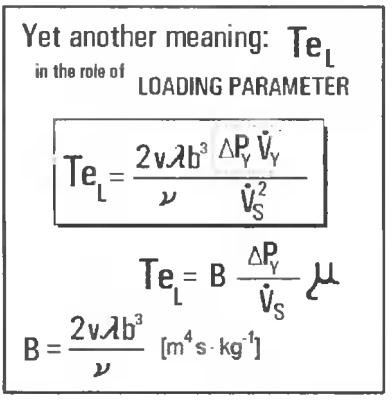

Fig. 30. Newly introduced dimensionless number Te finds a useful application as the parameter characterising the optimum loading for power transport between two interconnected devices

Inserting the resultant expression for ΔP into the definition of Te_L from Fig. 30 and applying the definition of m from Fig. 27 leads to the following nondimensional available output power:

$$Te_L = BR_S - 2BR_S \mu = BR_S(1-\mu^2) \tag{5}$$

This is plotted in Fig. 31 as the dimensionless representation of family of curves in Fig. 29 (which shows only two representative curves from the family).

To transfer the maximum possible power into the load, it is necessary to reach the top of the curve where the derivative must be zero:

$$\frac{dTe_L}{d\mu} = BR_s - 2BR_s = 0 \quad \ldots \mu_{opt} = \frac{1}{2} \tag{6}$$

Optimum loading of the valve is achieved for output flow $\dot{V}$ equal to one half of the supply flow rate o$\dot{V}_S$. To obtain this, the resistance of the load is to be the same as that of the internal resistance of the upstream three-terminal device, $R = R_S$. An interesting result is the maximum relative transferred power, equal to $BR_S/4$, obtained by inserting eq. (6) into eq. (5). This makes another interesting interpretation of the meaning of constant B possible.

11. OPTIMUM POWER TRANSFER IN THE QUADRATIC CASE

The solution of the maximum power transfer task using the loading parameter Te_L is quite general; it may be even extended to the case of high Reynolds number flows, where the linear relation (Fig. 16) between the flow rate and the generated

pressure drop in the two-terminal load device is replaced by the quadratic constitutive relation:

$$\Delta P = Q \cdot \left(\dot{V}\right)^2 \tag{7}$$

with the quadratic dissipance $Q\,[\mathrm{kg \cdot m^{-7}}]$. The loading characteristic of the upstream three-terminal device is correspondingly:

$$\Delta P = a - Q_s \cdot \left(\dot{V}\right)^2 \tag{8}$$

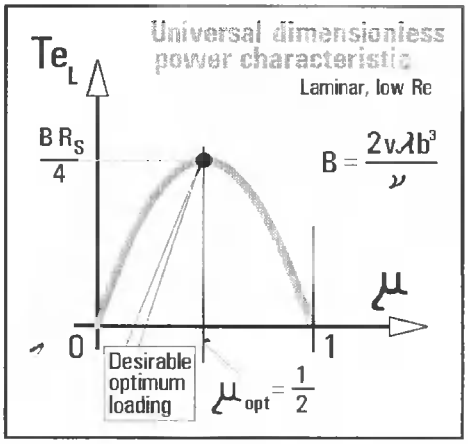

Fig. 31. Dimensionless counterpart to the power characteristics in Fig. 29 for laminar, low Reynolds number flows. Note the universality: the whole family of dimensional curves from Fig. 29 squeezes into this single parabola

As before, the constant a may be eliminated by noting the conditions for the maximum flow rate: $\Delta P = 0$ and $\dot{V} = \dot{V}_s$ so that $a = Q_s \cdot \left(\dot{V}\right)^2$ and:

$$\Delta P = Q_s\left(\dot{V}_s\right)^2 - Q_s\left(\dot{V}\right)^2 \tag{9}$$

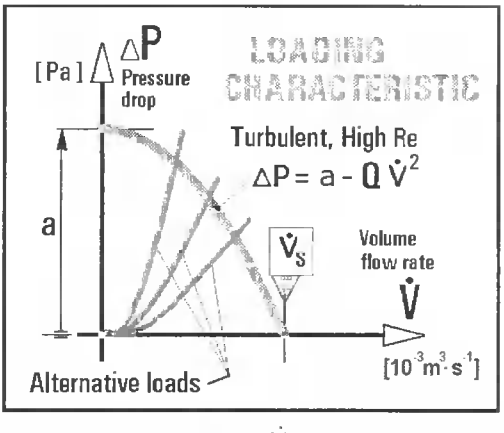

Fig. 32. Dependence between the output flow rate $\dot{V}$ and the available pressure drop ΔP. This is a counterpart to Fig. 26 for high Reynolds number flows with constant Euler numbers and therefore with quadratic characteristics

Inserting eq. (9) into the expression for Te_L in Fig. 30 leads to:

$$\mathrm{Te}_L = BQ_S \dot{V} \mu(1-\mu^2) \tag{10}$$

and the condition for optimum loading $d\mathrm{Te}_L / d\mu = BQ_S \dot{V} \mu(1-3\mu^2)$:

$$\mu_{opt} = \frac{1}{\sqrt{3}} \tag{11}$$

The maximum $\mathrm{Te}_{Lmax} = 2BQ_S \cdot \dot{V}_S / 3\sqrt{3}$ is obtained with relative dissipance of the load $q = Q/Q_S = (1-\mu^2)/\mu$ if $q = 2$. The diagram Fig. 33 presents the relative values $\frac{\mathrm{Te}_L}{\mathrm{Te}_{Lmax}} = \frac{q}{2}\left(\frac{3}{1+q}\right)^{3/2}$ to show how near it is possible to approach the theoretical maximum with different relative loads q.

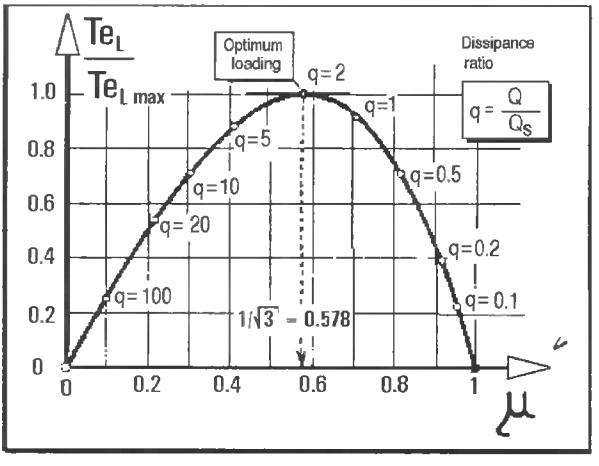

Fig. 33. Universal power characteristic for turbulent, high Reynolds number flows in the relative nondimensional co-ordinates

With load dissipance Q the same as the internal output + dissipance Q_S of the upstream device, or 5-times as large, it is still possible to transfer nearly 90% of the maximum power. However, with load dissipance much smaller, $q = 0.1$ or much larger $q = 100$, the transferred power is only about 25% of what the upstream device can deliver – and no wonder such poor transfer can lead to disappointments of those who neglect the matching task.

12. CONCLUSIONS

The newly found dimensionless characterisation parameter Te was initially considered to be just a simple tool without any further meaning. The present paper demonstrates it as an important quantity competing with parameters as important as the traditional Reynolds and Euler numbers. The analysis shows it is, in fact, a product of these numbers. It is, however, so useful in fluidic and microfluidic device characterization and circuit solution tasks that it deserves to be more widely known.

REFERENCES

[1] Foster K., Parker G.A., 1970. FLUIDICS – Components and Systems. Wiley-Interscience London.

[2] Tippetts J.R., 2002. Watts, Bits, and Fluidics. Proc. of MECH2K2 Intern. Congress on Mechatronics.

[3] Tesař V., 1998. Valvole fluidiche senza parti mobili. Oleodinamica pneumatica, 39 (3), Milano, 216-223.

[4] Tesař V., 1983. Großmaßstäbliche fluidische Ventile für die Durchflußsteuerung. Messen-steuern-regeln Bd. 26 (4), Berlin.

[5] Stone H.A., Kim S., 2001. Microfluidics: Basic Issues, Applications, and Challenges. AIChE Journal, 1250.

[6] Tesař V., 2002. Microfluidics. [In:] Festschrift UFT 2002, Publ. by UFT Umwelt- und Fluid-Technik, Bad Mergentheim Germany, 97-114.

[7] Tesař V., 2001. Microfluidic Valves for Flow Control at Low Reynolds Numbers. Journal of Visualisation 4 (1), 51-60.

[8] Tesař V., 2002. Microfluidic Turn-down Valve. Journal of Visualisation 5 (3), 301-307.

[9] Tesař V., 2002. Sampling by Fluidics and Microfluidics. Acta Polytechnica - Journal of Advanced Engineering CVUT Prague 42(2), 41-49.

[10] Tesař V., 1976. A System of Quantities for Description of States Occuring in Fluidic Circuits. Proc. of 6th Jablonna Conference on Fluidics, Moscow.

[11] Tesař V., 2000. Asymptotic Correlation for Pressure-Assisted Jet-Type Microfluidic Devices. Proceedings of Topical Problems of Fluid Mechanics 2000, Inst. of Thermomechanics AS CR, Prague, 85-88.

[12] Tesař V., 1992. Similarity in Power Fluidics. Proc. of Dimensional Analysis in Fluid Mechanics. Inst. of Thermomechanics, Czechoslovak Acad. Sci.

[13] Tesař V., 1981. Characterisation of Three-Terminal Fluidic Elements and Solution of Bifurcated-Flow Circuits Using the Concept of Equivalent Dissipance. Journal of Fluid Control / Fluidics Quarterly 13 (2), Ann Arbor, USA.

[14] Nogid L.M., 1959. Teoriya podobiya i rozmernostey. Leningrad.

[15] Zierep J., 1991. Ähnlichkeitsgesetze und Modellregeln der Strömungslehre. 3rd ed., Braun Karlsruhe.

[16] Čarnogurská M., 2000. Základy matematického a fyzikálného modelovania v mechanike tekutín a termodynamike. [Basics of mathematical and physical modelling in fluid mechanics and thermodynamics]. Vienala Košice, 91 [in Slovakian]

[17] Götler H., 1975. Dimensionanalyse. Springer Berlin.

[18] Conway J.H., Guy R.K., 1996. The Book of Numbers. Springer New York, 187-189.

[19] IUPAC, 1997. Compendium of Chemical Technology, 2nd ed.

Václav Tesař[1]
John R. Tippetts
Ray W.K. Allen

University of Sheffield
Department of Chemical and Process Engineering
Mappin Street, Sheffield S1 3J, United Kingdom
[1] *on leave from CTU Czech Technical University, Prague, Czech Republic*

'FAILURE' OF STEADY CFD SOLUTIONS CAUSED BY VORTEX SHEDDING

Summary: Results of numerical computations of essentially steady flowfields may be significantly in error if the steady-state version of the software predicts large standing vortices which, in reality do not remain steady but are swept away with the flow. The present authors encountered a typical example of such 'failure' of the computations applied to a design of a microfluidic valve. The persistent enigmatic disagreement between the CFD results and experimental data was explained by flow visualisation showing a large dominant vortex shed with the flow.

Keywords: microfluidics, CFD, standing vortices

1. INTRODUCTION

Progress in software for numerical solution of fluid flow has led to very high standard of reliability of the computed results. The present authors have been using a commercial CFD code with confidence for design of microfluidics valves and find the results usually quite well validated by subsequent experimental tests, provided there is no niggardly attitude towards the number of used grid elements. Typically, 100 000 grid elements are needed to discretise the valve geometry reliably. This is a large number which admittedly makes the computations rather time-consuming. Typical configurations of microfluidics valves are planar shapes of constant, rather shallow depth (Fig.1). To capture reasonably the vertical velocity profiles, at least 8-10 grid elements are to be used in the depth direction. Since the grid elements should not be of very elongated shapes, also their size in the plan view has to be correspondingly small. This rules out possible savings of the number of grid elements in those increased area regions where velocities are small and no spectacular hydrodynamic phenomena can take place – so that a smaller number of rather large elements would be otherwise quite acceptable.

Generally, microfluidics is more suitable for computation-aided design than for many other applications. Laminar flows avoid the problems and uncertainty associated with the choice of various turbulence models. Operating at very low Reynolds numbers causes problems with inapplicability of standard fluidic principles of the no-moving-part valve operation, requiring them to be pressure driven [3], which is yet of no consequences for the CFD flowfield solution procedures.

A considerable problem, however, emerged recently. Somewhat characteristically, it arose in an extraordinary situation involving large Reynolds number flows.

The failure of an agreement between the computational and experimental validation data was thus initially attributed to problems with turbulence modelling. Nevertheless, results of repeated computations with no less than seven different models have shown remarkable mutual similarity. It was not until flow visualization investigations on scaled-up laboratory models were performed that an explanation and clarification of what seemed to be a spectacular failure of CFD was finally found.

2. VALVE AND ITS BEHAVIOUR

The microfluidic valve in which this problem was encountered is shown in Fig. 1. It is a part of a sampling unit for high throughput testing of catalysts, consisting essentially of 16 identical valves [1]. The output terminals Y of all 16 valves are connected to a common chemical composition analyzer. Only one valve of the unit at any time is in its OPEN state, enabling the flow of fluid sample from the supply terminal S into the analyzer. The remaining 15 valves are in the CLOSED state, into which they are brought by control flow, admitted into the control inlet X, which sweeps the sample away into the vent.

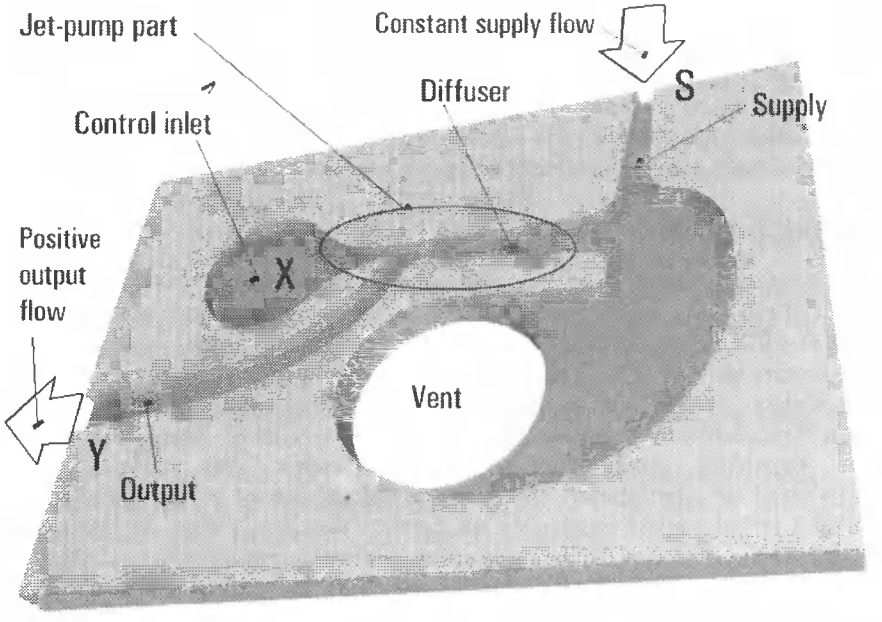

Fig. 1. Microfluidic valve with jet pumping integral part designed for the extraordinary requirement of generating negative output flow in the CLOSED state

An extraordinary requirement on valve operation is the stipulation of a jet pumping effect to be generated in the CLOSED state – so that output fluid flow becomes negative, i.e. directed into the valve. This is intended to remove from the analyzer and all cavities downstream from the valves any traces of previously present samples and thereby achieve high sample purity. Jet pumping effect of laminar jets being too weak, this calls for presence of quite powerful turbulent jet. The supply flow cannot be used for the purpose – its magnitude is limited by the requirement of residence time in the microreactor, from which the sample is taken. The only suitable

flow is the control flow. This, of course, leads to a paradoxical situation of the fractional flow gain, control flow being much more powerful than the supply flow in controls (quite opposite to usual valves being basically fluidic amplifiers, with weak control manipulating a much larger controlled flow – their ratio, the flow gain, being as large as perhaps 100 or even more). The fractional (< 1.0) gain is acceptable due to very small absolute flow rate magnitudes in microfluidics [4], where the large consumption of control fluid is immaterial. Still, the Reynolds number of the control flow is here not really large. To generate a sizeable jet pumping, the valve contains what is in fact a well-shaped jet pump – with high contraction primary nozzle and a long diffuser downstream from the secondary inlet (which doubles as the output channel in the OPEN state).

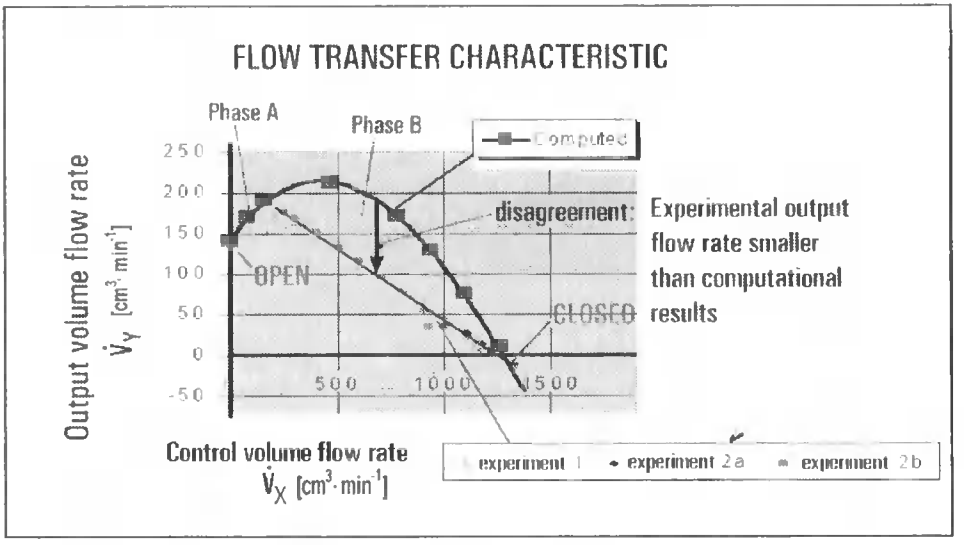

Fig. 2. Comparison of the flow transfer characteristics obtained numerically as well as experimentally for a scaled-up model of the valve

The operation of the valve is best explained by means of its flow transfer characteristics, Fig. 2. This shows the output flow response to an increasing control flow plotted on the horizontal co-ordinate. At the outset, in Phase A, the output flow rate (the vertical co-ordinate) increases above its value in the OPEN state, the initially weak control flow not having sufficient momentum to act on the supply flow (driven by a considerable driving pressure difference between V and Y) and simply adds to the amount leaving through Y. It requires a considerable increase in the control flow magnitude for reversing this trend in the next Phase B. The output flow then begins to decrease. It goes down to zero and finally, in the CLOSED state, even reaches the desirable small negative value.

It is only in the CLOSED state, and immediately before reaching it, in the latest stage of the closing process, that the jet pump part of the valve has an opportunity to operate really as a jet pump, sucking the returning fluid through the output channel. Both in Phase A as well as Phase B the flow in this jet pump secondary inlet has a reverse orientation. The mode of operation differs not only from the usual processes in jet pumps, but is of different character in the two phases. In Phase A there is a

confluence (Fig. 3) of the supply (sample fluid, dark) and the control (light color) flows – as visualized by addition of dye into a scaled-up model flow in Fig. 4.

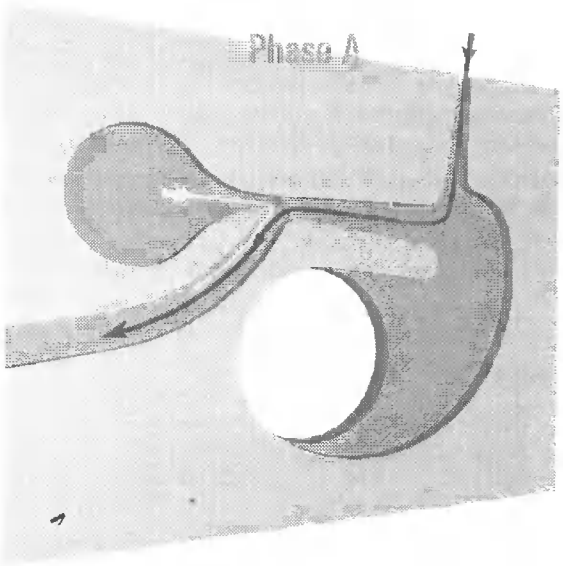

Fig. 3. Flow junction in the jet-pumping part of the valve in the initial Phase A. Schematic representation of the light-colored control flow and the dark sample fluid flow. At the small control flow level in Phase A, the sample still gets to the output terminal

Fig. 4. Jet-pumping part of the valve in Phase A visualized by addition of a dark dye to the sample fluid flow. The small control flow just leaves through the output Y (Fig. 1) together with the sample fluid

On the other hand, in Phase B the control flow displaces the sample fluid completely from the jet pump part of the valve and the positive output flow in the output channel is solely a bifurcated percentage of the control fluid. Fig. 5.

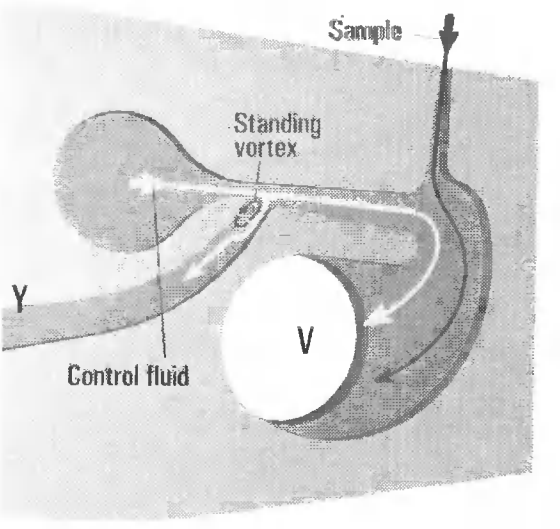

Fig. 5. Schematic representation of the light-colored control flow and the dark sample fluid flow inside the valve in Phase B (Fig. 2). At the larger control flow, the sample fluid is displaced from the jet-pump part of the valve

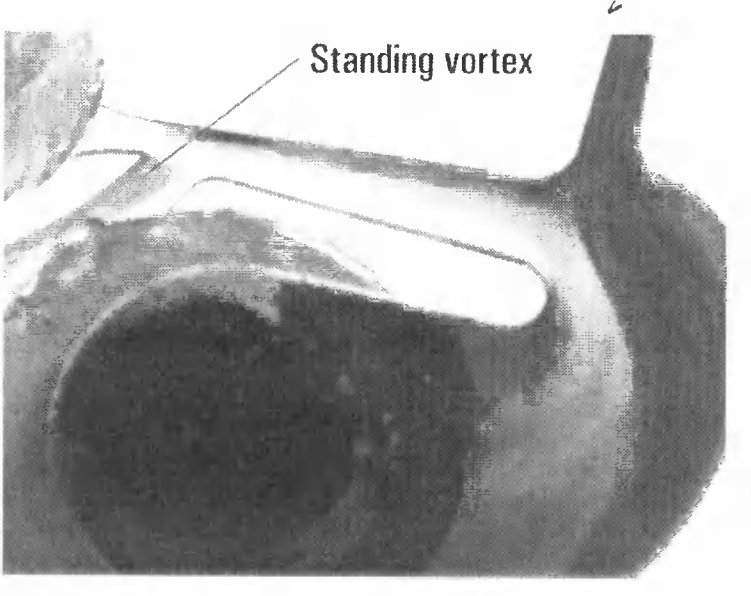

Fig. 6. Visualised large standing vortex predicted by the CFD solution in Phase B at the inlet into the output channel. It is visible as it retains the dye from the sample fluid passing there in Phase A

Fig. 7. Visualised fluid flow inside the valve in Phase B after some time has elapsed. The computation predicted large vortex was swept away with the flow into the output channel

3. PROBLEM AREA

As shown in Fig. 2, there is quite an excellent agreement between the computation and experiment data both in the OPEN as well as the CLOSED state. In fact, also in the initial Phase A of closing the valve the agreement is remarkably good. A more surprising is the disagreement found in the next Phase B. The actually measured output flow decreases linearly towards the CLOSED state and fails to continue rising smoothly towards the local maximum predicted by the computation.

The computed behavior in Phase B is dominated by the presence of the large vortex (Fig. 8) predicted to remain stationary inside the entrance into the output channel. The positive output flow, which is a part of the increased control flow, squeezes into this channel past the vortex. In a typical Phase B computed prediction shown in Fig. 8, the Reynolds number of the diffuser flow is still too small for an efficient diffuser action: note that pressure in the diverging channel between the locations B and C actually decreases. On the other hand, a substantial diffuser effect is predicted on the short segment between A and B. No solid-wall diffusers would work so well requiring so short length – the effect is solely due to the presence of the standing vortex.

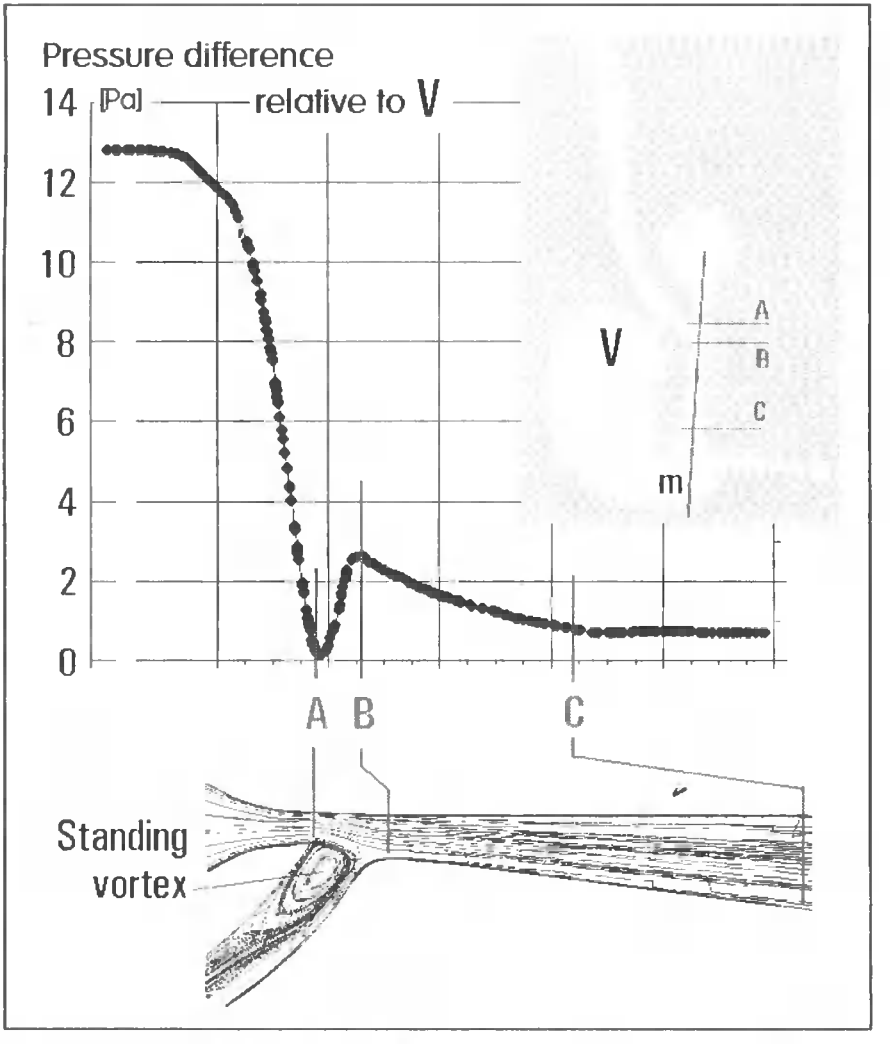

Fig. 8. Computationally predicted standing vortex in the exit channel entrance generates pressure rise between A and B, which is not found in the experiment

4. EXPLANATION OF THE PROBLEM

Similar diffusers with standing vortices were proposed by [2]. In practice, they invariably failed as the vortices did not remain in their predicted positions and were in fact shed, carrying away with them the energy spent on their formation. The same effect, the dominant large vortex not remaining in the predicted position, was found to be the reason behind the present enigmatic disagreement in Phase B. Of course, the vortex formation and shedding being an unsteady phenomenon, it cannot be predicted by a steady state CFD computation.

This explanation was verified by flow visualizations. The used laboratory scaled-up model, though made of Perspex, was originally not intended for visualization

purposes. The entrance into the output channel, where the processes of interest take place, are obscured by other parts of the model. The pictures, Figs. 6 and 7, are therefore not of the standard we are used to see in visualization photographs made for educational purposes. This, however, is a situation quite commonly encountered in practical engineering development. Importantly, the basic facts about the vortex are clearly recognizable. Initially, after a particular Phase B regime was set up, the presence of the large standing entrance vortex is manifested by the remaining blue dyed fluid, Fig. 6. The vortex, however, does not remain there permanently and is carried down the output channel with the output flow. The video frame in Fig. 7, after some time elapses, shows the entrance wholly devoid of any blue dyed fluid.

Of course, with the vortex missing for considerable periods of time, the actual behaviour is quite different from what was predicted. As the vortex is predicted only in one particular flow phase, with bifurcating control flow in Phase B, there is no problem in other regimes, like Phase A, where there is no vortex shedding effect and no such disagreement. Such unexpected change between the well predictable and unpredictable phases during what seems to be a simple transition from the OPEN state of the valve into its CLOSED state makes the problem encountered particularly dangerous.

5. CONCLUSION

The flows in the developed valve being steady, it is quite natural to use steady state CFD computations for their evaluation, with the effect of turbulent vortices represented by the time-mean Reynolds averages. Unfortunately, this necessarily fails to predict what is basically a time-dependent phenomenon, like the predicted large steady vortex, dominating the flow in the present case, being actually unsteady: growing, carried away, and then growing again. The disagreement between the steady prediction and actual behavior cannot be attributed to any "error" of the CFD code used. It is a case of selecting inadequate flow model (steady state). The effect is particularly deceitful as it may appear without warning in only in a particular operating condition after quite immaculate results were obtained elsewhere.

REFERENCES

[1] Low Y.Y., Tesar V., Tippetts J.R., Allen R.W.K., Pitt M., 2001. Multichannel Catalyst Testing Reactor with Microfluidic Flow Control. Proceedings of 3rd European Congress of Chemical Engineering ECCE3, Nuremberg, 1029-1040.

[2] Ringleb F.O., 1961. Separation Control by Trapped Vortices. [In:] Lachmann G.V. (ed.), Boundary Layer and Flow Control, its principles and application. Vol. I, Pergamon Press Oxford.

[3] Tesař V., 2000. Microfluidic Valves for Flow Control at Low Reynolds Numbers. Journal of Visualization 4 (1), Japan, 51-60.

[4] Tesař V., Low Y.Y., Allen R.W.K., Tippetts J.R., 2001. MICROFLUIDICS FOR MEMS – Microfluidic Valve. PICAST IV – Proceedings of the 4th Pacific International Conference on Aerospace Science and Technology, National Cheng Kung University Kaoshiung, Taiwan, 301-306.

Janusz Zachwieja

University of Technology and Agriculture
Faculty of Mechanical Engineering
Department of Applied Mechanics

ANALYSIS OF DYNAMICS OF STODOLA-GREEN ROTOR IN FLEXIBLE BEARING

Summary. The paper presents a numerical approach to dynamics of a one-disk rigid rotor. An assembly composed of a non-deformable disk on a shaft is often found in flow machines such as pumps or ventilators. Due to its technical significance, the system was subject to a series of analyses, both theoretical and experimental, mainly for critical velocity determination. The hanging out position of the disk is conducive to the occurrence of gyroscopic effects which, depending on the conditions, can stabilise the rotor motion (synchronous precession) or decrease its critical velocity (asynchronous precession).

The description of rotor motion with the use of an analytic method is usually based on the assumption that bearing nodes reveal a susceptibility which equals zero. This is a simplification which, nowadays, cannot be accepted. The support stiffness observed in this paper has a great influence on the rotor vibration quantity. Moreover, in practise, it is not possible for the bearing stiffness in different planes to be identical. This effect, described as the rotor outer anisotropy, is the cause of more than one critical velocity. These phenomena must be taken into account at the machine design stage so that its nominal velocity will be much smaller than the critical velocities. Otherwise each starting and coasting of the rotor is connected with going through the resonance area, causing a multiple increase in the vibration amplitude.

Each rotor has certain unbalance, which results in centrifugal force or a couple of forces affecting the bearing during the rotors motion. Synchronous perturbation of such a source can be removed by balancing the disk alone or the disk and the shaft. Stiffness of shaft support is essential for the course and the final effect of rotor balancing in own bearings. For numerical analysis of the dynamics of rotor with flexible bearings, the standard Finite Elements Method has been used.

Keywords: dynamics of rotor, internal anizotropy, numerical disk model

1. INTRODUCTION

Although there is a number of methods used in the analysis of the issue discussed such as:

- finite rigid elements method (SES),
- variation methods (Reileig, Ritz, Galerkin,
- transition matrix method,

nevertheless the classic method OES is used most frequently. Let us limit our considerations to the rotor itself i.e. deformable shaft with a rigid disk set in flexible bearings.

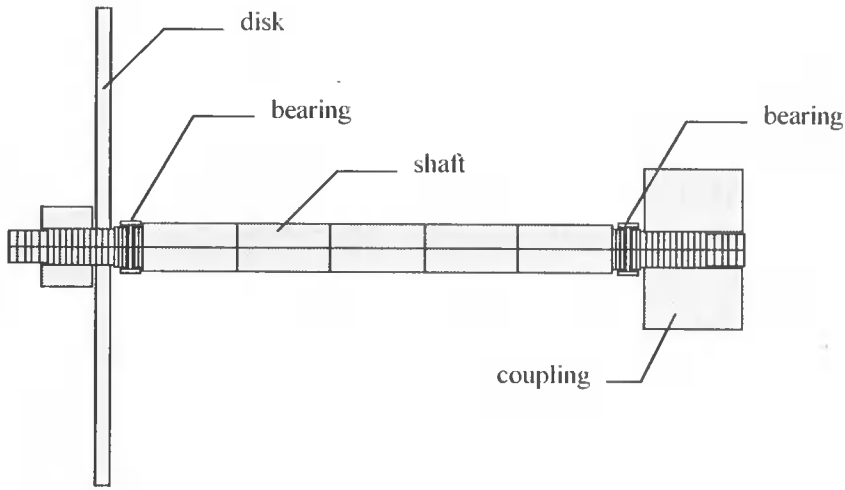

Fig. 1. Division of rotor into deformable finite elements

The rotor presented in Fig. 1 will be divided into three arrangements, which will be analyzed separately, and then "glued" by a proper composition of inertia, stiffness and damping matrices.

2. DESCRIPTION OF SHAFT FOLLOWING OES METHOD

The shaft beam element has four degrees of freedom in the node (Fig. 2). It means that, we accept only a possibility of the transverse shaft vibrations occurrence, however, we neglect, the influence of torsional vibrations.

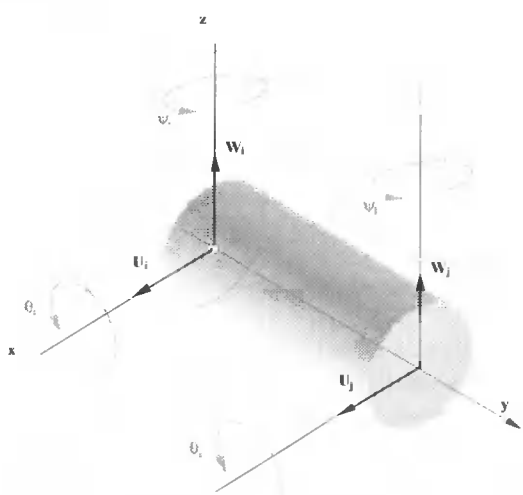

Fig. 2. OES of a beam type with four degrees of freedom in the node

Four displacements and four angles are node displacement vector components.

$$\boldsymbol{\delta}_e = \begin{bmatrix} u_i & w_i & \psi_i & \theta_i & u_j & w_j & \psi_j & \theta_j \end{bmatrix}^T \tag{1}$$

where:

$u_i, w_i, \psi_i, \theta_i$ translation displacements and angles of deflection in node 'i',

$u_j, w_j, \psi_j, \theta_j$ translation displacements and angles of deflection in node 'j'.

Displacements and angles of deflection along the cylinder axis (coordinate y) are expressed as:

$$\begin{bmatrix} u(y) \\ w(y) \end{bmatrix} = N(y)\boldsymbol{\delta}_e \tag{2}$$

and

$$\begin{bmatrix} \psi \\ \theta \end{bmatrix} = \begin{bmatrix} -\dfrac{\partial u(y)}{\partial y} \\ \dfrac{\partial w(y)}{\partial y} \end{bmatrix} = \begin{bmatrix} -1 & 0 \\ 0 & 1 \end{bmatrix} D(y)\boldsymbol{\delta}_e \tag{3}$$

here:

$$N(\xi) = \begin{bmatrix} N_1 & 0 & N_2 & 0 & N_3 & 0 & N_4 & 0 \\ 0 & N_1 & 0 & N_2 & 0 & N_3 & 0 & N_4 \end{bmatrix} \begin{bmatrix} N_{uu} \\ N_{uw} \end{bmatrix} = \tag{4}$$

$$\begin{bmatrix} 1-3\xi^2+2\xi^3 & 0 & L(\xi-2\xi^2+\xi^3) & 0 & 3\xi^2-2\xi^3 & 0 & L(-\xi^2+\xi^3) & 0 \\ 0 & 1-3\xi^2+2\xi^3 & 0 & L(\xi-2\xi^2+\xi^3) & 0 & 3\xi^2-2\xi^3 & 0 & L(-\xi^2+\xi^3) \end{bmatrix}$$

is the OES shape function matrix, whereas matrix **D** is expressed by dependence:

$$D = \begin{bmatrix} D_{uu} \\ D_{uw} \end{bmatrix} = \begin{bmatrix} 0 & \dfrac{\partial}{\partial y} \\ \dfrac{\partial}{\partial y} & 0 \end{bmatrix} N = \begin{bmatrix} 0 & \dfrac{1}{L}\dfrac{\partial}{\partial \xi} \\ \dfrac{1}{L}\dfrac{\partial}{\partial \xi} & 0 \end{bmatrix} N \tag{5}$$

$$\frac{1}{L}\begin{bmatrix} -6\xi+6\xi^2 & 0 & L(1-4\xi+3\xi^2) & 0 & 6\xi-6\xi^2 & 0 & L(-2\xi+3\xi^2) & 0 \\ 0 & 6\xi-6\xi^2 & 0 & L(1-4\xi+3\xi^2) & 0 & 6\xi-6\xi^2 & 0 & L(-2\xi+3\xi^2) \end{bmatrix}$$

Coordinate y referred to the finite element length was marked as ξ:

$$\xi = \frac{y}{L} \tag{6}$$

The cylinder motion will be considered in three reference systems – Fig. 3:

1. **0XYZ** is a stationary system,
2. **0xyz** is a mobile system, rotating with a cylinder,
3. **0'x'y'z'** is a mobile system with axes parallel to **0xyz** and the center lying on the cylinder rotation axis. Axes of this system are the main inertia axes of each of its cross-sections.

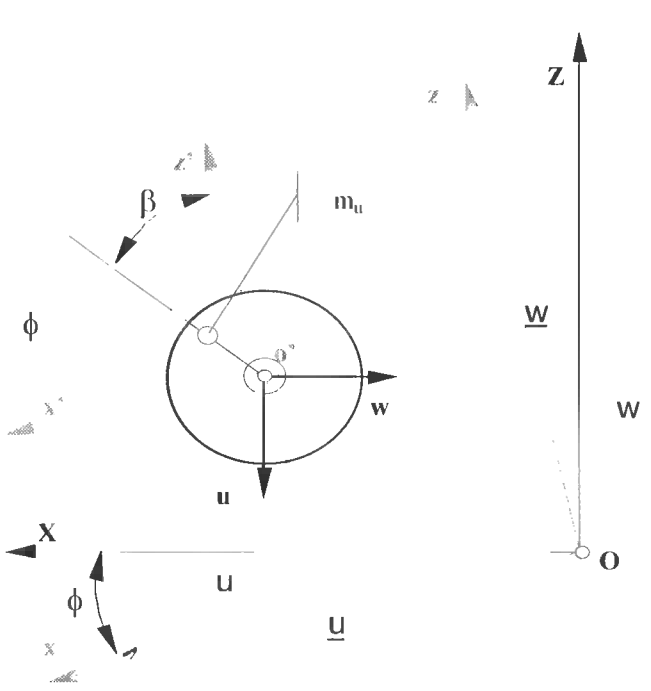

Fig. 3. Reference systems

The way in which dependences are derived into inertia, stiffness and damping matrices of the beam element can be found in the papers [1, 2]. The present paper is limited to the shaft motion equation in the form:

$$\mathbf{M}\ddot{\boldsymbol{\delta}}_e + \mathbf{C}\dot{\boldsymbol{\delta}}_e + \mathbf{K}\boldsymbol{\delta}_e = \mathbf{Q}_A + \mathbf{Q}_L \tag{7}$$

It should be noted that the equation describes the symmetric shaft vibrations. Matrices which occur in equation (7) stand for:

$\mathbf{M} = \mathbf{M}_t + \mathbf{M}_r$ – is an inertia matrix in a translation and rotation motion. $\mathbf{K}$ is the beam element stiffness matrix [5]. Matrix $\mathbf{C}$ is the so-called gyroscopic matrix connected with the reaction of moment a force in a precession motion [3].

Vector $\mathbf{Q}_A$ is a mass (weight) forces vector of the beam element:

$$\mathbf{Q}_A = \frac{1}{2}\rho g A L\left[0 \quad 1 \quad 0 \quad \frac{1}{6}L \quad 0 \quad 1 \quad 0 \quad -\frac{1}{6}L\right]^T \tag{8}$$

$\mathbf{Q}_L$ – is a vector of reaction force between the shaft and the disk and the bearing.

In case of a system: shaft, disk and bearings, these forces are inner forces, thus they occur in a general equation of motion.

3. NUMERICAL DISK MODEL

Disk equations of motion in a stationary coordinates system, assume the following form:

$$\mathbf{M}_D\ddot{\boldsymbol{\delta}}_0 + \mathbf{C}_D\dot{\boldsymbol{\delta}}_0 = \mathbf{Q}_D + \mathbf{Q}_L \tag{9}$$

In the equation (9), a lack of disk stiffness matrix can be noticed. It is a logical consequence of the assumption that the disc stiffness is very big (theoretically infinite – Fig. 4).

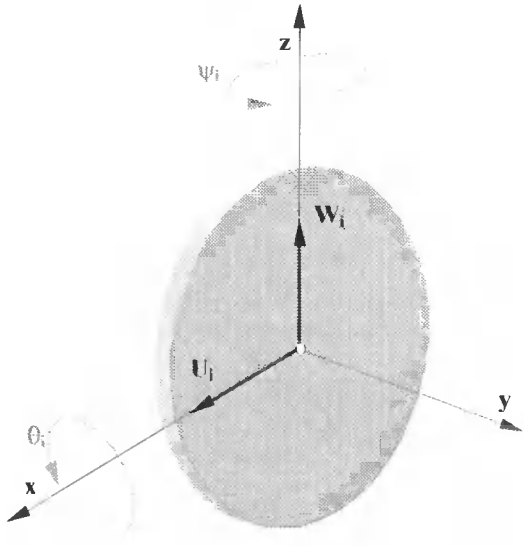

Fig. 4. Modeled disk as a finite element

Particular matrices and vectors are presented in the following way:

$$\mathbf{M}_D = \begin{bmatrix} m & 0 & 0 & 0 \\ 0 & m & 0 & 0 \\ 0 & 0 & J_x & 0 \\ 0 & 0 & 0 & J_x \end{bmatrix} \tag{10}$$

$\mathbf{M}_D$ is the disk inertia matrix, whereas m is a its mass and J_x is a mass moment of disk inertia in against axis x.

$$\mathbf{C}_D = \begin{bmatrix} c & 0 & 0 & 0 \\ 0 & c & 0 & 0 \\ 0 & 0 & 0 & J_y\Omega \\ 0 & 0 & -J_y\Omega & 0 \end{bmatrix} \tag{11}$$

$\mathbf{C}_D$ is the disk gyroscopic matrix. In turn J_y is its mass inertia moment in against of y axis. Rotational speed velocity of the disk was denoted by Ω.

$$\mathbf{Q}_D = m_u\Omega^2 d \begin{bmatrix} \sin(\Omega t + \beta) \\ \cos(\Omega t + \beta) \\ 0 \\ 0 \end{bmatrix} - mg \begin{bmatrix} 0 \\ 1 \\ 0 \\ 0 \end{bmatrix} \tag{12}$$

$\mathbf{Q}_D$ is a vector of forces reacting on the disk, namely gravity and centrifugal force coming from unbalance of the disk.

Unbalance of the disk is defined by:

m_u – unbalance mass;

d – distance from the unbalance mass center to disk rotation axis;

β – angular position of unbalance on a disk circuit.

4. NUMERICAL MODEL OF THE BEARING

Equation of a bearing motion has the following form (Fig. 5):

$$\mathbf{K}_p\boldsymbol{\delta}_p + \mathbf{C}_p\dot{\boldsymbol{\delta}}_p = \mathbf{Q}_L \tag{13}$$

Here matrix $\mathbf{K}_p$ is the bearing stiffness matrix:

$$\mathbf{K}_p = \begin{bmatrix} k_{zz} & k_{zx} \\ k_{xz} & k_{xx} \end{bmatrix} \tag{14}$$

whereas matrix $\mathbf{C}_p$ is bearing damping matrix:

$$\mathbf{C}_p = \begin{bmatrix} c_{uu} & c_{uw} \\ c_{wu} & c_{ww} \end{bmatrix} \tag{15}$$

Vector $\mathbf{Q}_L$ is reaction vector between the shaft and bearing.

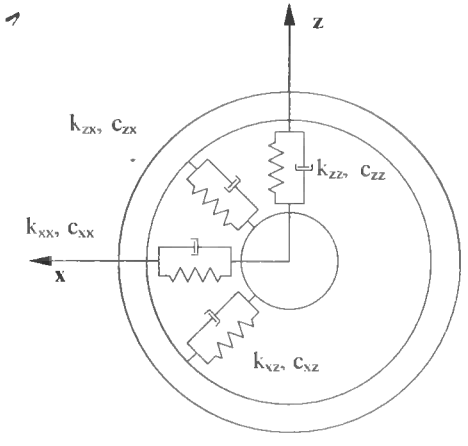

Fig. 5. Model of stiffness and damping in the bearing

5. NATURAL FREQUENCIES OF ROTOR VIBRATIONS AND INTEGRATION OF EQUATIONS OF MOTION

Equation of rotor motion including gyroscopic effects takes the following form:

$$\mathbf{M}\ddot{\boldsymbol{\delta}} + \mathbf{C}\dot{\boldsymbol{\delta}} + \mathbf{K}\boldsymbol{\delta} = \hat{\mathbf{Q}} \tag{16}$$

where:

$\mathbf{M}$ – matrix of inertia of the shaft-rotor system,

$\mathbf{C}$ – matrix of the bearing – shaft – disk system damping,

$\mathbf{K}$ – matrix of bearing – shaft – disk system stiffness,

$\bar{\mathbf{Q}}$ – vector of internal forces and outer forces reacting on the rotor.

Comparing the equation right side (16) to zero, we obtain a mathematical description of free vibrations of the rotor. Solutions are searched for following [2] and are reduced to the eigenvalue of matrix.

$$\mathbf{A} = \begin{bmatrix} \mathbf{0} & \mathbf{I} \\ -\hat{\mathbf{K}}^{-1}\hat{\mathbf{M}} & -\hat{\mathbf{K}}^{-1}\hat{\mathbf{C}} \end{bmatrix} \tag{17}$$

Further, for integration of equation (16) a method of central differences [6] has been used.

6. NUMERICAL MODELING OF ROTOR VIBRATIONS.

Fig. 6 shows a stand for rotor dynamics tests designed and built by the author in the Department of Applied Mechanics.

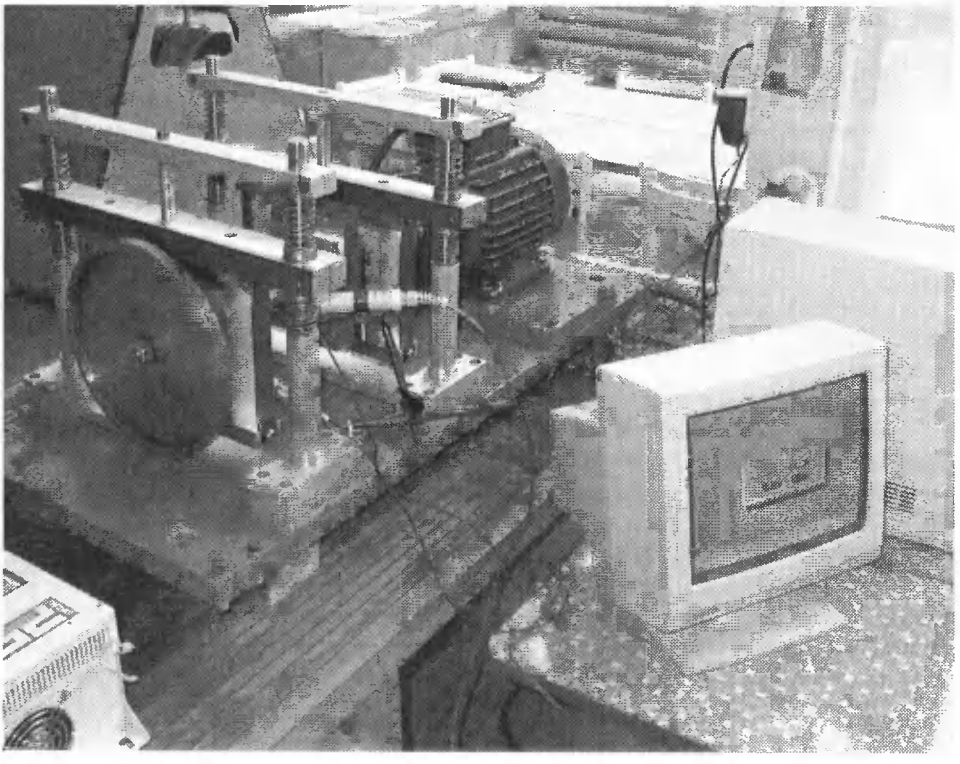

Fig. 6. Research stand

A method of rotor numerical modeling from Fig. 6 is shown in Fig. 1.

The rotor shaft was divided into 5 deformable finite elements (OES) of the beam type with four freedom degrees in the node. It means that we will take into consideration reactions on every element both induced by bending moment and by shearing forces. The influence of torsion was neglected do to flexible coupling between

the engine and rotating shafts. As a damping factor only the gyroscopic effect both of the shaft and the disk was taken into consideration to check its influence on the resonance frequency values [3]. The rotor is subject to synchronous perturbation, whose source is an unbalanced disk. Unbalance of rotor with 0.004 kgm was accepted for tests, in compliance with the assigned unbalance of rotor on a research stand. The calculations were made with a computer program developed in Department of Applied Mechanics [4]. The values assumed for calculations represent quite precisely the characteristics of the rotor tested, see Table 1.

Table 1. Geometrical material characteristics of finite elements modeling rotor.

Element		Value				
Disk		m [kg]	J_x,J_z [m^4]	J_y [m^4]	m_ud [kgm]	β
		2.89	0.012	0.024	0.004	π/4
Sshaft	Element	L [m]	D [m]	A [m^2]	I_x,I_z	I_o
	1	0.028	0.018	0.000254	5.153E-09	1.031E-08
	2	0.025	0.04	0.001257	1.257E-07	2.513E-07
	3	0.263	0.025	0.000491	1.917E-08	3.835E-08
	4	0.025	0.04	0.001257	1.257E-07	2.513E-07
	5	0.028	0.08	0.005027	2.011E-05	4.021E-06
Bearings		Stiffness matrix [N/m]		$\mathbf{K} = \begin{bmatrix} 1.41E+04 & 0 \\ 0 & 3.25E+04 \end{bmatrix}$		

The first five frequencies of free vibrations received in a way of numerical calculations are given in Table 2, Fig.7.

The free vibrations frequencies measured and calculated for rotor are presented in Fig. 8. The values denoted as I were obtained accepting extreme low stiffness in the vertical plane 1.41E+04 N/m. For mean stiffness in the interval tested equal 1.85E+04 N/m, the calculated values of free vibrations frequencies for the rotor are denoted as II. Differences between calculated values and experimentally determined values are a result of the approximate shaft position determination. The effect of support point transition from node 3 to node 2 is shown by a comparison of I and III values.

Table 2. Calculations free vibration frequencies of the rotor

Number of frequency	Value	
	[rad/s]	[Hz]
1	51.1	8.29
2	57.0	9.20
3	90.9	14.34
4	136.99	22.10
5	416.67	66.31

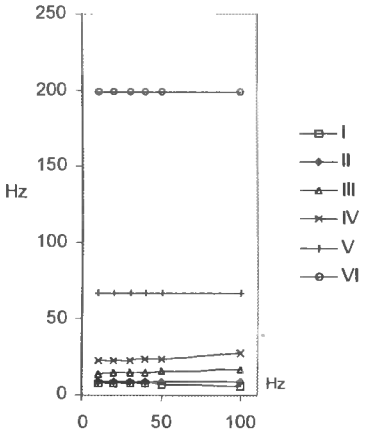

Fig. 7. Effect of rotation velocity of the rotor on its natural frequency values. The frequencies were marked with numbers I – VI

The differences between the measured and calculated values result also from determining the eigenvalue of matrix with error method (used algorithm of Cooley-Turke) and from neglecting the influence of inner damping of the shaft and a disk material. Usually for simple rotor models the damping matrix is accepted as a linear combination of inertial and stiffness matrices [5].

$$\mathbf{C} = \alpha \mathbf{M} + \beta \mathbf{K} \tag{18}$$

where: $\mathbf{C}$ – damping matrix,
$\mathbf{M}$, $\mathbf{K}$ – inertial and stiffness matrices,
α, β – proportionality coefficient,

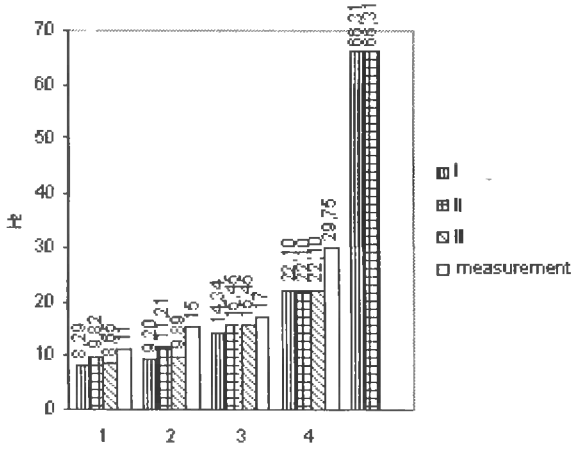

Fig. 8. Comparison of calculated and measured free vibration frequency values for the rotor

With the use of central differences method, the equation of motion was integrated from 6 Hz to 20 Hz. The results obtained are presented in Fig. 9 in the form of frequency-amplitude characteristics.

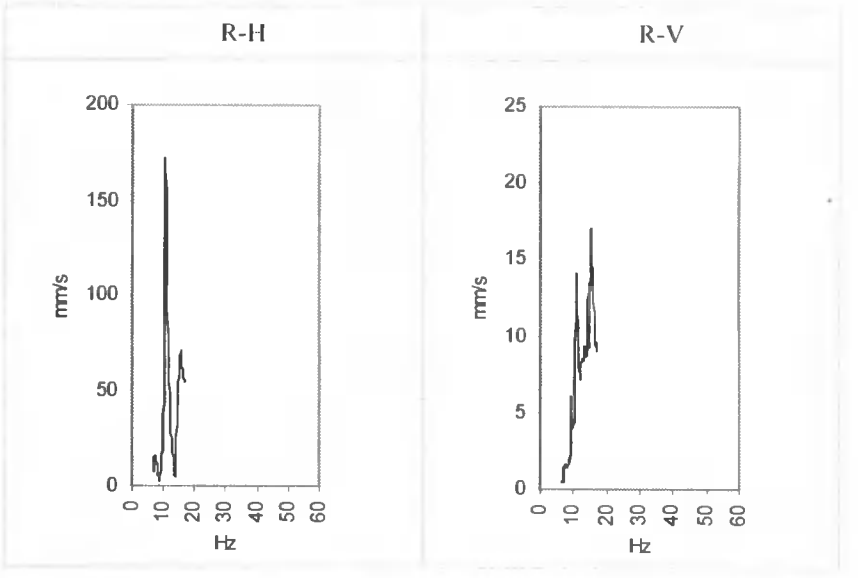

Fig. 9. Characteristics A-F (vibration velocities) of the rotor calculated for horizontal (R-H) and vertical (R-V) directions

In the range of vibration frequencies 10 Hz – 13 Hz vibration amplitude distribution from the vertical (amplitude value drop) to the horizontal plane (enhancement) is observed. This effect is visible in a numerical solution of shaft neck center motion trajectory presented in Fig. 10 and Fig. 11.

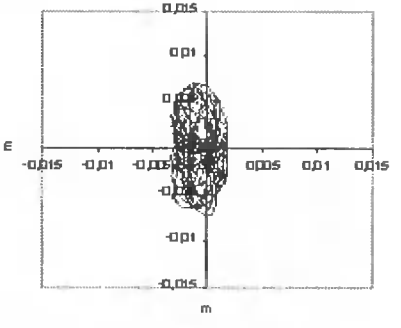

Fig. 10. Trajectory of shaft center motion for rotation frequency 10.5 Hz

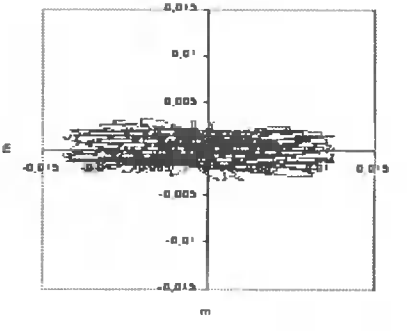

Fig. 11. Trajectory of shaft center motion for rotation frequency 13 Hz

Fig. 12 shows amplitude-frequency characteristics of the left rotor bearing vibrations in vertical and horizontal planes determined at rotor start.

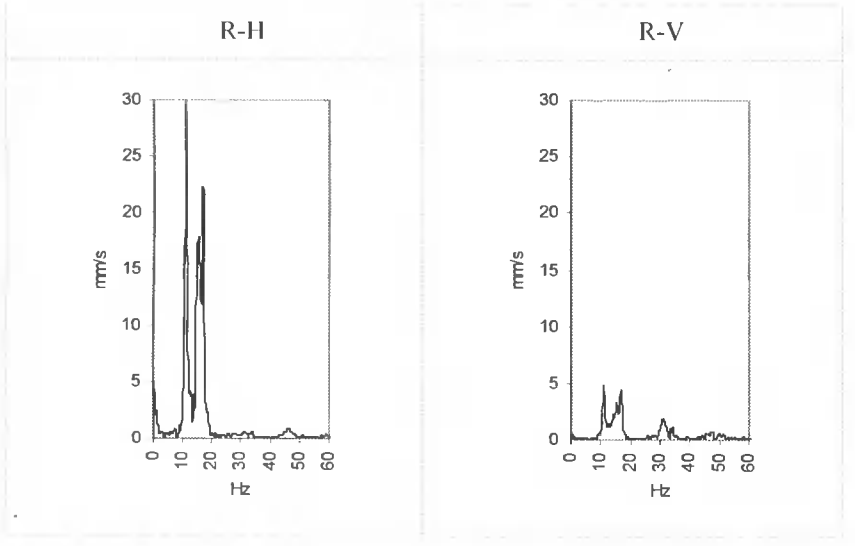

Fig. 12. Characteristics of the left rotor bearing vibrations velocities A-F determined at rotor start

The differences of the measured and calculated amplitudes observed are the effects of the measurement inertia in the short transition time through the resonance area as well as of the errors of stiffness evaluation and neglecting the system inner damping.

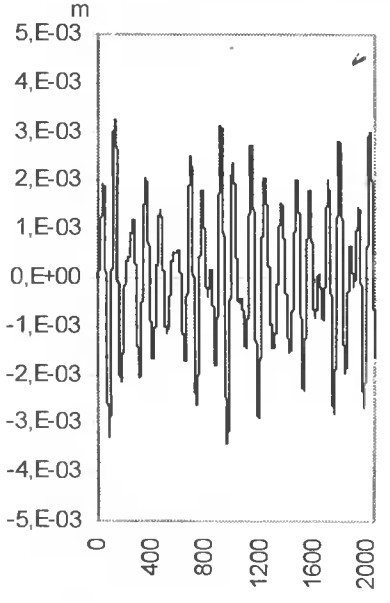

Fig. 13. Effect of rumble in a bearing vibration time course in plane R-H. Frequency 13 Hz

The system forced by synchronous perturbation in this frequency shows a tendency for simultaneous vibrations in its natural frequency, which is reflected by the rumble effect (Fig. 13).

7. CONCLUSIONS

The results of the theoretical analyses and experimental tests, the following conclusions can be formulated:

1. The dynamics of a Green-Stodola rotor supported in a flexible way can be analyzed using a simple model OES with four freedom degrees in the node. As a result quite precise critical velocity values are obtained. An adequate determination of bearing flexibility and of shaft support position is essential for these calculations.
2. The gyroscopic effect affects the rotor free vibration frequency value inconsiderably. Conditions for back drafi precession resulting from calculations are very difficult to be experimentally verified. Although the observed areas of unstable rotor work suggest the occurrence of back drafi circulation, the synchronous perturbation whose source is unbalance of the shaft cannot be the reason of such a disk precession occurrence.
3. Anisotropy of rotor support results in the occurrence of a strong resonance in the plane of smaller stiffness. The similarity between the rotor rotation frequency and its resonance frequency makes the rotor vibrations show a rumble effect.

REFERENCES

[1] Mohiuddin M.A., Khulief Y.A., 1999. Coupled bending torsional vibration of rotors using finite element. Journal of Sound and Vibration 223.
[2] Nelson H.D., McVaugh J.M., 1976. The Dynamics of Rotor-Bearing System Using Finite Elements. Journal of Engineering for Industry 98.
[3] Zachwieja J., 2002. Efekt żyroskopowy w dynamice walców maszyny papierniczej. Zesz. Nauk. ATR w Bydgoszczy, Mechanika 53.
[4] Zachwieja J., 2002. Drgania walca prowadzącego krajarki papieru KL63. Zesz. Nauk. ATR w Bydgoszczy, Mechanika 52.
[5] Kruszewski J., 1984. Metoda elementów skończonych w dynamice konstrukcji. Arkady Warszawa.
[6] Chmielewski T., Zembaty Z., 1998. Podstawy dynamiki budowli. Arkady Warszawa.

ISBN 83-89334-85-2